



ZERO BRINE

Software Tool for the Simulation of Selected Brine Treatment Technologies

Technology Libraries and Integrated Platform



The ZERO BRINE project (www.zerobrine.eu) has received funding from the European Union's Horizon 2020 research and innovation programme under grant agreement No 730390.

Deliverable 5.2		Software Tool for the Simulation	
Related Work Package	WP5 - Development of technology libraries (software tools)/ Integration into a common platform		
Deliverable lead	DLR		
Author(s)	DLR: Massimo Moser, Marina Micari, Benjamin Fuchs, Nikhil Pawar CTM: Joan Farnós		
Contact	Nikhil.Pawar@dlr.de Benjamin.Fuchs@dlr.de		
Reviewer	Andrea Cipollina (Unipa) Thomas Pregger (DLR)		
Grant Agreement Number	730390		
Instrument	Horizon 2020 Framework Programme		
Start date	1.6.2017		
Duration	54 months		
Type of Delivery (R, DEM, DEC, Other)¹	R / Other		
Dissemination Level (PU, CO, CI)²	PU		
Date last update	8.10.2021		
Website	www.zerobrine.eu		

Revision no	Date	Description	Author(s)
0.1	19. Sep 2018	First draft	Massimo Moser
0.2	12. Oct 2018	Technology Models CTM	Joan Farnós
0.3	22. Oct 2018	Technology Models DLR	Marina Micari
0.4	22. Oct 2018	RCE Platform Description and Setup	Ben Fuchs
1.0	22. Oct 2018	First review, first consolidated version	Massimo Moser
1.1	31. Oct 2018	Various Updates	DLR/CTM
2.0	25. Nov 2018	Review UNIPA	Andrea Cipollina
2.1	28. Nov 2018	Minor refurbishments	M. Micari, J. Farnos
2.2	30. Nov 2018	Consolidated version	Massimo Moser
2.3	08. Oct 2021	Revision (esp. ED, RCE), final version	Nikhil Pawar



The ZERO BRINE project has received funding from the European Commission under the Horizon 2020 programme, Grant Agreement no. 730390. The opinions expressed in this document reflect only the author's view and do not reflect the European Commission's opinions. The European Commission is not responsible for any use that may be made of the information it contains.

¹ R=Document, report; DEM=Demonstrator, pilot, prototype; DEC=website, patent fillings, videos, etc.; OTHER=other

² PU=Public, CO=Confidential, only for members of the consortium (including the Commission Services), CI=Classified

Table of Contents

1.	Introduction and Objectives.....	4
2.	Data Providers.....	5
3.	Data Management and Time Schedule.....	5
4.	Multi-Effect Distillation Model.....	7
4.1.	Forward Feed Model.....	9
4.2.	Thermal Vapour Compressor.....	12
4.3.	MED Model Validation.....	13
4.4.	MED Nomenclature.....	14
5.	Reverse Osmosis Model.....	15
5.1.	RO Membrane.....	16
5.2.	RO Element.....	18
5.3.	RO Plant.....	19
5.4.	RO Model Validation.....	22
5.5.	RO Nomenclature.....	22
6.	Nanofiltration Model.....	23
6.1.	DSMP-DE Membrane Model.....	24
6.2.	NF Element and Plant Model.....	27
6.3.	NF Model Validation.....	28
6.4.	NF Nomenclature.....	29
7.	Crystallizer Model.....	30
7.1.	Crystallizer Nomenclature.....	34
8.	Membrane Distillation Model.....	34
8.1.	DCMD Element Model – Heat and Mass Transfer.....	35
8.2.	DCMD Unit Model – Mass and Energy Balances.....	40
8.3.	DCMD Plant Model.....	41
8.4.	MD Nomenclature.....	43
9.	Ion Exchange Resins Model.....	45
9.1.	Model for IEX Resins for Water Softening.....	46
9.2.	IEX Nomenclature.....	51
10.	Eutectic Freeze Crystallization Model.....	52

10.1.	Data driven numerical Model.....	52
10.2.	Thermodynamic EFC Model	52
10.3.	Experimental Validation	58
11.	Electrodialysis Model.....	62
11.1.	Working Principle	62
11.2.	Mathematical Modelling.....	63
11.3.	Model Validation.....	69
11.4.	Nomenclature	69
12.	RCE Integration.....	70
12.1.	RCE	70
12.2.	RCE Server.....	71
12.3.	The RCE Client	72
12.4.	Tool Integration.....	72
12.5.	Technical Aspects of RCE.....	73
12.6.	RCE Integration of Tools.....	73
12.7.	Prerequisites	74
12.8.	Illustration of an RCE Tool and Modelling of a Treatment Chain	75
13.	Bibliography.....	77

1. Introduction and Objectives

The ZERO BRINE project aims to facilitate the implementation of the Circular Economy package and the SPIRE roadmap in various process industries by developing necessary concepts, technological solutions and business models to redesign the value and supply chains of minerals and water while dealing with present organic compounds in a way that allows their subsequent recovery.

Minerals and water will be recovered from saline impaired effluents (brines) generated by the process industry while eliminating wastewater discharges and minimizing the environmental impacts of industrial operations through brines (ZERO BRINE). ZERO BRINE brings together and integrates several existing and innovative technologies to recover products of high quality and sufficient purity to represent good market value.

The objective of this task was to develop a software tool that can be used to simulate different brine treatment trains that were selected during project implementation to treat different complex brine streams. To do so, technology libraries have been developed for each of the technologies that are used for the treatment. These libraries build on the experience of partners, using different programming environments, namely Python and Matlab. In a second step, a common simulation platform has been set up in order to simulate the complete treatment trains proposed in WP2-WP4. The implemented tool was used simulate case studies in the frame of WP7.

Matlab (matrix laboratory) is a powerful numerical computing environment, which has been commercially developed by Mathworks over the last 34 years. Matlab is mainly intended for numerical computing, nevertheless it offers a series of additional toolboxes for symbolic computing as well as graphical multi-domain simulation). This software was used by CTM to develop the simulation of the heat recovery systems, the eutectic freeze crystallization (TU DELFT-EFC) technologies. Python is a high-level programming language for general-purpose programming. Based on previous works carried out at the DLR, Python was used to model several water treatment technologies such as MED (plane and with thermal vapour compression (TVC)), reverse osmosis (RO), nanofiltration (NF), electrodialysis (ED) and the CrIEM crystallizer. DLR was responsible for the implementation of this task in close collaboration with the technology experts of the project. The software tool developed in this task was also used to evaluate the replicability of treatment trains in other process industries in the frame of WP8. For this purpose, the input data and process configurations were adapted so that simulation can be carried out for specific industrial plants.

2. Data Providers

Data providers are responsible for acquisition of the data, processing and visualization of the data and delivery all the data to the data manager. Most of the data from WP5 regarding EFC will be obtained thorough bench-scale and pilot scale experimentation. In the following table, the data providers for each process or technology are defined.

Table 1: Data provided from each partner in WP5, task 5.3.

Partner	Data provided
DLR	Leading partner
CTM	CTM was responsible of WP5 EFC modelling and to perform bench scale experiments to produce experimental data related to the membrane regeneration process, NF/RO technology and EFC. In addition, CTM was responsible to analyse samples from the pilot plant and to process the generated data with the support of other partners. CTM also evaluated heat waste recovery strategies creating theoretical data related to this process.
UNIPA	Unipa supported the modelling activities, in particular with regard to the validation of the MED model. In addition, Unipa delivered basic information about the modelling of the crystallizer.
FACSA	FACSA was responsible to provide techno-economic information useful for the activities of WP7 (feasibility studies)
SEALEAU	DLR provided support to Sealeau for the MED design
LENNTECH	Lenntech was responsible to provide validation data for the characterization of the NF model
TYPSA	TYPSA was responsible to provide techno-economic information useful for the activities of WP7 (feasibility studies)
TU Delft	TU Delft provided data on EFC, as the responsible technology provider.
NTUA	NTUA provided information regarding the MED pilot plant

3. Data Management and Time Schedule

The database of WP5 contains mainly technical information, experimental and observational data. Experimental data include all the data generated during experimentation at bench scale and at pilot scale. These data were collected by the person responsible for the experiments and sent to the person coordinating the task and WP5. The following table shows the data required for the simulations, which were obtained from experiments and supplementary literature research.

A schedule was developed for the delivery of the data, which was based on the planning for the experimental work. As various delays occurred, also as a result of the COVID-19 pandemic, the final data transfer and data integration into the software models could not be started until the end of 2020.

Table 2: Required data obtained for each process/technology.

Technology/process	Data produced
NF/RO	<p>Operation parameters: applied pressure; recirculation flow, permeate recovery, permeate flux. Literature data for: antiscalant dosage, cleaning operations, etc.</p> <p>Quality parameters: permeate (produced water) and concentrate composition. For permeate, conductivity was the most critical parameter.</p> <p>Cost parameters: energy requirements with and without waste heat recovery, chemicals, investment costs, membranes cost.</p>
EFC	<p>Operation parameters: temperature; feed flow.</p> <p>Quality parameters: Na₂SO₄ purity, water produced quality.</p> <p>Cost parameters: energy requirements with and without waste heat recovery, investment costs.</p>
MED	<p>Operation parameters: temperature; feed flow, etc.</p> <p>Quality parameters: concentrate brine concentration, water produced quality.</p> <p>Cost parameters: energy requirements with and without waste heat recovery, investment costs.</p>
ED	<p>Operation parameters: time, voltage, current and current density (calculated), flow, rate of feed, dilution, acid and base concentrate.</p> <p>Quality parameters: NaOH and H₂SO₄ concentration, water produced quality.</p> <p>Cost parameters: energy requirements, investment costs.</p>
CrIEM/Crystallizer	<p>Operation parameters: feed flow; alkaline solution concentration; feed concentration of Mg⁺⁺ and Ca⁺⁺.</p> <p>Quality parameters: effluent composition, fractionated crystallisation efficiency, purity of crystals.</p>

4. Multi-Effect Distillation Model

The technical/design model of the Multi-Effect distillation process is mainly based on mass and energy balances at steady-state conditions and on the evaluation of thermo-physical properties of water, in the liquid or in the vapor state, and of the NaCl-water solution. These properties are estimated via correlations reported in literature. The main input variables are: feed salinity, temperature and flow rate, steam temperature, motive steam pressure (in presence of the TVC), required brine salinity, temperature of the last effect and number of effects. All the geometrical features, such as the size of the tubes in the tube bundles or of the connecting lines, are given as parameters. Conversely, the key output variables of the design model are the heat exchanger areas, the preheater areas and the end-condenser area, the steam flow rate and the motive steam flow rate in the case of the MED-TVC.

The model takes advantage from a purposely developed resolution algorithm which includes minimization steps (via iterative procedures) allowing design requirements to be fulfilled. The model is able to run for different feed arrangements (FF-MED and PC-MED) and different design methods, which refer to different design requirements, i.e. one provides equal A_{HX} and equal A_{preh} , while the other provides equal temperature differences (ΔT_{eff}) for each effect. In general, for easiness of comparison with other technical models, the design method with equal areas of the heat exchangers and the preheaters was selected.

Table 3: Main inputs and outputs of the technical model for the MED process.

Model	Inputs	Outputs
Technical model	Number of effects (N [-])	Distillate flow rate (M_{dist} [kg/s])
	Feed flow rate (M_{feed} [kg/s])	Brine flow rate (M_{brine} [kg/s])
	Feed salinity (X_{feed} [ppm])	Heat exchanger areas (A_{HX} [m ²])
	Intake feed temperature (T_{feed} [°C])	Preheater areas (A_{preh} [m ²])
	Brine salinity (X_{brine} [ppm])	End-condenser area (A_{cond} [m ²])
	Steam temperature (T_s [°C])	Cooling-water flow rate (M_{cw} [kg/s])
	Motive steam pressure (P_m [bar])	Steam flow rate (M_s [kg/s]) and motive steam flow rate for MED-TVC (M_m [kg/s])
	Temperature in the last effect (T_N [°C])	Specific area (sA [m ² /(kg/s)]) and specific thermal consumption (sQ [kJ/kg])

The structure of the resolution algorithm is reported in Figure 1. As shown in the figure, the technical model presents three minimization loops, since it is required that (i) the areas of the heat exchangers

(A_{HX}) and (ii) the areas of the preheaters (A_{preh}) have to be equal and (iii) a given distillate flow rate (M_{dist}) has to be produced which corresponds to a given brine salinity.

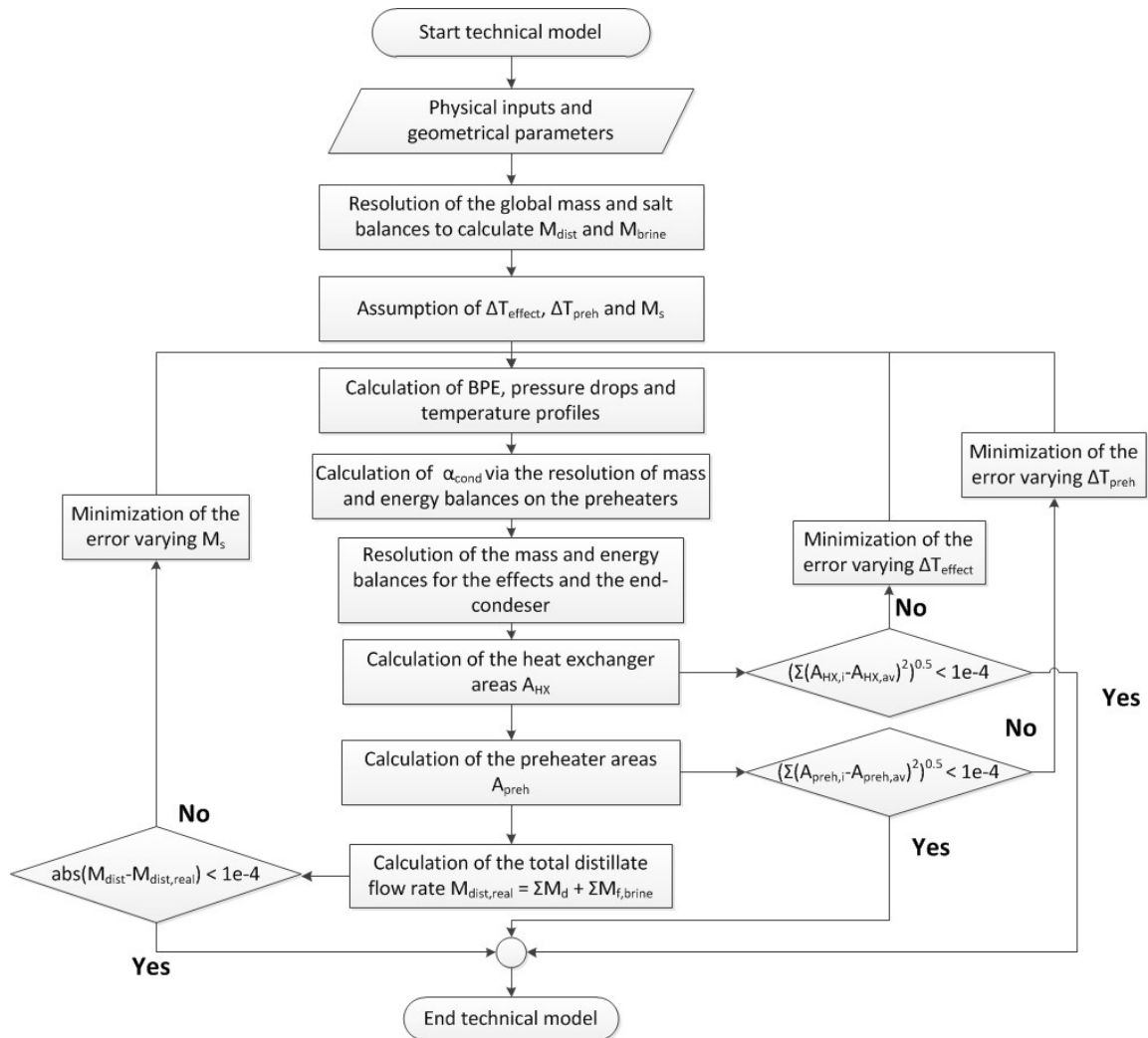


Figure 1: Resolution algorithm for the MED model.

The main output variables are the specific area (sA), the specific thermal consumption (sQ) and the GOR, which are defined as follows.

$$(4.1) \quad sA = \frac{\sum_N A_{HX} + \sum_{N-1} A_{preh} + A_{cond}}{M_{dist}}$$

$$(4.2) \quad sQ = \frac{M_s \lambda(T_s)}{M_{dist}}$$

$$(4.3) \quad GOR = \frac{M_s}{M_{dist}}$$

Where $\lambda(T_s)$ is the latent heat of water at a temperature equal to T_s .

In this report, a more detailed description of the FF-MED plant is reported because of the high concentrations and the high Top Brine Temperatures (El-Dessouky et al. 1998), which are common to most of the cases investigated by the Zero Brine project.

4.1. Forward Feed Model

The schematic representation of the MED plant described in the present FF-MED model is reported in Figure 2. It shows the first effect, a generic intermediate effect and the last effect with the end condenser. In fact, three slightly different systems of mass and energy balance equations have been used to model these three classes of effects.

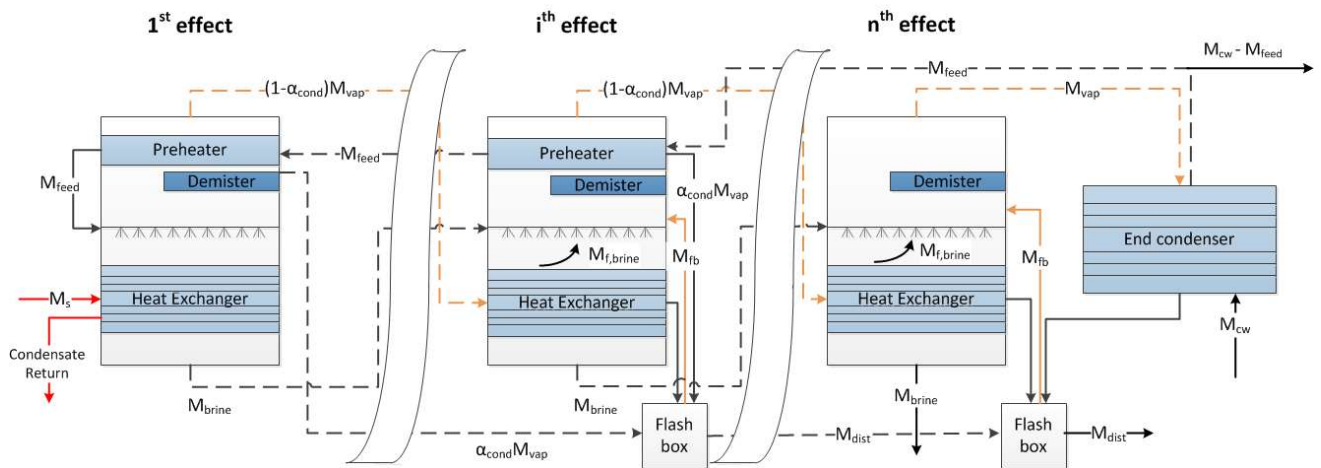


Figure 2: Schematic representation of the MED plant.

All the equations relevant to the model of the FF-MED are reported in Table 4, where λ is the latent heat of water, h_{vap} is the enthalpy of the steam, h_{liq} is the enthalpy of the liquid water, h_{sw} is the enthalpy of the NaCl salt-water solution and $c_{p,sw}$ is the NaCl salt-water solution specific heat. The water properties are a function of temperature, while the NaCl-water solution properties are functions of temperature and composition. Basically, each run starts from the calculation of global mass and salinity balances, to estimate the brine flow rate (M_{brine}), the distillate flow rate (M_{dist}) and the brine salinity (X_{brine}), having assumed that the distillate is pure water. Then, all the variables, such as mass flow rate, temperature and pressure, related to each single effect are estimated.

Table 4: Main mass and energy balance equations of the forward-feed MED model.

(4.4)	$M_{\text{feed}} = M_{\text{dist}} + M_{\text{brine}}$	Global mass balance
(4.5)	$M_{\text{feed}} X_{\text{feed}} = M_{\text{brine}} X_{\text{brine}}$	Global salt balance
(4.6)	$T_{\text{vsat}} = T - \text{BPE}(T, X_{\text{brine}})$	Temperature drop for the BPE
(4.7)	$T'_{\text{vsat}} = T_{\text{vsat}} - \Delta T_{\text{demister}}$	Temperature drop in the demister
(4.8)	$T'_c = T'_{\text{vsat}} - \Delta T_{\text{lines}}$	Temperature drop in the connecting lines
(4.9)	$T_c = T'_c - \Delta T_{\text{grav}} - \Delta T_{\text{acc}}$	Temperature drop in the evaporator
(4.10)	$M_s \lambda(T_s) + M_{\text{feed}} h_{\text{sw}}(T_{\text{preh}}[1], X_{\text{feed}})$ $= M_b[1] h_{\text{sw}}(T[1], X_b[1])$ $+ (1 - \alpha_{\text{cond}}[1]) M_{\text{vap}}[1] h_{\text{vap}}(T'_{\text{vsat}}[1])$ $+ \alpha_{\text{cond}}[1] M_{\text{vap}}[1] h_{\text{liq}}(T'_{\text{vsat}}[1])$	Energy balance on the first effect
(4.11)	$M_b[i - 1] = M_d[i] + M_{\text{brine}}[i] + M_b[i]$	Mass balance on a generic effect
(4.12)	$M_{\text{feed}} X_{\text{feed}} = M_b[i] X_b[i]$	Salt balance on a generic effect
(4.13)	$M_{\text{vap}}[i] = M_d[i] + M_{\text{brine}}[i] + M_{\text{fb}}[i]$	Mass balance on the vapor phase
(4.14)	$M_c[i - 1] + \alpha_{\text{cond}}[i] M_{\text{vap}}[i]$ $+ (1 - \alpha_{\text{cond}}[i - 1]) M_{\text{vap}}[i - 1] = M_{\text{fb}}[i] + M_c[i]$	Mass balance on the generic flash-box
(4.15)	$M_c[i - 1] h_{\text{liq}}(T'_{\text{vsat}}[i - 1])$ $+ \alpha_{\text{cond}}[i] M_{\text{vap}}[i] h_{\text{liq}}(T'_{\text{vsat}}[i]) +$ $(1 - \alpha_{\text{cond}}[i - 1]) M_{\text{vap}}[i - 1] h_{\text{liq}}(T_c[i - 1])$ $= M_{\text{fb}}[i] h_{\text{vap}}(T'_{\text{vsat}}[i]) + M_c[i] h_{\text{liq}}(T'_{\text{vsat}}[i])$	Energy balance on the generic flash-box
(4.16)	$M_{\text{brine}}[i] \lambda(T_{\text{brine},f}[i])$ $= M_{\text{brine}}[i - 1] c_{p,\text{sw}}(T_{\text{mean}}, X_b[i - 1])$ $(T[i - 1] - T_{\text{brine},f}[i])$	Energy balance on the brine entering as the feed ($T_{\text{brine},f}$ calculated via the Non Equilibrium Allowance (El-Dessouky et al. 1998))
(4.17)	$M_{\text{feed}} c_{p,\text{sw}}(T_{\text{mean}}, X_f) (T_{\text{preh}}[i] - T_{\text{preh}}[i + 1])$ $= \alpha_{\text{cond}}[i] M_{\text{vap}}[i] \lambda(T'_{\text{vsat}}[i])$	Energy balance on a generic preheater
(4.18)	$(1 - \alpha_{\text{cond}}[i - 1]) M_{\text{vap}}[i - 1] \lambda(T_c[i - 1])$ $+ M_{\text{brine}}[i] (h_{\text{sw}}(T[i - 1], X_b[i - 1]) - h_{\text{vap}}(T'_{\text{vsat}}[i]))$ $+ M_b[i] (h_{\text{sw}}(T[i - 1], X_b[i - 1]) - h_{\text{sw}}(T[i], X_b[i]))$ $= M_d[i] (h_{\text{vap}}(T'_{\text{vsat}}[i]) - h_{\text{sw}}(T[i - 1], X_b[i - 1]))$	Energy balance on a generic heat exchanger
(4.19)	$(1 - \alpha_{\text{cond}}[N - 1]) M_{\text{vap}}[N - 1] \lambda(T_c[N - 1])$ $+ M_{\text{fb}}[N] h_{\text{vap}}(T'_{\text{vsat}}[N])$ $+ M_b[N - 1] h_{\text{sw}}(T[N - 1], X_b[N - 1])$ $= M_b[N] h_{\text{sw}}(T[N], X_b[N])$ $+ M_{\text{vap}}[N] h_{\text{vap}}(T'_{\text{vsat}}[N])$	Energy balance on the last effect
(4.20)	$M_{\text{cw}} c_{p,\text{sw}}(T_{\text{cw}}, X_{\text{feed}}) (T_{\text{cw,out}} - T_{\text{cw,in}}) = M_{\text{vap}}[N] \lambda(T'_c[N])$	Energy balance on the end condenser

Regarding the temperature profiles, six main quantities have to be calculated: temperature of the brine generated in the effect (T), temperature reached by the feed in the preheater of the effect (T_{preh}), temperature of the saturated vapor generated in the effect (T_{vsat}), temperature of the vapor after crossing the demister (T'_{vsat}), temperature of the vapor after crossing the connecting lines (T'_c) and condensation temperature of the vapor in the following effect (T_c). These are interdependent according to the equations (4.6)-(4.9), through the boiling point elevation (BPE) and the pressure drops, which lead to temperature drops ($\Delta T_{demister}$, ΔT_{lines} , ΔT_{grav} , ΔT_{acc}), in the case of saturated vapor. The boiling point elevation is estimated through the Pitzer model, which is valid in a wider range of salinity compared to the other correlations in literature (Pitzer and Mayorga 1973, M. Bialik et al. 2008). The pressure drops are estimated according to some correlations present in literature (ESDU 1993, Shen 2015). Concerning the modelling of the effects, the first effect is the only one which receives heat from an external source (M_s at temperature equal to T_s) and in which the feed (M_{feed} at a concentration equal to X_{feed}) enters after having crossed all the preheaters. The feed is sprayed on a tube bundle, while M_s flows inside the tubes. In this effect, the vapor generated (M_{vap}) is given only by the partial evaporation of the feed (M_d). This crosses the demister and the first preheater, where it partially condenses. The remaining part is sent to the following effect, as the heating steam. The brine generated in the first effect (M_b at a concentration equal to X_b) is sent to the following effect as the feed, sprayed on the external surface of the tube bundle. The intermediate effects' modelling includes the two energy balances on the preheater and on the heat exchanger to know the condensed fraction on the preheater tube surface (α_{cond}) and M_d , respectively (equations (4.17)-(4.18)). Moreover, other two vapor contributions have to be considered: the vapor generated by the inlet brine flash (M_{fbrine} from equation (4.16)) and the vapor coming from the flashing box M_{fb} , which is generated by the flash of the condensed distillate collected in the flashing box (M_{fb} and M_c , the condensate exiting from the flash box, are derived from equation (4.14), (4.15)). Finally, the last effect differs from the others because it does not have any preheater and the entire vapor generated in the last effect is sent to the end condenser, where it condenses completely. This leads to a slightly different expression of the energy balances on the effect (Equation (4.19)) and on the last flashing box, since the total M_{vap} generated in the last effect is condensed in the end condenser and then collected in the flash box. The brine generated in the last effect ($M_b [N]$) constitutes the final brine produced by the plant, while the condensate exiting from the last flash box ($M_c [N]$) constitutes the final distillate. These have to satisfy the global balance in Equations (4.4)-(4.5). Regarding the end condenser, usually, the feed itself is used to condensate the vapor. The necessary total cooling water flow rate (M_{cw}) is calculated through the heat balance reported in Equation (4.20) and the surplus ($M_{cw} - M_{feed}$) is cooled down and can be reused.

As already mentioned, the required steam flow rate M_s is calculated through the minimization loop and this figure is necessary to calculate the thermal energy requirement of the whole system which is defined as the product of the steam flow rate times the latent heat at T_s . For what concerns the electric

energy requirement, this takes into account the energy requirement of the pumps and it is assumed equal to 1.5 kWh_{el}/m³ (Sommariva 2010).

Finally, the areas of the heat exchangers, of the preheaters and of the end condenser are calculated according to Equations (4.21)-(4.24), where DTML_{preh} and DTML_{cond} are the temperature logarithmic mean in the preheater and in the condenser and U_{cond} and U_{evap} are the heat transfer coefficients for the condenser and the evaporator respectively, derived from correlations by El-Dessouky et al. (El-Dessouky et al. 1998)

Table 5: Equations to calculate the heat exchangers, preheaters and end condenser areas of the MED plant.

(4.21)	$A_{hx} [0] = \frac{M_{feed} c_{p,sw} (T_{mean}, X_f) (T[1] - T_{preh}[1]) + M_d[1] \lambda(T_{vsat}[1])}{U_{evap} (T[1]) (T_{steam} - T[1])}$
(4.22)	$A_{hx} [i] = \frac{(1 - \alpha_{cond}[i - 1]) M_{vap}[i - 1] \lambda(T_c[i - 1])}{U_{evap} (T[i]) (T_c[i - 1] - T[i])}$
(4.23)	$A_{preh} [i] = \frac{\alpha_{cond}[i] M_{vap}[i] \lambda(T'_{vsat}[i])}{U_{cond} (T'_{vsat}[i]) DTML_{preh}}$
(4.24)	$A_{cond} = \frac{M_{cw} c_{p,sw} (\overline{T_{cw}}, X_{feed}) (T_{cw,out} - T_{cw,in})}{U_{cond} (T'_c[N]) DTML_{cond}}$

4.2. Thermal Vapour Compressor

In the case of a MED-TVC system, a certain amount of vapor generated in the last effect is not condensed in the end condenser but it is recycled to the first effect as part of the heating steam. More in detail, this is possible using a compression device, such as a thermo-compressor, in which a fraction of the vapor coming from the last effect or from an intermediate (i.e. entrained vapor) is mixed with the vapor coming from an external source (i.e. motive steam). In this work, the entrained vapor is always taken from the last effect. The discharged vapor is rejected as super-heated vapor at a pressure equal to the saturation pressure at $T=T_s$. In order to model the TVC, some correlations reported in literature were employed (El-Dessouki and Ettouney 2002, Hassan and Darwish 2014). Given the pressure of the motive steam P_m , the saturation pressure at T_s (P_s) and the pressure of the entrained vapor (P_{ev} , i.e. the saturation pressure at T_n), it is possible to calculate the compression ratio ($C_R = P_s / P_{ev}$) and the expansion ratio ($ER = P_m / P_{ev}$). Thus, the correlations allow calculating the entrainment ratio ($Ra = M_m / M_{ev}$) and, consequently, the amount of steam, which has to be supplied externally (M_m).

4.3. MED Model Validation

The described model was validated through the comparison with another model, which is present in literature (Ortega-Delgado et al. 2017). The two models are similar in their structure, both of them are employed as design models in which the areas of the heat exchangers and of the preheaters are imposed equal. Moreover, the thermo-physical properties of the salt solutions are estimated as functions of temperature and composition. The main differences consist in the estimation of the Boiling Point Elevation (BPE), which is estimated through the Pitzer model in the present model, in order to be able to cover a wider range of feed and brine salinity. Conversely, in the reference model the correlation reported by Sharqawy et al. for seawater was used (Sharqawy et al. 2010). This last correlation and the Pitzer model shows a good agreement at low concentrations, although the BPE calculated via the Pitzer model is higher, while at concentrations higher than 120 g/kg the correlation by Sharqawy is not valid. Furthermore, the programming method is different, since the present model is implemented in Python and a suitable resolution algorithm had to be developed, while the model by Ortega-Delgado et al. is implemented in Engineering Equation Solver (EES) and a simultaneous solver system is employed, which uses the Newton-Raphson method. For validation purposes, the models were tested within the typical desalination range of concentration (35,000-65,000 ppm) and some simulation analyses, varying the number of effects and the distillate flow rate, were carried out, both for the Forward Feed and for the Parallel Cross arrangement. In the following, the results of the analysis performed varying N for the forward-feed MED-TVC are reported. The input data used for this analysis are reported in Table 6.

Table 6: Input data for the reported validation analysis (variation of N_{effects}).

X_{feed} [ppm]	35,000
X_{brine} [ppm]	65,000
N [-]	variable (4-15)
T_{steam} [°C]	70
$P_{\text{motive steam}}$ [bar]	3.5
T_n [°C]	38
M_{feed} [kg/s]	5

Figure 3 shows a very good agreement between the two models. The slight difference which is reported for higher number of effects is due to the fact that the BPE estimated in the Python model through the Pitzer equations is always higher than the one estimated in the EES model. This determines a slight difference in the areas especially at higher number of effects, where the operating ΔT of each effect is lower. As the number of effects increases, the specific area increases because of the depletion of the driving force which is available for the single effect. At the same time, the higher the number of effects, the higher the thermal efficiency of the system. Therefore, the required motive steam decreases and the GOR increases with N.

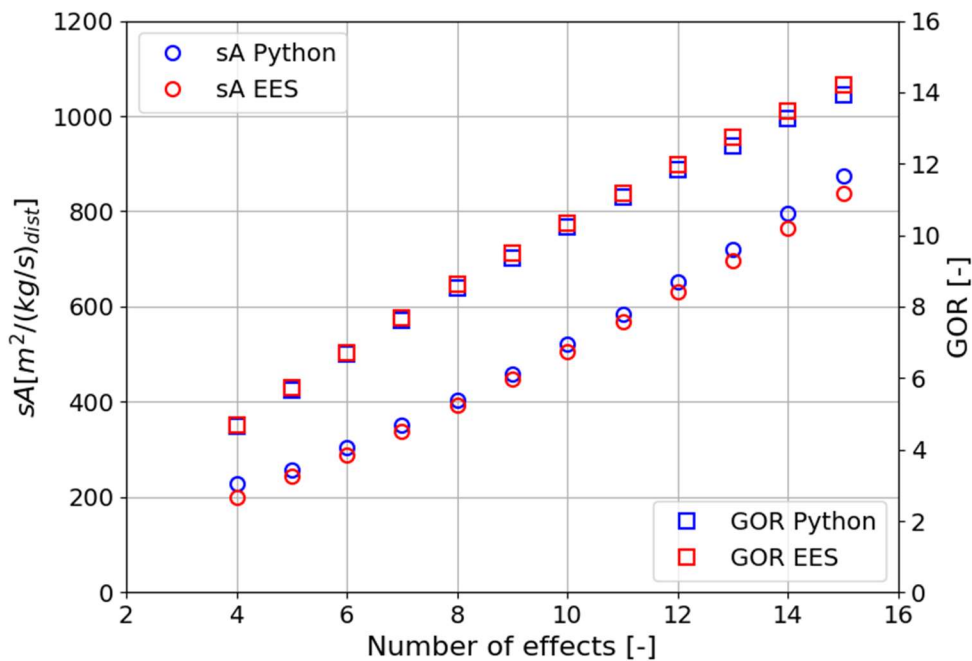


Figure 3: Comparison of the specific area [$\text{m}^2/(\text{kg/s})_{\text{dist}}$] and the GOR [-] as functions of the number of effects for the present model (Python model) and for the reference model (EES model) for the case of a MED-TVC system with a forward-feed arrangement.

4.4. MED Nomenclature

N	number of effects [-]
M	mass flow rate [kg/s]
T	temperature [°C]
X	salinity [ppm]
P	pressure [bar]
A	heat exchanger area [m^2]
sA	specific area [$\text{m}^2/(\text{kg/s})$]
sQ	specific thermal consumption [kJ/kg]
h	specific enthalpy [kJ/kg]
C_p	specific heat [kJ/(kg °C)]
U	overall heat transfer coefficient [kW/(m^2 °C)]
C_R	compression ratio [-]
ER	expansion ratio [-]
Ra	entrainment ratio [-]

Greek letters

λ	latent heat [kJ/kg]
ΔT	temperature difference [°C]
α_{cond}	fraction of vapor condensed in the preheater

Subscripts

feed	feed entering into the first effect
dist	outlet distillate
brine	outlet brine
HX	heat exchanger
preh	preheater
cond	end-condenser
s	total steam
m	motive steam
vap	total vapor generated in the generic effect
d	vapor generated via evaporation
f,brine	vapor generated via the brine flash
fb	vapor generated in the flash box
b	brine solution generated in the generic effect
c	condensed pure water collected in the flash box
cw	cooling water
sw	salt water solution
liq	pure water in the liquid state
vap	pure water in the vapor state
n	last effect index
ev	entrained vapor
_real	fixed distillate flow rate to be produced

Acronyms

MED	Multi-Effect Distillation
TVC	Thermo-vapor compressor
GOR	Gain Output Ratio
FF	Forward Feed
BPE	Boiling Point Elevation [°C]
DTML	Temperature logarithmic mean

5. Reverse Osmosis Model

Reverse Osmosis is one of the most common desalination processes, which is based on a membrane separation under an applied pressure. RO is widely used for seawater desalination to obtain potable water. However, it is effective in treating water at any salinity, from brackish water up to high salinity waters. The technology is commonly present at the industrial scale and several efforts were made to produce highly performing membranes, with very high salt rejection (approx. 99%) and high water flux (Wilf 2007). The most common configuration presents a spiral-wound geometry and the RO plant arrangement consists in a certain number of pressure vessels in parallel, each of those containing a certain number of RO elements in series (typically between 4 and 8) (Vince et al. 2008). Depending on

the operating conditions, e.g. the feed concentration, and on the main objective of the separation, e.g. high purity water as permeate, it is possible to select different configurations, such as single stage, double stage with permeate staging, double or multiple stage with concentrate staging (Malek et al. 1996). Two of the main issues of the RO process regard the concentration polarization and the membrane fouling, which are connected and contribute both in water flux depletion and eventually higher energy consumption. Several methods have been used to reduce these effects, for example increasing the flow rate or promoting turbulence (Jamal et al. 2004). In the literature on RO plant modelling, some analytical models have been developed to estimate the transport phenomena across the RO membrane (Lonsdale et al. 1965, Kimura and Sourirajan 1967). Moreover, commercial software developed by DOW is available and allows the simulation of several membrane elements and configurations. Some studies are also devoted to the comparison between single and multi-stage operations (Malek et al. 1996) or to the optimization of the process configuration (Vince et al. 2008). The model set up for the simulation of the RO process within the Zero Brine project provides the possibility to simulate a single stage or a multi-stage system and it is an optimization model which finds the suitable feed pressure in correspondence to a certain recovery. The model starts from the evaluation of the membrane properties and the calculation of water and salt flux under a certain pressure. Thus, the whole element is taken into account and discretized along the length in a certain number of sub-elements. In each of those, trans-membrane fluxes are calculated and mass balances are applied. Finally, the elements are interconnected to simulate the pressure vessel and the whole plant. The structure of the RO plant, as described by the implemented model, is reported in Figure 4.

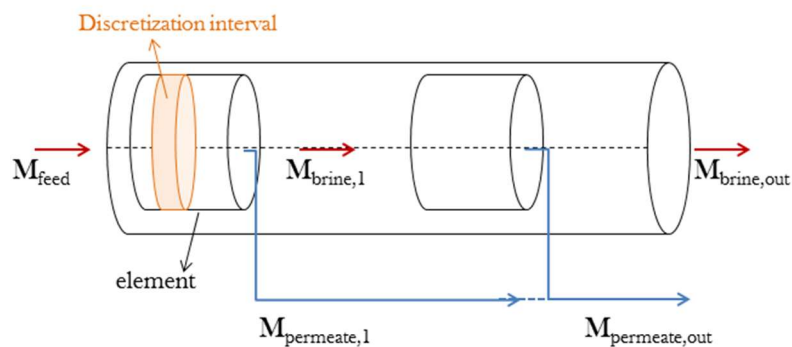


Figure 4: Structure of a single stage RO plant.

5.1. RO Membrane

The model commonly used to simulate the RO membrane performances is a two-parameter solution diffusion model which provides that both water and solute diffuse through the membrane. Their transport is regulated by two parameters: pure water permeability in the membrane (A_{membr}) and solute permeability in the membrane (B_{membr}). Therefore, the water flux (F_w) and the solute flux (F_s) through the membrane are defined as follows:

$$(5.1) \quad F_w = A_{\text{membr}} (\Delta P - \Delta \Pi)$$

$$(5.2) \quad F_s = B_{\text{membr}} (X_{f,w} - X_p) 10^{-6}$$

where ΔP is the transmembrane pressure difference [bar], $\Delta \Pi$ is the transmembrane osmotic pressure difference [bar], $X_{f,w}$ is the feed concentration at the solution-membrane interface [ppm] and X_p is the permeate concentration, which is usually negligible in this expression in comparison with $X_{f,w}$. The osmotic pressure difference is calculated according to the Van't Hoff relation:

$$(5.3) \quad \Delta \Pi = \frac{2 RT \rho}{M_{\text{NaCl}}} 10^{-5} (X_{f,w} - X_p) 10^{-6}$$

where R is the universal gas constant, T is the operating temperature [K], ρ is the solution density [kg/m^3] and M_{NaCl} is the molar mass of NaCl (0.0585 kg/mol). In the case of other components present in the solution, the osmotic pressure depends on the sum of the concentration differences between feed and permeate side divided by the relevant molar mass of the component.

The membrane properties are calculated starting from some data supplied by the membrane produced, as reported for two membranes taken as examples in Table 7.

Table 7: Nominal test conditions for two types of membranes (FILMTEC RO Membranes).

Membrane	Active area [m ²]	Pressure [bar]	Permeate flow rate [m ³ /day]	Rejection [%]	Concentration [ppm]	Salt
SW30XLE-440	40.9	55.2	37.5	99.8	32,000	NaCl
BW30HRLE-440	40.9	10.3	47.9	99.3	2,000	NaCl

The estimation of the nominal membrane properties is performed calculating the osmotic pressure at the test condition and then applying the definition of water and solute flux to calculate $A_{\text{membr,nom}}$ and $B_{\text{membr,nom}}$ respectively.

$$(5.4) \quad \Delta \Pi_{\text{test}} = \frac{2 RT \rho}{M_{\text{NaCl}}} 10^{-5} X_{f,\text{test}} 10^{-6}$$

$$(5.5) \quad A_{\text{membr,nom}} = \frac{F_{w,\text{test}} 1000}{24 \times 3600 A (\Delta P_{\text{test}} - \Delta \Pi_{\text{test}})}$$

$$(5.6) \quad B_{\text{membr,nom}} = \frac{1 - R_{\text{salt}}}{R_{\text{salt}}} A_{\text{membr,nom}} (\Delta P_{\text{test}} - \Delta \Pi_{\text{test}})$$

where $X_{f,\text{test}}$ is the feed concentration in the test condition [ppm], $F_{w,\text{test}}$ is the flow in m^3/day , ΔP_{test} is the transmembrane pressure in the test condition, A is the active area [m^2] and R_{salt} is the membrane salt rejection.

The real values of the membrane properties, i.e. A_{membr} and B_{membr} are calculated by correcting the nominal values with the temperature correction factor (TCF) and the membrane ageing factors (MAF_w and MAF_s), which are calculated as follows:

$$(5.7) \quad \text{TCF} = \frac{1}{e^{C_{\text{membr}} \left(\frac{1}{T} - \frac{1}{298} \right)}}$$

$$(5.8) \quad \text{MAF}_w = (1 - \Delta\Phi_w)^{\text{age}_{\text{membr}}}$$

$$(5.9) \quad \text{MAF}_s = 1 + \Delta\Phi_{s,\text{coeff}} \times \text{age}_{\text{membr}}$$

where C_{membr} is a constant, characteristic of membrane barrier material (around 2,500-3,000 for polyamide membranes (Wilf 2007)), $\text{age}_{\text{membr}}$ is the average life time of the RO membranes (taken equal to 4 years) and $\Delta\Phi_w$ and $\Delta\Phi_s$ are measures of the relative water passage loss and of the relative solute passage increase with time (equal to 0.07 and 0.1 respectively) (Wilf 2007, Moser 2015). Overall, the temperature increase has a positive impact on the membrane performances because the permeability of water is higher and the required pressure decreases. Conversely, the membrane performances decline with time because of the formation of fouling layers and the loss of mechanical stability. For this reason, it is observable a reduction of the water flux and an increase of the salt flux. Finally, the concentration of the feed solution at the feed-membrane interface ($X_{f,w}$) is estimated taking into account the concentration polarization phenomenon, through the following correlation, as a function of the membrane element recovery:

$$(5.10) \quad \text{CPF} = k_p e^{\left(\frac{2 R_{\text{el}}}{2 - R_{\text{el}}} \right)}$$

where the membrane element recovery R_{el} is defined as the ratio between the produced permeate flow rate and the feed flow rate, while k_p is a constant depending on membrane element geometry. The higher R_{el} , the higher CPF because the concentration of the feed increases more sharply in the element.

5.2. RO Element

The RO element is discretized along its length in a certain number of sub-elements (equal to 50, which resulted to be an accurate discretization on the basis of a sensitivity analysis) and for each element the water and salt fluxes are calculated. Thus, the permeate flow rate and composition are estimated as:

$$(5.11) \quad M_{\text{perm}}[i] = (F_w[i] + F_s[i]) \frac{A_{\text{elem}}}{n_{\text{discr}}}$$

$$(5.12) \quad X_{\text{perm}}[i] = \frac{F_s [i]}{F_w [i]} 10^6$$

The fluxes are calculated at the transmembrane pressure and the transmembrane osmotic pressure of the accounted sub-element and the feed pressure is assumed to vary linearly in every element with a pressure drop of each element of 0.5 bar (*Filmtec Reverse Osmosis Membranes Technical Manual* n.d.). The concentrate flow rate and concentration are calculated via mass balances:

$$(5.13) \quad M_{\text{conc}}[i] = M_f[i] - M_{\text{perm}}[i]$$

$$(5.14) \quad X_{\text{conc}}[i] = \frac{X_f[i] M_f[i] - X_{\text{perm}}[i] M_{\text{perm}}[i]}{M_{\text{conc}}[i]}$$

The outlet concentrate flow rate produced in the i element constitutes the inlet feed flow rate of the $i+1$ element.

$$(5.15) \quad M_f[i + 1] = M_{\text{conc}}[i]$$

$$(5.16) \quad X_f[i + 1] = X_{\text{conc}}[i]$$

Finally, the overall distillate produced in the element is the sum of the permeate solutions produced in every sub-element and its composition is calculated via a mass balance:

$$(5.17) \quad M_{\text{perm, out elem}} = \sum_i M_{\text{perm}}[i]$$

$$(5.18) \quad X_{\text{perm, out elem}} = \frac{\sum_i M_{\text{perm}}[i] X_{\text{perm}}[i]}{\sum_i M_{\text{perm}}[i]}$$

Finally, the element recovery can be calculated as:

$$(5.19) \quad R_{\text{el}} = \frac{M_{\text{perm, out elem}}}{M_{\text{feed elem}}} \times 100$$

5.3. RO Plant

The single stage RO plant is given by a certain number of pressure vessels in parallel, each of those presenting RO elements in series. The simulation of the pressure vessel provides the interconnection of the elements, described in the previous section, by the definition of the inlet feed flow rate of every element as the concentrate flow rate produced by the previous element. The permeate flow rate produced by every pressure vessel ($M_{\text{perm, out}}$) is the sum of the permeate solutions produced in every element contained in the vessel. The main performance indicators of the RO plant consist in the overall recovery, the purity of the outlet permeate solution $X_{\text{perm, out}}$ and the electric power consumption P_{RO} [kW] which is dominated by the power demand of the high pressure pump, given by:

$$(5.20) \quad R_{\text{plant}} = \frac{M_{\text{perm,out}}}{M_{\text{feed}}} \times 100$$

$$(5.21) \quad X_{\text{perm,out}} = \frac{\sum_{\text{elem}} M_{\text{perm,out elem}} X_{\text{perm,out elem}}}{M_{\text{perm,out}}}$$

$$(5.22) \quad P_{\text{RO}} = \frac{P_{\text{feed}} 10^5 M_{\text{feed}}}{\rho \eta_{\text{pump}}}$$

where P_{feed} is the applied feed pressure in [bar], ρ is the density of the solution [kg/m^3] and η_{pump} is the efficiency of the high pressure pump [-].

The number of pressure vessels (i.e. the total membrane area available in the stage) can be fixed in the simulation or can be calculated, when a fixed recovery is required, as the ratio between the required total permeate flow rate and the calculated water flux. The model is able to simulate the RO plant when a certain feed pressure and a certain total membrane area are given as inputs and in this case the permeate flow rate and the plant recovery are calculated. More often, the recovery is given as the main requirement and the feed pressure is calculated as a consequence through an optimization tool. The resolution procedure is shown in Figure 5.

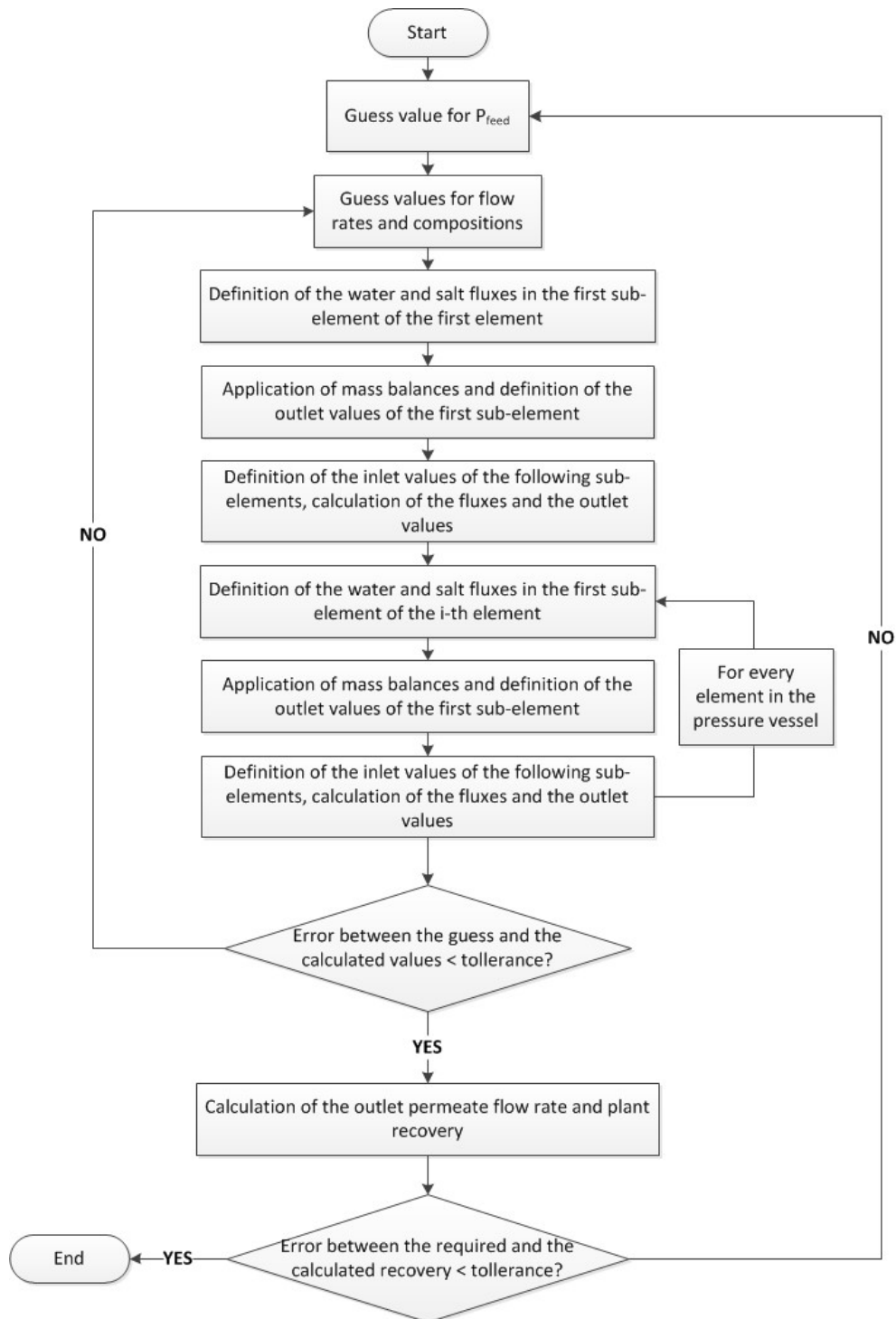


Figure 5: Resolution procedure of the RO plant model.

The resolution of the multi-stage system is analogous and the permeate flow rate produced by the first stage is sent as the feed to the following stage.

5.4. RO Model Validation

Some charts are reported with reference to the validation performed through the comparison with the commercial software WAVE, developed by Dow (www.dow.com/water-and-process-solutions/resources/design-software). Some simulations were performed with a single stage RO plant at different recoveries. The main outputs compared are the required feed pressure and the average permeate water flux. The charts show a very good agreement between the model results and the results produced by Wave, ensuring a good reliability of the model.

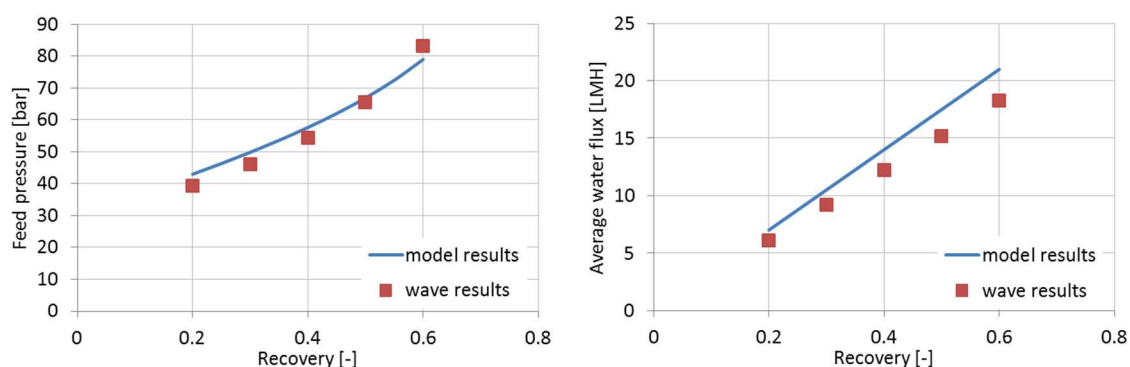


Figure 6: Validation charts: comparison of the feed pressure (on the left) and the average permeate water flux (on the right) calculated by the model and calculated by the WAVE software.

5.5. RO Nomenclature

A_{membr}	pure water permeability in the membrane [kg/(s m ² bar)]
B_{membr}	solute permeability in the membrane [kg/(s m ²)]
F_w	water flux [kg/(s m ²)]
F_s	salt flux [kg/(s m ²)]
T	operating temperature [K]
ΔP	transmembrane pressure difference [bar]
X	concentration [ppm]
R_{salt}	salt rejection [%]
A	membrane active area [m]
C_{membr}	membrane constant for the temperature correction factor [K]
M	flow rate [kg/s]
n_{discr}	number of discretization intervals [-]
R_{el}	element recovery [%]
R_{plant}	plant recovery [%]
P_{feed}	feed pressure [bar]
P_{RO}	electric power consumption [W]
Subscripts	
f,w	feed side at the membrane interface
f	feed side
p	permeate side

feed	feed solution
conc	concentrate solution
perm	permeate solution
perm,out	permeate produced by the plant
perm,out elem	permeate produced by the RO element
w	water
s	salt
elem	discretization element

Greek letters

$\Delta\Pi$	transmembrane osmotic pressure difference [bar]
$\Delta\Phi$	relative variation of the flux with time [-]
ρ	density of the solution [kg/m^3]
η_{pump}	efficiency of the high pressure pump [-]

Acronyms

RO	Reverse osmosis
TCF	Temperature correction factor
MAF	Membrane ageing factor
CPF	Concentration polarization factor
NDP	Net driving pressure [bar]

6. Nanofiltration Model

The NF model is developed on different scales, i.e. the lowest scale describes the mechanisms within the membranes, the medium scale is relevant to the NF element, while the high scale regards the whole NF plant, given by a certain amount of vessels in parallel, each one containing some NF elements in series. The schematic representation of the NF unit, as it is described in the model, is reported in Figure 7.

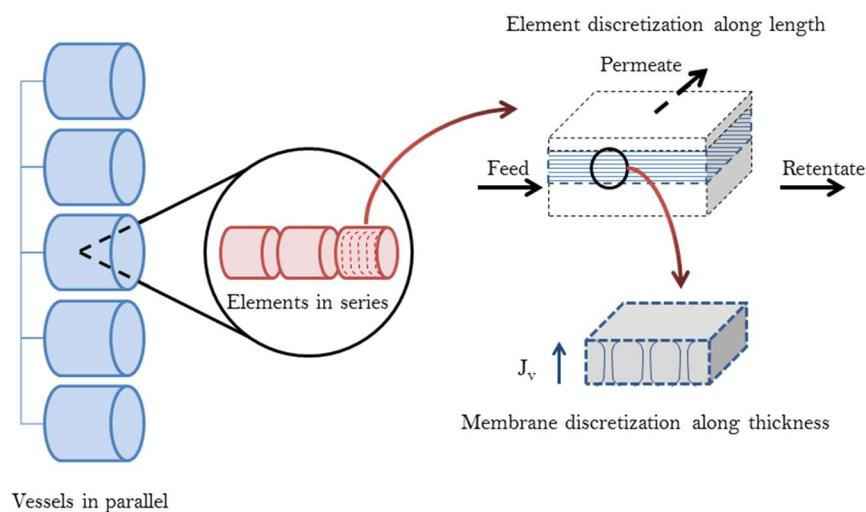


Figure 7: Different scales of modelling of the nanofiltration unit.

6.1. DSMP-DE Membrane Model

Starting from the lowest scale, the mechanisms within the membranes are described via the Donnan Steric Partitioning Model with Dielectric Exclusion (DSMP-DE). In literature, there are numerous studies regarding the modelling of NF membranes and the DSMP model is the most widely used (Bowen et al. 1997, 2004, Geraldes and Alves 2008). The model allows a full characterization of the NF membrane, knowing four parameters, i.e.:

- the membrane pore radius (r_{pore})
- the active thickness (δ_m)
- the dielectric constant within the pores (ϵ_{pore}) and
- the fixed charge density (X_d).

These parameters are necessary for the estimation of the membrane rejection of a species i , being it defined as $1 - C_{pi} / C_{\text{feed}i}$. The system of equations composing the DSMP-DE model is linearized according to (Geraldes and Alves 2008) and solved in Python via the LAPACK routine `_gesv`, which is typically used to solve linear systems. The problem is then solved via iterations, updating the coefficients of the linearized equations and solving the linear system, until the residuals relevant to the imposed conditions are below a user-defined threshold ($<10^{-4}$).

The DSMP-DE model consists in the resolution of the extended Nernst-Planck equation along the thickness of the membrane, which takes into account the three different mechanisms of ion transport, i.e.:

- convection
- diffusion
- electro-migration (Equation 6.1 in Table 8).

The main equations are reported in Table 8, where C_i^b , C_i^{bm} , C_{ij}^m , and C_i^p represent the concentration of the species i in the bulk solution, at the bulk-membrane interface just before entering in the pore, in the j -th interval within the membrane, and in the permeate, respectively. J_i and J_v are the flux of the species i and the solvent (water) convective flux across the membrane. $K_{i,c}$, $k_{i,d}$ are the hindered convective and diffusive mass transfer coefficients of the ions within the pore, depending on λ , i.e. the ratio between the solute radius (r_i) and the pore radius (r_{pore}). $D_{i,p}$ is the diffusivity of the species i within the pore, which is corrected with respect to the diffusivity in the bulk via $k_{i,d}$. $K_{c,i}^{\text{bulk}}$ is the mass transfer coefficient in the bulk, depending on the flow regime, while $k_{c,i}^{\text{bulk}}$ is obtained multiplying the mass transfer coefficient by a factor depending on the permeation flux through the membrane (Geraldes and Afonso 2006).

Table 8: Equations of the implemented DSPM-DE model.

(6.1)	$j_i = J_v C_{i,p} = -D_{i,p} \frac{C_{i,j+1}^m - C_{i,j}^m}{\delta y_j} - \frac{1}{2} z_i (C_{i,j+1}^m + C_{i,j}^m) D_{i,p} \frac{F}{RT} \frac{\psi_{j+1} - \psi_j}{\delta y_j} + \frac{1}{2} k_{i,c} (C_{i,j+1}^m + C_{i,j}^m) J_v$
(6.2)	$k_{i,d} = \frac{1 + \frac{9}{8} \lambda \ln(\lambda) - 1.56034 \lambda + 0.528155 \lambda^2 + 1.91521 \lambda^3 - 2.81903 \lambda^4}{+0.270788 \lambda^5 + 1.10115 \lambda^6 - 0.435933 \lambda^7}$
(6.3)	$k_{i,c} = \frac{1 + 3.867 \lambda - 1.907 \lambda^2 - 0.834 \lambda^3}{1 + 1.867 \lambda - 0.741 \lambda^2}$
(6.4)	$D_{i,p} = k_{i,d} D_{i,\infty}$
(6.5)	$\frac{\gamma_{i,1}^m C_{i,1}^m}{\gamma_{i,1}^{bm} C_{i,1}^{bm}} = \phi_i \phi_B \exp\left(-\frac{z_i F}{RT} \Delta\psi_{D,bm}\right)$
(6.6)	$\frac{\gamma_{i,N}^m C_{i,N}^m}{\gamma_{i,1}^p C_{i,1}^p} = \phi_i \phi_B \exp\left(-\frac{z_i F}{RT} \Delta\psi_{D,pm}\right)$
(6.7)	$\ln \gamma = -A z_i^2 \left(\frac{\sqrt{I}}{1 + \sqrt{I}} - 0.3 I \right)$
(6.8)	$A = \frac{e_0^3 N_A^{1/2}}{\ln(10) 4\pi \sqrt{2} (\epsilon k_B T)^{3/2}}$
(6.9)	$\phi_B = \exp\left(-\frac{\Delta W_i}{k_B T}\right)$
(6.10)	$\Delta W_i = \frac{z_i^2 e_0^2}{8\pi \epsilon_0 r_i} \left(\frac{1}{\epsilon_{pore}} - \frac{1}{\epsilon_{bulk}} \right)$
(6.11)	$\phi_i = (1 - \lambda_i)^2$
(6.12)	$\sum_i z_i C_i^{bm} = 0$
(6.13)	$\sum_i z_i C_i^p = 0$
(6.14)	$\sum_i z_i C_{i,j}^m + X_d = 0$
(6.15)	$j_i = -k_{c,i}^{bulk} (C_i^{bm} - C_i^b) + J_v C_i^{bm} - z_i C_i^{bm} D_{i,\infty} \frac{F}{RT} \xi$
(6.16)	$k_{c,i}^{bulk} = k_{c,i}^{bulk} \Xi = k_{c,i}^{bulk} \left[\frac{J_v}{k_{c,i}^{bulk}} + \left(1 + 0.26 \left(\frac{J_v}{k_{c,i}^{bulk}} \right)^{1.4} \right)^{-1.7} \right]$

The resolution provides the ion partitioning at the two membrane interfaces (equation 6.5 for the bulk-membrane interface and equation 6.6 for the permeate-membrane interface), which is determined by

the Donnan equilibrium, the steric effect due to the sieving effect of the membrane (evaluated via the coefficient Φ_i , calculated via equation 6.11) and the dielectric exclusion (estimated through the coefficient Φ_B , i.e. the Born solvation contribution for partitioning, see equations 6.9-6.10). This last effect was widely investigated in literature, since it has a prominent role in the definition of the ion rejection (Vezzani and Bandini 2002, Oatley et al. 2012). In fact, the dielectric exclusion is mainly due to the variation of the solvent dielectric properties inside the pores, caused by an alteration of the solvent structure. This different dielectric constant of the solvent inside the pores gives rise to a barrier to ion solvation, which constitutes an additional exclusion term. In the interface equilibrium, the concentrations are multiplied by the activity coefficient γ , to take into account the non-ideality of the solutions, estimated via the Davies equations (6.7-6.8). Other conditions which have to be fulfilled are the electroneutrality on the bulk and on the permeate side and inside the membrane, where a fixed charge density X_d is present (Equation 6.12, 6.13, 6.14 respectively). Finally, the mass transfer resistance on the bulk side is taken into account to calculate the concentration of the ions on the bulk-membrane interface (just before entering into the pore). Therefore, the balance in equation 6.15 represents the solute flux from the bulk to the membrane and it is used to estimate the role of the concentration polarization. This effect is neglected on the permeate side.

The mass transfer coefficient in the bulk is estimated via the correlation developed for spiral wound membranes, reported in equation 6.17 (Senthilmurugan et al. 2005).

$$(6.17) \quad k_{c,i}^{\text{bulk}} = 0.753 \left(\frac{\eta_{\text{mix}}}{2 - \eta_{\text{mix}}} \right)^{1/2} \left(\frac{D_{i,\infty}}{h_f} \right) Sc^{-1/6} \left(\frac{Pe_i h_f}{L_{\text{mix}}} \right)^{1/2}$$

where η_{mix} is the mixing efficiency of the spacer, h_f is the height of the feed channel, L_{mix} is the mixing length of the spacer, Pe and Sc are the Peclet and the Schmidt dimensionless numbers respectively, i.e. $Pe = \frac{2 h_f u_w}{D_{i,\infty}}$ and $Sc = \frac{\eta}{\rho D_{i,\infty}}$.

Finally, ψ represents the electric potential across the membrane, ξ the electric potential gradient at the bulk-membrane interface, outside the electric double layer, and $\Delta\psi_{\text{bm}}$ and $\Delta\psi_{\text{pm}}$ represent the potential difference at the bulk-membrane interface and at the permeate-membrane interface, respectively.

The solvent flux J_v through the membrane is estimated via Hagen-Poiseuille relation, depending on the membrane geometric parameters and on the net driving pressure:

$$(6.18) \quad J_v = \frac{\Delta P r_{\text{pore}}^2}{8 \eta \delta_m}$$

where η is the solution viscosity, δ_m is the active membrane thickness and ΔP is given by the difference between the pressure difference between bulk and permeate channel and the osmotic pressure $\Delta\Pi$, given by equation 6.19.

$$(6.19) \quad \Delta\Pi = RT \sum_i (C_i^{\text{bm}} - C_i^{\text{p}})$$

6.2. NF Element and Plant Model

The DSPM-DE model is integrated for the resolution of a whole NF element, discretizing the length of the membrane and applying mass balances to every interval. As shown by Roy et al. (Roy et al. 2015), also for a spiral wound element it is possible to apply a one-dimensional model, without significant errors, since the variation of the permeate concentration and flow rates along the width of the membrane is negligible. Consequently, an iterative one-dimensional model is employed, in which for every discretization interval the average value of the concentration, flow rates and pressure within the interval are accounted for the calculation of the osmotic pressure and the bulk mass transfer coefficient. The mass balances implemented to estimate the output concentrations and flow rates, together with the pressure losses definition along the element (Roy et al. 2015), are reported in Table 9.

Once the single element is modelled, to switch to an industrial NF plant scale, a certain number of elements are put in series inside a vessel. More in detail, the concentrate flow rate produced by one element is fed to the following element, while the produced permeates are finally mixed together. Moreover, typically, many pressure vessels are arranged in parallel to achieve a certain recovery rate ($M_{p,out} / M_{feed}$), which corresponds to a required permeate flow rate. Thus, for the overall plant resolution, an iterative calculation is set up, in which a guess number of vessels, i.e. a guess total membrane area, is given through the ratio between the required permeate flow rate and a guessed average solvent flow rate through the membrane. Thus, the series of elements is solved, the average solvent flux is recalculated in relation to the net driving pressure along the elements, and the total recovery rate is calculated. At this point, the number of pressure vessels is updated and the iterative calculation stops as soon as the overall recovery ratio is higher than or equal to the required one. This last iterative procedure needs only a few iterations but it is necessary, since the solvent flux through the membrane changes significantly along the membrane length and from one element to another and accounting only the flux at the first element entrance would lead to a strong underestimation of the required vessels, with important economic consequences.

Table 9: Equations to model a nanofiltration element.

(6.20)	$M_p[x] = M_p[x - 1] + J_v[x] \frac{A_{membra,tot}}{n_{elem}n_{discr,L}}$
(6.21)	$M_{ret}[x] = M_b[x] - J_v[x] \frac{A_{membra,tot}}{n_{elem}n_{discr,L}}$
(6.22)	$C^p_i[x] = \frac{C^p_i[x - 1]M_p[x - 1] + j_i[x] \frac{A_{membra,tot}}{n_{elem}n_{discr,L}}}{M_p[x]}$

$$(6.23) \quad C_{ret,i}^{ret}[x] = \frac{C_{b,i}^{b}[x]M_b[x] - j_i[x] \frac{A_{membr,tot}}{n_{elem}n_{discr,L}}}{M_{ret}[x]}$$

$$(6.24) \quad M_b[x] = M_{ret}[x - 1]$$

$$(6.25) \quad C_{b,i}^{b}[x] = C_{ret,i}^{ret}[x - 1]$$

$$(6.26) \quad P[x] = P[x - 1] - \Delta P_{losses} = P[x - 1] - \frac{f dx}{2 D_H} \rho_w u_w^2$$

$$(6.27) \quad f = \frac{6.23}{Re^{0.3}}$$

where M_p and C_{pi} are the mass flow rate and the concentrations in the permeate channel, M_{conc} and C_{conci} are the flow rate and the concentrations in the concentrate channel, which are equal to the feed flow rate and the concentration of the feed in the next interval (M_b and C_{bi}). Regarding the pressure losses definition, f is the friction factor, dx is the length of the discretization interval, D_H is the hydraulic diameter relevant to the feed channel, employed also in the calculation of Re , and u_w is the feed velocity.

Finally, also in the case of the NF plant, the electric power requirement is calculated in analogy with the RO plant (Equation 5.22) and it is given by the power demand of the feed pump.

6.3. NF Model Validation

The DSPM-DE model was validated via the comparison with some experimental results reported in literature for two different salt solutions in presence of NF270 membranes (Oatley et al. 2012). The membrane parameters employed for the validation were taken equal to the ones taken in the reference work. As shown in Figure 8, there is a very good agreement between the experimental and the model results for both cases.

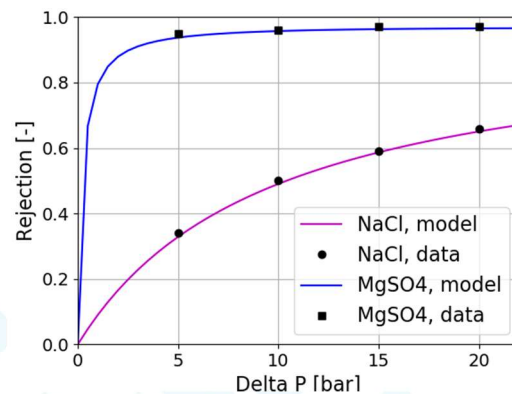


Figure 8: Rejection experimental values (black dots) (Oatley et al. 2012) and trend simulated by the model in presence of NaCl or MgSO₄ with NF270 membranes.

6.4. NF Nomenclature

J_v	water flux through the NF membrane [m/s]
r_{pore}	NF membrane pore radius [nm]
X_d	NF membrane charge density [mol/m ³]
r_i	ion radius [nm]
C	concentration [mol/m ³]
x	direction of the feed flow in the NF element
y	direction across the membrane from the feed to the permeate side
M	flow rate [m ³ /s]
j_i	flux of the ion i [m/s]
$A_{\text{membr,tot}}$	total membrane area for each vessel (6 elements with a area of 1x1m ²) [m ²]
n_{elem}	number of elements in each vessel
$n_{\text{discr,L}}$	number of discretization intervals along the NF element length
n_{vessel}	number of vessels in parallel
P	pressure [bar]
ΔP_{losses}	pressure losses along the element [bar]
ΔP	net driving pressure [bar]
f	friction factor [-]
dx	length of the discretization interval [m]
D_H	hydraulic diameter relevant to the feed channel [m]
Re	Reynolds number
Pe	Peclet number
Sc	Schmidt number
u_w	feed velocity [m/s]
$k_{i,c}$	hindered convective mass transfer coefficients of the ions within the pore
$k_{i,d}$	hindered diffusive mass transfer coefficients of the ions within the pore
$D_{i,p}$	diffusivity of the species i within the pore [m ² /s]
$D_{i,\infty}$	diffusivity of the species i in the bulk [m ² /s]
$k_{c,i}^{\text{bulk}}$	mass transfer coefficient in the bulk [m/s]
$k'_{c,i}^{\text{bulk}}$	corrected mass transfer coefficient in the bulk [m/s]
z	ion valence
F	Faraday constant (9.64867 x 10 ⁴ C/eq)
R	ideal gas constant (8.314 J/(K mol))
T	Temperature [K]
N_A	Avogadro constant (6.023 x 10 ²³ mol ⁻¹)
k_B	Boltzmann constant (1.38066 x 10 ⁻²³ J/K)
e_0	electronic charge (1.602 x 10 ⁻¹⁹ C)
A	temperature correction factor for the activity coefficient
I	ionic strength [mol/l]
h_f	height of the NF feed channel [m]
L_{mix}	mixing length of the spacer [m]

Greek letters

δ_m	NF membrane active layer thickness [μm]
ϵ_{pore}	dielectric constant within the pore
ϵ_{bulk}	dielectric constant in the bulk
ϵ_0	vacuum permittivity (8.854×10^{-12} F/m)
ϵ	medium permittivity [F/m]
$\Delta\Pi$	osmotic pressure [bar]
ρ_w	solvent density [kg/m^3]
γ	activity coefficient
η	solution viscosity [Pa s]
λ	ratio between the solute radius and the pore radius
ψ	electric potential across the membrane [V]
ξ	electric potential gradient at the bulk-membrane interface [V]
$\Delta\psi_{D,bm}$	Donnan potential difference at the bulk-membrane interface [V]
$\Delta\psi_{D,pm}$	Donnan potential difference at the permeate-membrane interface [V]
Φ_i	steric coefficient
Φ_B	Born solvation contribution for partitioning
η_{mix}	mixing efficiency of the spacer
ΔW	Born solvation energy barrier [J]
ξ	correction factor for the mass transfer coefficient

Subscripts and superscripts

i	ion index
j	index for the discretization within the membrane thickness
p	NF permeate along the NF element
ret	NF retentate along the element
m	inside the membrane
feed	solution entering into the element
out	outlet of the NF unit
b	solution entering into the interval along the NF element
bm	bulk-membrane interface

Acronyms

TVC	Thermo-vapor compressor
NF	Nanofiltration
DSPM-DE	Donnan Steric Partitioning Model with Dielectric Exclusion

7. Crystallizer Model

In literature, there are many studies related to the recovery of magnesium from brines, reporting several experimental campaigns aiming at controlling the purity and the crystals size distribution of precipitate particles (Turek and Gnot 1995, Liu et al. 2011, Cipollina et al. 2014). However, only a few studies are devoted to modelling the crystallization of $\text{Mg}(\text{OH})_2$. With this regard, a fundamental work was carried out by Alamdari et al. (Alamdari et al. 2008), in which the kinetics of secondary nucleation, growth and agglomeration were estimated via the fitting of experimental data obtained for a batch and a semi-batch seeded reactor.

Generally speaking, the crystallization is modelled via population balance equations, which are able to describe the properties of the particles in space and time. The population balance equation takes into account the different mechanisms occurring inside the crystallizer, i.e. nucleation, growth and aggregation, estimating the variation of the number density function $n(L, t)$, according to the following expression (Omar and Rohani 2017):

$$(7.1) \quad \frac{\partial n(L, t)}{\partial t} = - \frac{\partial [G(L) n(L, t)]}{\partial L} + B(L, t) - D(L, t)$$

where L is the particle length, $G(L)$ is the growth rate, $B(L, t)$ is the birth rate due to the aggregation and $D(L, t)$ is the death rate due to the aggregation. In this case, the breakage of the crystals is neglected.

The population balance equation can be solved following different approaches; one of the most widely used involves the conversion of the population balance into a moment balance. In particular, an attractive option is the quadrature method of moments (QMOM), which is robust and able to handle complex systems, including aggregation and breakage mechanisms (Marchisio et al. 2003b). This method is based on a quadrature approximation, which changes the integral in the moments' definition into a summation.

$$(7.2) \quad m_k = \int_0^{+\infty} n(L) L^k dL \sim \sum_{i=1}^{N_q} w_i L_i^k$$

where N_q is the number of quadratures ($N_q=3$ was shown to be sufficient to describe the moments evolution accurately), w_i are the weights and L_i are the abscissas. The calculation of weights and abscissas is performed via the product-difference algorithm, for which it is necessary to know the first $2N_q$ moments. Thus, to follow the evolution of the moments with time, starting from a known set of the first six orders moments at t_0 , it is possible to apply the balance of the moments, taking into account the occurring mechanisms, to calculate the moments at t_1 . These moments are, then, employed to calculate the weights and the abscissas via the product-difference algorithm, which are useful to estimate the kinetics at t_1 .

For the time being, the attention is focused on the balances on the third moment, which is a measure of the mass of precipitated crystals (M_T).

To this aim, the primary and secondary nucleation kinetics, together with the growth rate, were accounted for the estimation of the M_T variation. The agglomeration kernel was not included, since it does not influence the total mass of crystals but only the crystal size (Marchisio et al. 2003a). The secondary nucleation and growth kinetics are function of the system supersaturation and of M_T , according to the expression given by Alamdari. However, the secondary nucleation depends on the supersaturation with an exponent (b in equation 7.5) equal to 2, instead of 3 as found by Alamdari. This is due to a fundamental difference between the two systems arrangement, which leads to a much higher supersaturation in the system under investigation.

Table 10: Crystallization kinetics and precipitated crystal mass balance.

(7.3)	$S = \frac{[Mg^{++}][OH^-] - K_{sp,Mg(OH)_2}}{K_{sp,Mg(OH)_2}}$
(7.4)	$N_{prim} = k_{prim} \exp\left(-\frac{16\pi v^2}{3 k_B^3 T^3 (\ln S)^2}\right)$
(7.5)	$N_{sec} = k_{sec} S^b M_T$
(7.6)	$G_v = 3k_g k_v^{1/3} S^g v^{2/3} 10^{-6}$
(7.7)	$\frac{dM_T}{dt}_{nucl} = (N_{prim} \rho_{solv} + N_{sec} \rho_{sol}) dV \rho_{cryst} v_{nucl} 10^6$
(7.8)	$\frac{dM_T}{dt}_{growth} = G_v \rho_{cryst}$
(7.9)	$\frac{dM_T}{dt}_{tot} = \frac{dM_T}{dt}_{nucl} + \frac{dM_T}{dt}_{growth}$

where $K_{sp,Mg(OH)_2}$ is the solubility product of $Mg(OH)_2$. N_{prim} [$\#/(g_{solv} s)$], N_{sec} [$\#/(g_{sol} s)$] and G_v [cm^3/s] are the primary nucleation, secondary nucleation and volume-based growth rate, respectively. In equation 7.4, k_{prim} is assumed to be equal to 12 [$\#/(g_{solv} s)$], on the basis of experimental data, v is the volume of one solute molecule [m^3] and σ is the crystal solution interfacial energy, equal to 0.123 J/ m^2 for $Mg(OH)_2$. In equations 7.5 and 7.6, k_{sec} is equal to 0.418 [$\#/(g_{cryst} s)$], k_g is $2.13 \cdot 10^{-11}$ [m/s], k_v is the volume shape factor of the particle and v is the average particle size [m^3]. Finally, v_{nucl} is the minimum particle size and $(dM_T/dt)_{nucl}$, $(dM_T/dt)_{growth}$ and $(dM_T/dt)_{tot}$ are the measure of the increase of the mass of precipitated crystals due to nucleation, growth and total in [g_{cryst}/s].

Different possible crystallizer reactors may be used, for example a batch crystallizer is typically used also at the industrial scale but mostly for small production volumes. In this case, a plug-flow arrangement with different alkaline solution injections was selected, in order to be able to deal with higher volumetric flow rates and to avoid too high supersaturations. The length of the reactor was divided into different elements, as many as the injections and each element was discretized into n intervals. Two discretization steps are employed for each element, since the extremely high supersaturation occurring at the NaOH-solution inlet made necessary to apply a very narrow discretization step ($10^{-6}m$), while after the supersaturation fall a discretization step of $10^{-2}m$ was accounted. In the first interval of each element the total flow rate was increased by the corresponding entering NaOH solution, while, in the rest of the element, the flow rate was constant. The schematic representation of the analysed system is reported in Figure 9.

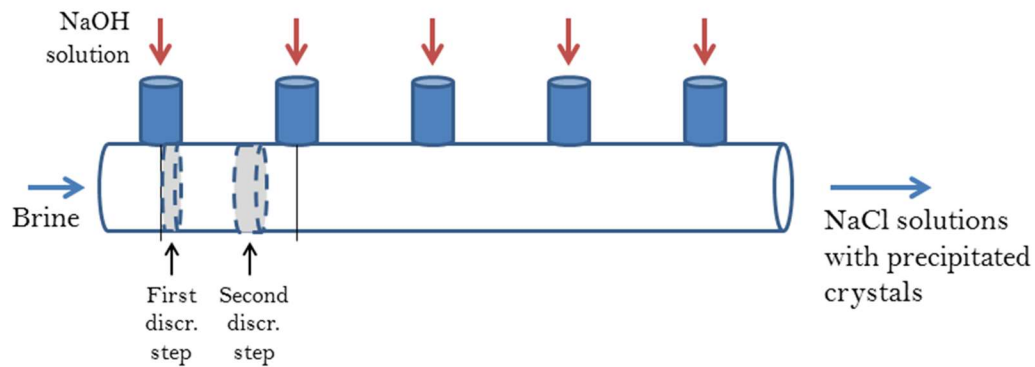


Figure 9: Schematic representation of the plug-flow reactor used for the crystallization step.

For each interval, the kinetics and the M_T generation speed were estimated and used for the evaluation of the concentration of Mg^{++} and OH^- , as shown in the equations 7.10 and 7.11. In equation 7.12, the balance on the OH^- concentration in the first interval of each element is reported, while the balance on the Mg^{++} concentration does not change. Finally, since the reactor is unseeded, in the first interval of the first element only the primary nucleation has to be accounted.

$$(7.10) \quad [Mg^{++}][x] = \frac{Q_{brine}[x-1][Mg^{++}][x-1]10^{-3} - \frac{dM_T}{dt}_{tot} \frac{60}{MW_{Mg(OH)_2}}}{Q_{brine}[x]10^{-3}}$$

$$(7.11) \quad [OH^-][x] = \frac{Q_{brine}[x-1][OH^-][x-1]10^{-3} - 2 \frac{dM_T}{dt}_{tot} \frac{60}{MW_{Mg(OH)_2}}}{Q_{brine}[x]10^{-3}}$$

$$(7.12) \quad [OH^-][x] = \frac{Q_{NaOH}[OH^-]_{in}10^{-3} + Q_{brine}[x-1][OH^-][x-1]10^{-3} - 2 \frac{dM_T}{dt}_{tot} \frac{60}{MW_{Mg(OH)_2}}}{Q_{brine}[x]10^{-3}}$$

where Q_{brine} is the flow rate proceeding along the reactor in [ml/min], Q_{NaOH} is the flow rate of alkaline solution for each injection and $[OH^-]_{in}$ is its concentration in [mol/l]. Finally, $[Mg^{++}]$ and $[OH^-]$ are the concentration in the brine along the reactor in [mol/l].

However, because of the very low solubility of the two hydroxides, it is generally observed that a conversion of 100% occurs in the reactors. For this reason, for the first simulations of the $Mg(OH)_2$ and $Ca(OH)_2$ crystallizers, a conversion of 100% was assumed in both reactors. Consequently, trivial mass balances were implemented to convert the total inlet molar flow rate of Mg^{++} and Ca^{++} into an outlet molar flow rate of $Mg(OH)_2$ and $Ca(OH)_2$. The other relevant calculation, also performed via mass balances, regards the alkaline solution flow rate required for the two separation stages. The required molar flow rate is estimated multiplying the entering molar flow rates of Mg^{++} and Ca^{++} , coming from

the nanofiltration, by the stoichiometric coefficient (i.e. 2) and considering an excess defined through mass balances, which allows reaching a pH equal to 13. The volume flow rate is estimated assuming a concentration of the NaOH solution equal to 1 mol/l.

7.1. Crystallizer Nomenclature

L	particle length [m]
$G(L)$	growth rate
$B(L, t)$	birth rate
$D(L, t)$	death rate
N_q	number of quadratures
w_i	weights
L_i	abscissas
M_T	mass of precipitated crystals [g]
$K_{sp, Mg(OH)_2}$	solubility product of $Mg(OH)_2$
N_{prim}	primary nucleation rate [$\#/(g_{solv} s)$]
N_{sec}	secondary nucleation rate [$\#/(g_{sol} s)$]
G_v	volume-based growth rate [cm^3/s]
k_v	volume shape factor of the particle [-]
v	average particle size [m^3]
v_{nucl}	minimum particle size [m^3]
Q_{brine}	flow rate proceeding along the reactor [ml/min]
Q_{NaOH}	flow rate of alkaline solution for each injection [ml/min]
$[OH^-]_{in}$	NaOH concentration in the alkaline solution [mol/l]
$[Mg^{++}]$	concentration of Mg^{++} in the brine [mol/l]
$[OH^-]$	concentration of OH^- in the brine [mol/l]

8. Membrane Distillation Model

Membrane Distillation is a separation process, which makes use of a microporous hydrophobic membrane, permeable only to the water vapor. The driving force of the separation mechanism is the vapor pressure difference, given by a temperature difference, at the two membrane interfaces. This driving force leads to a net water flux, in the vapor phase within the pores, from the hot channel, where the feed solution flows, to the cold channel, where the permeate solution flows. In the last years, the MD process has been subject of several studies in literature, because of its high potentialities for desalination: for example, it requires lower temperatures and smaller footprint than the Multi-Effect Distillation plants, it is very suitable in the case of low-grade waste heat availability and it works at much lower pressures than the Reverse Osmosis. Moreover, since the separation occurs by evaporation of water at the hot interface and by condensation of the vapor at the cold interface, theoretically, the rejection to any solute is 100% (Al-Obaidani et al. 2008). The main issue of the MD process regards a non-ideality phenomenon, namely the temperature polarization. Therefore, the

driving force for the vapor flux depends on the temperature difference at the two interfaces ($T_{\text{membrane,hot}} - T_{\text{membrane,cold}}$) and these temperatures are different from those relevant to the bulk side, because of the temperature polarization phenomenon (Qtaishat et al. 2008). Another drawback of the MD process is that the water flux is relatively low, compared with other technologies as RO, and the heat lost by conduction is significant, thus the thermal energy requirement is typically very high (Alkhudhiri et al. 2012). Several configurations of the MD unit have been proposed in order to reduce these drawbacks: the most widely used configuration is the Direct Contact MD (DCMD), where both hot and cold fluids are in direct contact with the membrane on the two sides; other configurations present an air gap between the membrane and a cold condensing plate (AGMD) or a cold sweep gas which substitute the cold permeate and provides the driving force (SGMD) or the vacuum applied on the permeate side to enhance the pressure difference (VMD). These configurations are schematically represented in Figure 10.

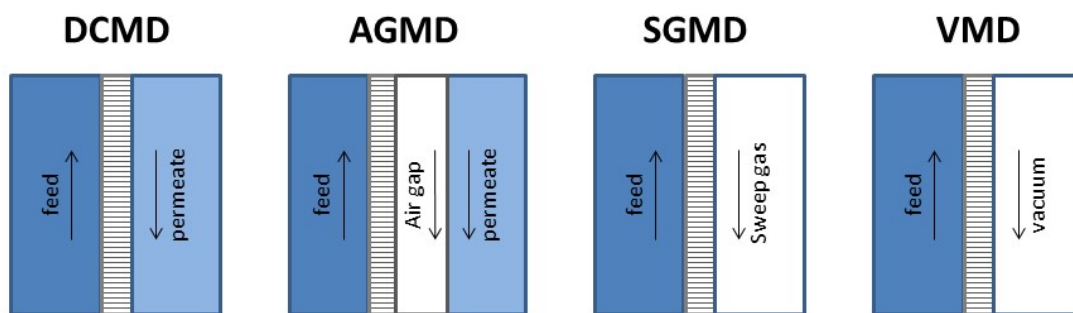


Figure 10: Schematic representation of some of the most widely used MD configurations.

All these configurations have advantages and disadvantages, for example the AGMD ensures a higher heat recovery but the mass transfer is limited by the air gap, or the VMD has negligible heat losses and high fluxes but the electric consumption increases sharply for the vacuum pump (Eykens et al. 2016). Overall, even if the DCMD reports high heat losses for conduction, it was chosen for the present work because of its operational simplicity, the possibility to operate in any configuration (e.g. flat sheet or spiral wound), and its high flux (Al-Obaidani et al. 2008).

8.1. DCMD Element Model – Heat and Mass Transfer

Firstly, the DCMD element was modelled through the description of the heat and mass transfer in the channels and across the membranes. The system presents a single membrane, which is in contact with a hot fluid (feed) on one side and with a cold fluid (permeates) on the other side, as shown in Figure 11. The membrane presents micro pores, which cross the whole thickness of the membrane and at both ends of the pores a liquid/vapor interface is generated. Different heat and mass transport mechanisms are involved: a convective heat and mass flux from the feed bulk to the feed-membrane interface and from the permeate-membrane interface to the permeate bulk, a conductive heat flux

within the pores and the vapor diffusion through the pores, which is coupled with the latent heat transport. The combination of these mechanisms gives rise to a temperature profile from the feed bulk to the permeate bulk, where the temperature polarization effect is evident, i.e. the temperature at the bulk membrane interface ($T_{m,hot}$) is lower than the temperature in the bulk ($T_{bulk,hot}$) and the temperature at the permeate membrane interface ($T_{m,cold}$) is higher than the temperature in the permeate bulk ($T_{bulk,cold}$). Also in the concentration profile, a similar effect is noticed, namely the concentration polarization effect, which leads to a concentration at the bulk membrane interface higher than the one in the bulk. These two phenomena are detrimental for the water flux, since they both contribute to the decrease of the driving force across the membrane.

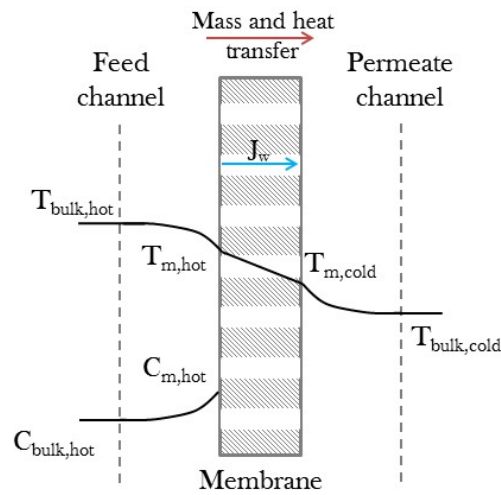


Figure 11: Representation of the DCMD element with the temperature and concentration profile.

8.1.1. Heat Transfer

For what concern the heat transfer, this accounts for different terms: the convective heat flux from the feed bulk to the feed-membrane interface ($Q_{conv,hot}$), the total heat flux through the membranes, i.e. the sum of the conductive flux ($Q_{cond,m}$) and the latent heat transferred with the vapor flux ($Q_{evap,m}$), and the convective heat flux from the permeate-membrane interface to the permeate bulk ($Q_{conv,cold}$). For the conservation of energy under steady-state conditions, these three heat fluxes have to be equal (Khalifa et al. 2017). The definition of the heat fluxes is reported in equation (8.1-8.5).

$$(8.1) \quad Q_{conv,hot} = h_f(T_{bulk,hot} - T_{m,hot})$$

$$(8.2) \quad Q_m = Q_{cond,m} + Q_{evap,m}$$

$$(8.3) \quad Q_{cond,m} = h_m(T_{m,hot} - T_{m,cold})$$

$$(8.4) \quad Q_{\text{evap},m} = J_w \Delta H_{\text{evap}} \left[\frac{T_{m,\text{hot}} + T_{m,\text{cold}}}{2} \right]$$

$$(8.5) \quad Q_{\text{conv},\text{cold}} = h_p (T_{m,\text{cold}} - T_{\text{bulk},\text{cold}})$$

where h_f , h_m and h_p are the heat transfer coefficients in the hot channel, in the membrane and in the cold channel, respectively [$\text{W}/(\text{m}^2 \text{K})$]. J_w is the water flux through the membrane [$\text{kg}/(\text{m}^2 \text{s})$] and ΔH_{evap} is the latent heat of vaporization of water [J/kg], calculated at the average temperature inside the membrane.

From the equality of the heat fluxes, it is possible to calculate directly the temperature at the bulk membrane interface and at the permeate membrane interface, according to the following equations (Khayet et al. 2004):

$$(8.6) \quad T_{m,\text{hot}} = \frac{\frac{k_m}{\delta_m} \left(T_{b,\text{cold}} + \frac{h_f}{h_p} T_{b,\text{hot}} \right) + h_f T_{b,\text{hot}} + J_w \Delta H_{\text{evap}}}{\frac{k_m}{\delta_m} + h_f + k_m \frac{h_f}{h_p \delta_m}}$$

$$(8.7) \quad T_{m,\text{cold}} = \frac{\frac{k_m}{\delta_m} \left(T_{b,\text{hot}} + \frac{h_p}{h_f} T_{b,\text{cold}} \right) + h_p T_{b,\text{cold}} + J_w \Delta H_{\text{evap}}}{\frac{k_m}{\delta_m} + h_p + k_m \frac{h_p}{h_f \delta_m}}$$

where k_m is the membrane conductivity [$\text{W}/(\text{m K})$] and δ_m is the membrane thickness [m]. The membrane conductivity is calculated combining the conductivity of air (k_{air}) and the conductivity of the polymeric structure ($k_{\text{membr},\text{pol}}$) through the membrane porosity ε , according to the following equation:

$$(8.8) \quad k_m = \varepsilon k_{\text{air}} + (1 - \varepsilon) k_{\text{membr},\text{pol}}$$

The heat transfer coefficients in the hot and in the cold channel (h_f and h_p) are estimated starting from the Nusselt number, according to the equation:

$$(8.9) \quad h = \frac{\text{Nu } k}{D_h}$$

where D_h is the hydraulic diameter of the channel and k is the thermal conductivity of the fluid. Several correlations are reported in literature for the calculation of the Nusselt number as function of the Reynolds and the Prandtl number and for the two flow regimes (typically laminar if $\text{Re} < 2,300$ and turbulent if $\text{Re} > 2,300$). These correlations are also dependent on the specific system geometry, which is represented through the hydraulic diameter of the channel. Re and Pr numbers are defined as follows:

$$(8.10) \quad \text{Re} = \frac{\rho v D_h}{\mu}$$

$$(8.11) \quad Pr = \frac{C_p \mu}{k}$$

where μ is the dynamic viscosity of the fluid, v is the fluid velocity in the channel and C_p is the fluid specific heat. Some of these correlations are reported in the table below, where L is the channel length. Among these correlations, in the present work, the equations 8.12 and 8.17 have been used in presence of laminar or turbulent flow respectively, for both channels. This selection was performed on the basis of the validation of the model through the comparison with the experimental results reported by Hitsov et al. (Hitsov et al. 2017, 2018).

Table 11: Literature correlations for the estimation of Nu number in the feed and permeate channels.

(8.12)	$Nu = 0.13 Re^{0.64} Pr^{0.38}$	Laminar flow (Andrjesdottir et al. 2013)
(8.13)	$Nu = 1.86 \left(\frac{Re Pr D_h}{L} \right)^{0.33}$	Laminar flow (Khalifa et al. 2017)
(8.14)	$Nu = 0.036 Re^{0.8} Pr^{1/3}$	Turbulent flow (Andrjesdottir et al. 2013)
(8.15)	$Nu = 0.027 Re^{0.8} Pr^{0.4} \left(\frac{\mu_{b,hot}}{\mu_{membr,hot}} \right)^{0.14}$	Turbulent flow, hot channel (Qtaishat et al. 2008)
(8.16)	$Nu = 0.027 Re^{0.8} Pr^{0.33} \left(\frac{\mu_{b,cold}}{\mu_{membr,cold}} \right)^{0.14}$	Turbulent flow, cold channel (Qtaishat et al. 2008)
(8.17)	$Nu = 0.22 Re^{0.69} Pr_{bulk}^{0.13} \left(\frac{Pr_{bulk}}{Pr_{membr}} \right)^{0.25}$	Turbulent flow (Hitsov et al. 2017)

8.1.2. Mass Transfer

In DCMD, the water flux through the membrane pores is typically expressed through a linear dependence on the driving pressure difference:

$$(8.18) \quad J_w = B_m (P_{m,hot} - P_{m,cold})$$

where B_m is the mass transfer coefficient [$kg / (m^2 s Pa)$], while $P_{m,hot}$ and $P_{m,cold}$ are the vapor pressures at the temperatures $T_{m,hot}$ and $T_{m,cold}$ respectively, calculated using the Antoine equation (Qtaishat et al. 2008). $P_{m,hot}$ is obtained multiplying the vapor pressure at $T_{m,hot}$ by the water activity at the concentration of the solution at the bulk membrane interface $C_{m,hot}$. The calculation of B_m is a widely discussed topic in literature and it is based on the definition of the main transport mechanisms through

porous membranes, i.e. Knudsen diffusion, molecular diffusion or a combination of these two. The identification of the predominant mass transfer mechanism is possible through the calculation of the Knudsen coefficient, given by the ratio of the molecular mean free path within the pores and the pore diameter (λ/d_p). The definition of the molecular free path is reported in equation 8.19, where K_b is the Boltzmann constant, T and P_{pore} are the average temperature [K] and pressure [Pa] within the pores and d_{wat} is the collision diameter of water vapor molecules, assumed as hard spheres and equal to 2.64×10^{-10} m.

$$(8.19) \quad \lambda = \frac{K_b T}{\sqrt{2} \pi P_{\text{pore}} d_{\text{wat}}^2}$$

If the molecular mean free path is higher than the pore diameter ($Kn > 1$), the collisions between the molecules and the wall are dominant with respect to the collisions molecules-molecules, which means that the Knudsen diffusion is the most representative transport mechanism (Qtaishat et al. 2008). Conversely, if the pore diameter is higher than the molecular mean free path ($Kn < 0.01$) the predominant transport mechanism is the molecular diffusion. In most cases, the value of Kn is between 0.01 and 1, which means that the transport is given by the combination of the two mechanisms. The definition of the mass transfer coefficient will then take into account both transport terms, here represented by $D_{w,k}$ and $D_{w,m}$, i.e. the Knudsen diffusion coefficient and the molecular diffusion coefficient respectively (Andrjesdottir et al. 2013).

$$(8.20) \quad D_{w,k} = \frac{2 r_{\text{pore}} \varepsilon}{3 \tau} \sqrt{\frac{8 R T}{\pi M_{w,\text{wat}}}}$$

$$(8.21) \quad D_{w,m} = 4.46 E - 6 \frac{\varepsilon}{\tau} T^{2.334}$$

$$(8.22) \quad B_m = \frac{1}{R T} \frac{D_{w,k} D_{w,m}}{D_{w,m} + P_{\text{air}} D_{w,k}} \frac{M_{w,\text{wat}}}{\delta_m}$$

where r_{pore} is the pore radius, τ is the membrane tortuosity, R is the universal gas constant, T is the average temperature within the pore [K], $M_{w,\text{wat}}$ is the molecular weight of water [kg/mol] and P_{air} is the air pressure inside the pores, calculated as the difference between the pressure in the pores ($1.103E5$ Pa) and the vapor pressure at the average temperature (Khalifa et al. 2017).

Finally, as already mentioned, the concentration polarization effect is usually accounted for the calculation of the concentration at the bulk membrane interface:

$$(8.23) \quad C_{m,\text{hot}} = C_{\text{bulk,hot}} e^{\frac{J_w}{k_{f,\text{mass}} \rho}}$$

where $k_{f,\text{mass}}$ is the mass transfer coefficient in the feed channel, calculated as:

$$(8.24) \quad k_{f,\text{mass}} = \frac{\text{Sh} D_{\text{NaCl,wat}}}{D_h}$$

where $D_{\text{NaCl,wat}}$ is the diffusivity of NaCl in water and Sh is the Sherwood number which is calculated in analogy with Nu number (Hitsov et al. 2017), as function of Re and Schmidt number:

$$(8.25) \quad \text{Sc} = \frac{\mu}{\rho D_{\text{NaCl,wat}}}$$

$$(8.26) \quad \text{Sh} = 0.22 \text{Re}^{0.69} \text{Sc}_{\text{bulk}}^{0.13} \left(\frac{\text{Sc}_{\text{bulk}}}{\text{Sc}_{\text{membr}}} \right)^{0.25}$$

The equations describing the mass and heat transfer were implemented on Python and solved following an iterative resolution procedure, which updates the temperature and feed concentration values at the bulk-membrane interface, until the difference between the three heat fluxes ($Q_{\text{conv,hot}}$, Q_m and $Q_{\text{conv,cold}}$) is minimized.

8.2. DCMD Unit Model – Mass and Energy Balances

The model described in the previous paragraph concerning the mass and heat transport mechanisms across the membrane has been scaled up, in order to simulate the whole DCMD unit. The unit is supposed to work in a counter-current mode, as shown in Figure 12, which makes necessary the implementation of an iterative procedure. Therefore, the MD unit was divided into a certain number of elements (usually 10, in literature also 3 or 5 elements are used (Hitsov et al. 2017)) and for each element the model relevant to the calculation of heat and mass transfer across the channels and the membrane was applied. Then, the elements were interconnected via the application of mass and energy balances, to calculate the inlet flow rates, temperatures and feed composition for any element. These balances are reported in the equations (8.27-8.31).

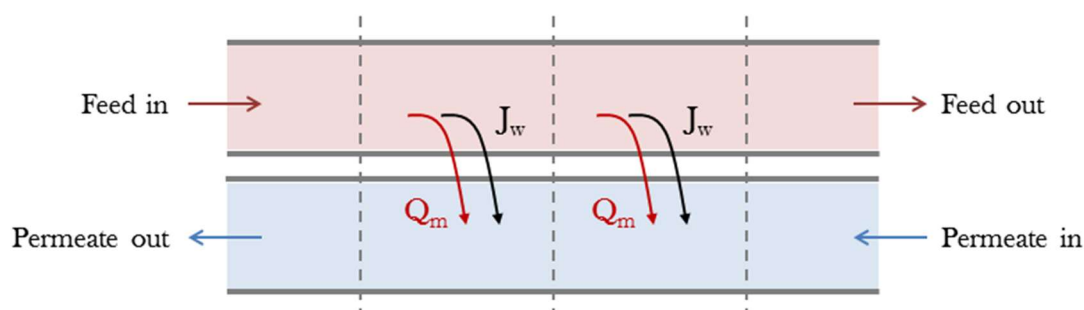


Figure 12: Schematic representation of a counter-current flat sheet DCMD unit.

$$(8.27) \quad m_{f,out} = m_{f,in} - J_w A_{elem} 10^{-3}$$

$$(8.28) \quad m_{p,in} = m_{p,out} - J_w A_{elem} 10^{-3}$$

$$(8.29) \quad T_{f,out} = \frac{m_{f,in} C_{p,f,in} \rho_{f,in} T_{f,in} - Q_m A_{elem}}{m_{f,out} C_{p,f,out} \rho_{f,out}}$$

$$(8.30) \quad T_{p,in} = \frac{m_{p,out} C_{p,p,out} \rho_{p,out} T_{p,out} - Q_m A_{elem}}{m_{f,in} C_{p,f,in} \rho_{f,in}}$$

$$(8.31) \quad C_{f,out} = \frac{m_{f,in} \rho_{f,in} C_{f,in}}{m_{f,out} \rho_{f,out}}$$

The calculation starts giving the input values, relevant to the unit geometry, the membrane properties, the feed composition, flow rate and pressure and the permeate flow rate. Then, guess values of the temperature profiles (T_{bulk} and T_m) in the feed and in the permeate channel, of the feed and permeate flow rate profiles and of the feed concentration profile along the unit have to be provided. At this point, the first iteration runs assuming these guess values and solving the membrane model for every element and the mass balances between the elements. All the profiles are recalculated and the inlet flow rate and temperature of the permeate solution, which enters in the last element, has to be compared with the input values. Thus, the iteration is repeated until the error between the calculated and the input permeate flow rate and the error between the calculated and the input permeate temperature is minimized. The minimization is performed through the minimize routine, in the `scipy.optimize` library, using the Nelder-Mead method and varying the outlet temperature and flow rate of the permeate solution.

8.3. DCMD Plant Model

The single DCMD unit is characterized by a low recovery, given by the ratio between the produced water flow rate and the feed flow rate. Therefore, thermodynamically, it cannot exceed 10% with the single pass (Ali et al. 2005). For this reason, in order to increase the recovery and to reach a higher concentration in the outlet feed solution, it is necessary to consider more MD units in series with intermediate coolers and heaters. For the simulation of the DCMD plant, Aquastill commercial modules were considered, which are given by 6 hot channels and 6 cold channels, in a spiral-wound fashion, with a total membrane area of 7.2 m² (Hitsov et al. 2017). The typical flow rate of these modules is comprised between 500 and 1500 l/h. The overall plant presents a certain number of branches in parallel ($N_{parallel}$), each of those crossed by a fixed permeate and feed flow rate equal to 1500 l/h ($M_{perm,in-design-lh}$ and $M_{feed,in-design-lh}$). The number of branches in parallel depends on the overall feed flow rate which has to be processed (or the amount of distillate which has to be produced) and the feed and permeate flow rate is defined through suitable pumps. Finally, each branch presents a certain number of modules in series, which depends on the water flux produced by each module. A schematic

representation of the MD plant presenting two parallel branches and N MD modules in series is reported in Figure 13.

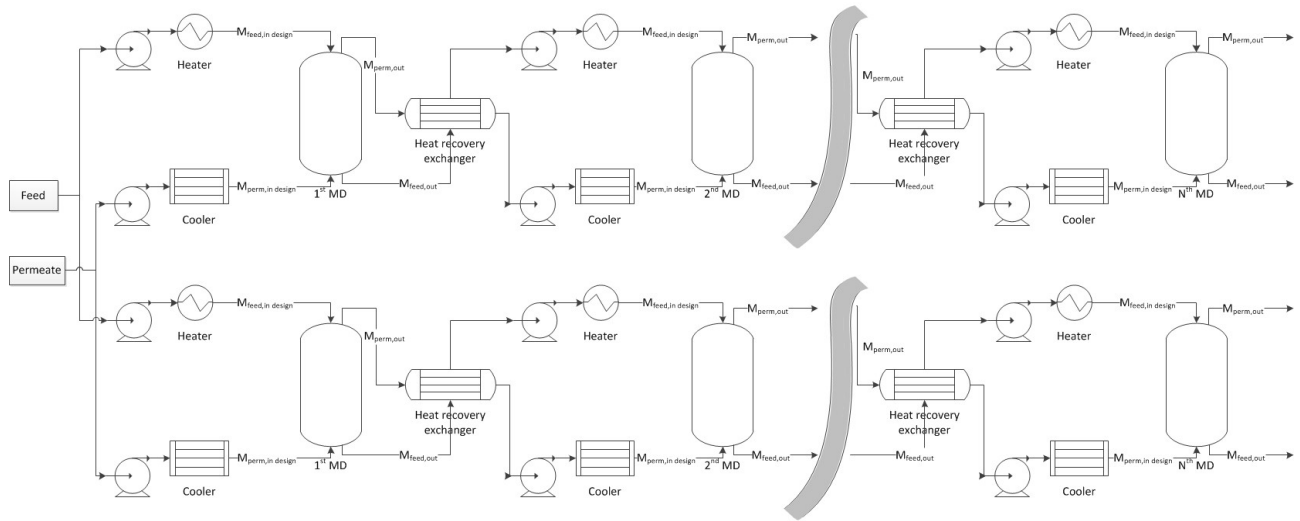


Figure 13: Schematic representation of the MD plant for large scale application.

Since every module works at the same conditions in terms of inlet temperature and flow rate, thanks to the employment of heat exchangers and pumps, the only difference between the modules concerns the inlet feed concentration, which is increasing from one module to the following. For this reason, the calculation of the required number of modules in series is performed considering the water flux produced in the MD module at the average concentration between the feed inlet and the required outlet concentrations. The overall plant mass balances and the calculation of the required number of modules are reported in equations (8.31-8.34).

$$(8.32) \quad M_{\text{brine,plant}} = \frac{M_{\text{feed,plant}} C_{\text{feed}}}{C_{\text{brine,plant}}}$$

$$(8.33) \quad M_{\text{dist,plant}} = M_{\text{feed,plant}} - M_{\text{brine,plant}}$$

$$(8.34) \quad N_{\text{parallel}} = \text{int} \left(\frac{M_{\text{feed,plant}} \rho_{\text{feed,plant}}}{M_{\text{feed,in-design-lh}} \times 1000} \right)$$

$$(8.35) \quad N_{\text{tot,modules}} = \text{int} \left(\frac{M_{\text{dist,plant}}}{J_{w,\text{aver}} A_{\text{module}} 3600} \right)$$

Where $M_{\text{feed,plant}}$ is the total feed flow rate to be processed in [kg/h]; $M_{\text{brine,plant}}$ and $M_{\text{dist,plant}}$ are the concentrate and distillate flow rates, respectively, which have to be produced in the plant [kg/h]; $C_{\text{brine,plant}}$ is the required outlet concentration of the concentrate solution [ppm] and $J_{w,\text{aver}}$ is the average water flux in [kg/(m² s)], calculated at the average concentration between C_{feed} and $C_{\text{brine,plant}}$.

Finally, the electric and thermal energy requirements are estimated according to equations (8.36-8.40). Regarding the thermal energy requirement, firstly, the thermal energy required to heat the total feed flow rate up to the inlet hot temperature is calculated. Then, between each module and the following in the series, a heat exchanger for heat recovery from the permeate to the concentrate flow rate is accounted, with a minimum temperature difference of 10°C. The remaining heating and cooling requirements are calculated separately.

$$(8.36) \quad P_{\text{electric,pumps}} = \frac{2 N_{\text{tot,modules}} M_{\text{feed,in-design-lh}} \Delta P_{\text{in}}}{\eta_{\text{pump}} \times 1000 \times 3600}$$

$$(8.37) \quad P_{\text{thermal,feed}} = \frac{M_{\text{feed,plant}}}{3600} C_{p,\text{feed}} (T_{\text{feed,in}} - T_{\text{intake}})$$

$$(8.38) \quad P_{\text{thermal,heater}} = \frac{M_{\text{feed,in-design-lh}}}{1000 \times 3600} \rho_{\text{feed,plant}} C_{p,\text{feed}} (T_{\text{feed,in}} - T_{\text{HR,feed,out}})$$

$$(8.39) \quad P_{\text{thermal,cooler}} = \frac{M_{\text{perm,in-design-lh}}}{1000 \times 3600} \rho_{\text{water}} C_{p,\text{water}} (T_{\text{HR,perm,out}} - T_{\text{perm,in}})$$

$$(8.40) \quad P_{\text{thermal,HR}} = \frac{M_{\text{feed,in-design-lh}}}{1000 \times 3600} \rho_{\text{feed,plant}} C_{p,\text{feed}} (T_{\text{HR,feed,out}} - T_{\text{HR,feed,in}}) \\ = \frac{M_{\text{perm,in-design-lh}}}{1000 \times 3600} \rho_{\text{water}} C_{p,\text{water}} (T_{\text{HR,perm,in}} - T_{\text{HR,perm,out}})$$

where $P_{\text{electric,pumps}}$ is the electric consumption of the pumps in [W], $P_{\text{thermal,feed}}$, $P_{\text{thermal,heater}}$, $P_{\text{thermal,cooler}}$ and $P_{\text{thermal,HR}}$ are the thermal consumption of the heat exchanger to heat the feed from T_{intake} (taken equal to 20°C) and $T_{\text{feed,in}}$ and the ones of each intermediate heater, cooler and recovery heat exchanger between MD modules [W]. $C_{p,\text{feed}}$ and $C_{p,\text{water}}$ are the specific heat of feed and water respectively in [kJ/(kg K)]. $T_{\text{HR,feed,in}}$, $T_{\text{HR,feed,out}}$, $T_{\text{HR,perm,in}}$ and $T_{\text{HR,perm,out}}$ are the inlet and the outlet temperatures of the feed and the permeate solutions in the recovery heat exchanger. Finally, ΔP_{in} is the inlet feed and permeate pressures [Pa], usually equal to 1.013E5 Pa.

8.4. MD Nomenclature

T	temperature [K]
m	volume flow rate [m ³ /s]
M	mass flow rate [kg/h]
C	concentration [ppm]
Q	heat flux [W/m ²]
h	heat transfer coefficient [W/(m ² K)]
Jw	water flux [kg/(m ² s)]
ΔH_{evap}	latent heat of vaporization of water [J/kg]
k_m	membrane thermal conductivity [W/(m K)]
k_{air}	air thermal conductivity [W/(m K)]
$k_{\text{membr,pol}}$	polymeric structure thermal conductivity [W/(m K)]
k	thermal conductivity of the solution [W/(m K)]
Nu	Nusselt number [-]

Re	Reynolds number [-]
Pr	Prandtl number [-]
Sh	Sherwood number [-]
Sc	Schmidt number [-]
D_h	hydraulic diameter of the channel [m]
v	fluid velocity in the channel [m/s]
C_p	fluid specific heat [J/(kg K)]
L	channel length [m]
B_m	mass transfer coefficient [kg / (m ² s Pa)]
ΔP_{in}	inlet pressure [Pa]
R	ideal gas constant (8.314 J/(K mol))
k_B	Boltzmann constant (1.38066 x 10 ⁻²³ J/K)
d_{wat}	collision diameter of water vapor [m]
P_{pore}	pressure within the pores [Pa]
r_{pore}	pore radius [m]
P_{air}	air pressure inside the pores [Pa]
$D_{w,k}$	Knudsen diffusion coefficient [m ² /s]
$D_{w,m}$	molecular diffusion coefficient [m ² /s]
$D_{NaCl,wat}$	diffusivity of NaCl in water [m ² /s]
$k_{f, mass}$	mass transfer coefficient in the feed channel [m/s]
$N_{parallel}$	number of branches in parallel [-]
$N_{tot, modules}$	total number of modules present in the plant [-]
A_{module}	membrane area of a single module [m ²]
$P_{electric, pumps}$	electric consumption of the pumps [W]
$P_{thermal, feed}$	thermal consumption of the heat exchanger to heat the feed cooler [W]
$P_{thermal, heater}$	thermal consumption of the intermediate heater [W]
$P_{thermal, cooler}$	thermal consumption of the intermediate cooler [W]
$P_{thermal, HR}$	thermal consumption of the intermediate recovery heat exchanger [W]
Subscripts	
m	membrane
f	feed
p	permeate
m,hot	feed membrane interface
m,cold	permeate membrane interface
bulk,hot	feed bulk
bulk,cold	permeate bulk
conv,hot	convective flux, feed side
conv,cold	convective flux, permeate side
cond,m	conductive flux, membrane
evap,m	latent heat, membrane
in	inlet in the element
out	outlet of the element
feed,plant	solution fed to the plant
brine,plant	concentrate solution produced by the plant
dist,plant	distillate solution produced by the plant
perm,in-design-lh	design inlet permeate of the module (flow rate in [l/h])
feed,in-design-lh	design inlet feed of the module (flow rate in [l/h])

Greek letters

δ_m	membrane thickness [m]
ε	membrane porosity [-]
ρ	solution density [kg/m^3]
μ	dynamic viscosity of the fluid [$\text{kg}/(\text{m s})$]
λ	molecular mean free path [m]
τ	membrane tortuosity [-]

Acronyms

MD	Membrane distillation
DCMD	Direct contact membrane distillation
AGMD	Air gap membrane distillation
SGMD	Sweep gas membrane distillation
VMD	Vacuum membrane distillation

9. Ion Exchange Resins Model

Ion Exchange resins (IEX) provide the interchange of ions between two phases, i.e. a resin phase and a liquid phase. The resin is a cross-linked polymer network, which presents a relatively uniform distribution of active sites, consisting in functional groups and ions, electrostatically bound (Alexandratos 2009). When the resin is surrounded by a solution containing ions of the same charge, an ion exchange occurs: the ions before dissolved in the solution get bound to the resin, while the ions before bound to the resin move to the liquid phase, as it is reported in Figure 14. The main advantage of the ion exchange resins technology consists in the reversibility of the ion exchange: there is no permanent change in the structure of the resin and it is possible to reuse the ion exchange material after having regenerated it (Wheaton and Lefevre 2016). Therefore, the technology provides the alternation of two phases: a loading phase, where the ions present in the feed solution are entrapped by the resin, and a regeneration phase, where a regenerant solution is employed to bring the resin back to the initial condition. In particular, during the regeneration phase, the ions that were entrapped in the resin sites are substituted with corresponding ions, present in the regenerant solution and initially bound to the resin active sites (e.g. Na^+ in the case of Figure 14).

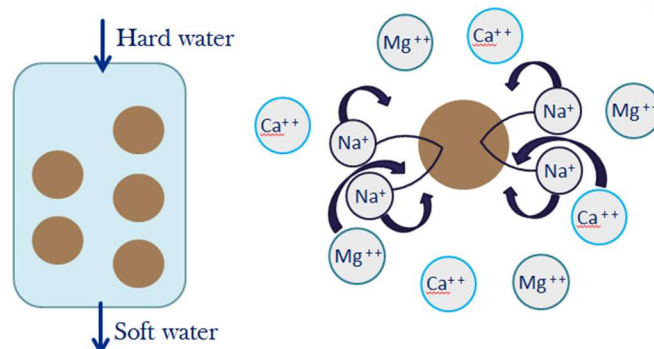
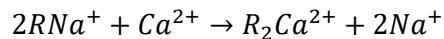


Figure 14: Schematic representation of the loading phase for IEX resins used for water softening.

For example, in water softening, the reaction occurring in the loading phase is:



while the inverse reaction occurs during the regeneration phase. In the direct reaction, the exchanger R can exchange the bound ion Na^+ for the Ca^{2+} ions present in the hard water, so the calcium is removed from the water and the equivalent quantity of sodium is released to the solution. When all the active sites are occupied by Ca^{2+} or Mg^{2+} ions, the resin has to be regenerated through the employment of a regenerant solution of NaCl, in order to bring the sites back to the Na^+ form and the resin can be reused (Alexandratos 2009).

The IEX resins are employed for several applications, for example for softening/dealkalization, organic scavenging, demineralization, nitrate or boron removal and accordingly several different types are available in the industry. The resins are typically categorized into cation and anion exchange resins and within both categories a further sub-categorisation into strong and weak resins is performed in literature (Wheaton and Lefevre 2016). Within the cation exchange resins, the weak resins have a high affinity with hydrogen ions and are typically regenerated via the employment of strong acids, conversely the strong resins are able to exchange cations and to split neutral salts and are typically regenerated via a NaCl solution. Regarding the anion exchange resins, the weak resins are used for the sorption of strong acids and are regenerated via caustic soda, while the strong resins have greater affinity for weak acids, as the ones commonly present in the water to be demineralized. In the following, the model of IEX resins employed for water softening with co-current regeneration is described. The model structure then can be readapted, when necessary, to other applications, modifying the input feed composition, the resin properties and the regenerant solution.

9.1. Model for IEX Resins for Water Softening

The model follows the structure of the commercial software WAVE for IEX design and it is able to calculate the main outputs relevant to both the loading and the regenerant phase, e.g. the required resin volume, the feed velocity in crossing the resin bed, the required regeneration time and volume. All the inputs and outputs of the model are listed in Table 12.

Table 12: Inputs and Outputs of the IEX model.

Inputs	Outputs
Feed flow rate [m ³ /h]	Resin volume [m ³]
Feed composition [ppm]	Ionic load [eq]
Feed hardness [eq/L]	Linear [m/h] and specific [BV/h] feed velocity
Train configuration	Resin area [m ²] and bed depth [m]

Duration of the operating cycle [h]	Regeneration ratio [%]
Resin and regeneration type	Applied and excess regenerant per cycle [eq]
Regenerant concentration [%wt]	Gross and net throughput [m ³]
Regeneration temperature [°C]	Total regeneration volume [m ³]
Regeneration dose [g/L _{resin}]	Total regeneration time [h]
Regeneration condition (backwash duration and expansion, injection velocity, rinse volume)	Duration and volume of the regeneration phases (backwash, injection, displacement and fast rinse)
Max pressure drop in the resin bed [bar]	IEX recovery [%]
Max hardness in the effluent [ppm CaCO ₃]	Hardness leakage [ppm CaCO ₃]

The model presents an iterative procedure, where the value of the required resin volume calculated in the previous iteration is given as the starting value for the calculation of the other variables in the following iteration. The iterative procedure stops as soon as the difference between the guess and the calculated volume is lower than a certain tolerance (i.e. 1e-4). The procedure starts with the feed and the resin characterization. For what concerns the feed, the concentration of every ion is converted into [eq/L] and the TDS of the feed is estimated in [eq/L] and in [ppm CaCO₃]. For what concerns the resin characterization, once a resin type is defined, the operating capacity can be calculated, on the basis of the information reported in the resin data sheet (*DOWEX Marathon C Resin - Product Data Sheet* n.d.). For example, for Dowex Marathon C resin in the Na form, the operating capacity can be calculated as function of the regeneration dose, according to Figure 15. For the effective operating capacity, a safety factor is used and its value is taken equal to 0.95, as in the Wave software.

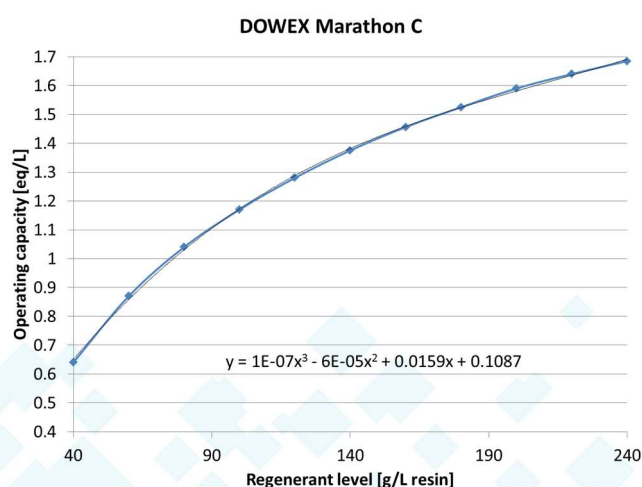


Figure 15: Operating capacity of DOWEX Marathon C resins for water softening.

At this point, the solving procedure starts with a guess resin volume V_{resin} and cross section area A_{resin} . The feed flow rate (Q_{feed} [m³/h]) to be considered in the procedure depends on the train configuration, since, often, two or more trains online and one train for the regeneration are accounted. Thus, the total feed flow rate has to be divided by the number of trains online. Moreover, the feed water is also used for one of the regeneration stages, the fast rinse, which is the final part of the regeneration, used to flush out the excess regenerant (*DOWEX Ion Exchange Resins Water Conditioning Manual* n.d.). For this reason, the net feed water processed in a cycle depends on the total feed water fed to the train and on the amount required by the fast rinse. Consequently, the gross throughput, defined as the total amount of water which is processed during the service cycle in m³, is calculated as follows:

$$(9.1) \quad \text{throughput}_{\text{gross}} = Q_{\text{feed}} t_{\text{cycle}} - V_{\text{fast rinse}}$$

where t_{cycle} is the duration of the operating cycle in hours and $V_{\text{fast rinse}}$ is the total volume required by the last regeneration stage in m³. Thus, the net feed water flow rate ($Q_{\text{feed,net}}$) is given by the ratio between the $\text{throughput}_{\text{gross}}$ and t_{cycle} . At this point, the feed linear velocity in m/h and the feed specific velocity in BV/h (bed volumes per hour) can be calculated as $Q_{\text{feed,net}} / A_{\text{resin}}$ and $Q_{\text{feed,net}} / V_{\text{resin}}$ respectively. The ionic load is defined as the total amount of equivalents that can be exchanged by the resin bed, thus it can be calculated as:

$$(9.2) \quad \text{Ionic load} = C_{\text{eff,op}} V_{\text{resin}} 1000$$

where $C_{\text{eff,op}}$ is the effective operating capacity in [eq/L].

The net throughput is defined as the amount of water produced in the operating cycle and it takes into account the fact that part of the water produced is used for the other regeneration stages, i.e. the backwash, injection and displacement (or slow) rinse.

$$(9.3) \quad \text{throughput}_{\text{net}} = \text{throughput}_{\text{gross}} - V_{\text{backwash}} - V_{\text{injection}} - V_{\text{displ rinse}}$$

In analogy with the net feed water flow rate, the net product flow rate ($Q_{\text{prod,net}}$) is calculated as the ratio between $\text{throughput}_{\text{net}}$ and t_{cycle} . Finally, the IEX recovery is defined as the ratio between the $\text{throughput}_{\text{net}}$ and the total amount of water supplied during the operating cycle per train. For the first guess, $Q_{\text{feed,net}}$ and $Q_{\text{prod,net}}$ are assumed to be equal to Q_{feed} , so the IEX recovery is assumed to be 100%.

For what concerns the regeneration phase, the regeneration dose R_{dose} , i.e. the amount of regenerant used per cycle in [g/L_{resin}], is given as an input, together with the concentration of the regenerant solution R_{conc} . From the regeneration dose, it is possible to define the regeneration ratio R_{ratio} , i.e. the reciprocal of the regeneration efficiency, being it defined as the ratio between the total applied regenerant and the ionic load.

$$(9.4) \quad R_{\text{ratio}} = \frac{R_{\text{dose}}/MW_{\text{NaCl}} V_{\text{resin}} 1000}{C_{\text{eff,op}} V_{\text{resin}} 1000} \times 100$$

$$(9.5) \quad \text{Applied regenerant} = \frac{R_{\text{dose}}}{MW_{\text{NaCl}}} V_{\text{resin}} 1000$$

$$(9.6) \quad \text{Excess regenerant} = \text{Applied regenerant} - \text{Ionic load}$$

Moreover, the duration of the regeneration cycle can be evaluated by investigated all the single regeneration phases. The backwashing is performed before the injection of the regenerant solution and it consists of an upward flow to remove all the materials covering the resin. The duration is usually fixed (e.g. 15 min) together with the bed expansion occurring during the backwashing. If the bed expansion is given, a linear correlation between expansion and water flow rate, usually supplied by the resin manufacturer in the data sheet, is applied to calculate the water flow rate (*DOWEX Ion Exchange Resins Water Conditioning Manual* n.d.). Regarding the injection phase, the flow rate is usually given as a parameter (e.g. specific flow rate equal to 3.5 BV/h). The required injection time is calculated taking into account the total amount of regenerant that has to be supplied (applied regenerant [eq]) and the concentration of the solution, according to the following expression:

$$(9.7) \quad t_{\text{injection}} = \frac{\text{Applied regenerant}}{\frac{R_{\text{conc}}}{MW_{\text{NaCl}}} Q_{\text{injection}}}$$

where R_{conc} is the concentration of the regenerant solution [ppm] and $Q_{\text{injection}}$ is the injection flow rate in m^3/h . Finally, the last stages of the regeneration cycle provide a rinse, i.e. the passage of water through the resin bed to flush out the remaining regenerant solution. Just after the injection, a displacement (slow) rinse is performed with the treated water and usually with the same flow rate as the regenerant in the injection phase. The total volume of water is usually given (e.g. 2 BV) and then the required time can be calculated. The second rinse step is faster and it usually operates at the same flow rate of the feed ($Q_{\text{feed,net}}$) and, also in this case, the volume is given as input (e.g. 3 BV) and the time is calculated.

Overall, the regeneration time ($t_{\text{regeneration}}$) is given by the sum of the backwash (t_{backwash}), injection ($t_{\text{injection}}$), displacement rinse ($t_{\text{displ rinse}}$) and fast rinse time ($t_{\text{fast rinse}}$) and the total regeneration volume ($V_{\text{regeneration}}$) is given by the sum of the volumes required by each of these stages. Once these volumes are calculated, they will be used as the guess values in the following iteration for the calculation of $\text{throughput}_{\text{gross}}$, $\text{throughput}_{\text{net}}$, $Q_{\text{feed,net}}$ and $Q_{\text{prod,net}}$.

At this point, the resin volume V_{resin} is recalculated according to the expression:

$$(9.8) \quad V_{\text{resin}} = \frac{\text{throughput}_{\text{gross}} \text{hardness}_{\text{in}}}{C_{\text{eff,op}} 1000}$$

where $\text{hardness}_{\text{in}}$ is the inlet amount of Mg^{++} and Ca^{++} in meq/L . The resin cross-section area and the bed depth are calculated by imposing a maximum pressure drop across the resin bed. Therefore, the

resin data sheet provides the trend of the pressure drop in [bar/m] vs. the flow rate, as shown for the DOWEX Marathon C resins in Figure 16 (*DOWEX Marathon C Resin - Product Data Sheet* n.d.). The shown pressure drops are measured at $T = 20^{\circ}\text{C}$. In order to calculate the pressure drops at a different temperature T [$^{\circ}\text{C}$], the following correlation is proposed for these specific resins:

$$(9.9) \quad P_T = \frac{P_{20^{\circ}\text{C}}}{0.026 T + 0.48}$$

Employing the pressure drop trend with the feed velocity (Figure 16) and the correction with the temperature (usually the temperature used for the estimation of pressure drops is 0°C), it is possible to calculate the cross section area and the height of the resin bed in correspondence to a total pressure drop of 1 bar.

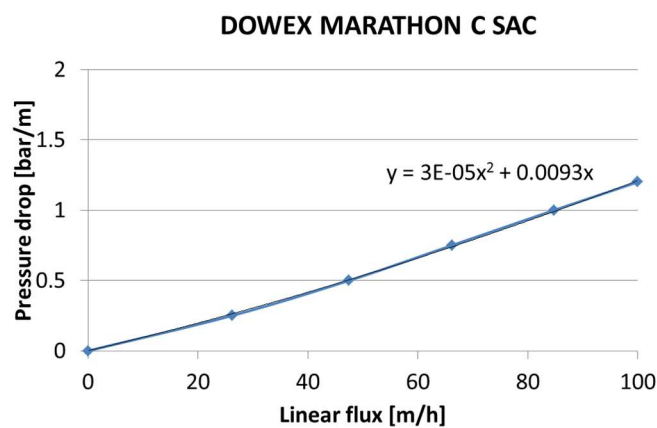


Figure 16: Trend of the pressure drop [bar/m] with the linear flux [m/h] for the DOWEX Marathon C Strong Acid Cation resins.

The values of resin volume, area and bed depth are then updated in the following iteration and all the calculations are repeated, until the whole system results to be solved.

Finally, it is possible to calculate the system leakage, which corresponds to the hardness still present in the treated water. The leakage [ppm CaCO_3] is function of the feed TDS in ppm CaCO_3 according to a linear correlation of the generic form:

$$(9.10) \quad \text{leakage} = A TDS_{\text{feed}} - B$$

where A and B depend on the regeneration dose. Different linear trends of leakage vs. TDS_{feed} were reported in the resin data sheet at different regeneration dose, for this reason more general correlations for A and B in function of the regeneration dose were derived, as shown in Figure 17. If the leakage is higher than the maximum value given as input, the regeneration dose should be increased and the calculation performed again.

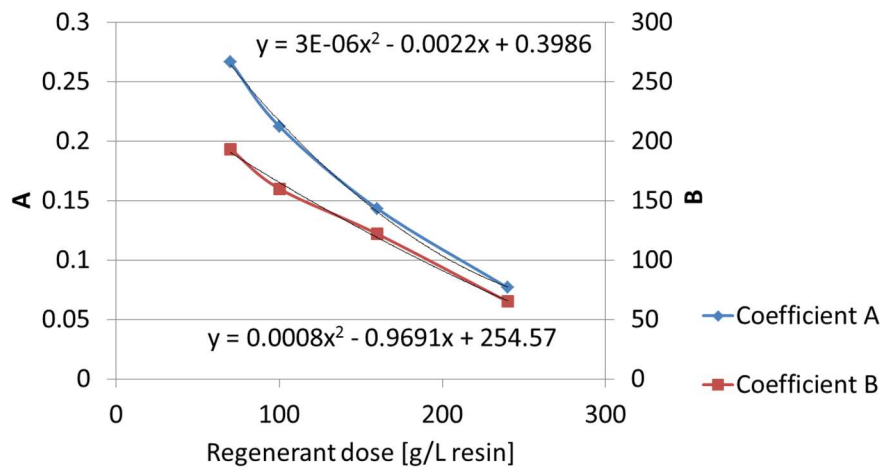


Figure 17: Trends of the coefficients A and B of Equation 9.10 as function of the regenerant dose.

9.2. IEX Nomenclature

V_{resin}	required volume of the resins [m ³]
A_{resin}	section of the resins [m ²]
Q_{feed}	feed flow rate [m ³ /h]
t_{cycle}	duration of the operating cycle[h]
MW_{NaCl}	molecular weight of NaCl [mol/g]
$V_{backwash}$	total regenerant volume required by the backwash stage during regeneration [m ³]
$V_{injection}$	total regenerant volume required by the injection stage during regeneration [m ³]
$V_{displ\ rinse}$	total regenerant volume required by the displacement rinse during regeneration [m ³]
$V_{fast\ rinse}$	total regenerant volume required by the fast rinse during regeneration [m ³]
$V_{regeneration}$	total regenerant volume required [m ³]
$t_{backwash}$	backwash time during regeneration [h]
$t_{injection}$	injection time during regeneration [h]
$t_{displ\ rinse}$	displacement rinse time during regeneration [h]
$t_{fast\ rinse}$	fast rinse time during regeneration [h]
$t_{regeneration}$	regeneration time [h]
$Q_{feed,net}$	net feed flow rate [m ³ /h]
$C_{eff,op}$	effective operating capacity [eq/L]
$Q_{prod,net}$	net product flow rate [m ³ /h]
R_{dose}	regeneration dose [g/L _{resin}]
R_{ratio}	regeneration ratio [%]
R_{conc}	concentration of the regenerant solution [ppm]
T	operating temperature [°C]
P_T	pressure drop at T [bar/m]
TDS_{feed}	concentration of the feed [ppm CaCO ₃]
A	constant for the calculation of the leakage
B	constant for the calculation of the leakage
hardness _i	inlet amount of Mg ⁺⁺ and Ca ⁺⁺ [meq/L]

Acronyms

IEX Ion Exchange

10. Eutectic Freeze Crystallization Model

10.1. Data driven numerical Model

Based on data from Hassan et al. (Hassan et al, 2017), a statistic approach of EFC modelling has been developed. This model only allows interpolation (not extrapolation) since it uses Dealunay patterns. When the requested information is out of a defined parameter range it issues an error. Therefore, the minimum and maximum values for which the modelling is valid are determined by the literature values of Hassan et al. The model consists of 3 files:

- a) *efcStatSingle.m*: calculation of a given scaling induction time value. The file must edit the values of N and DT, which are the rotation speed in rpm and the difference of sub-cooling temperatures in C, respectively. There are comments on the file indicating it. The file returns the induction time in seconds.
- b) *efcStatSweepPlot.m*: allows to sweep through different temperature differentials at a specific rotation speed. DT0 is the value of the temperature difference from which the sweep begins, and it is the number of increments (tenths of a degree). The file returns a graph of induction time vs. temperature differential for a specific rotation speed.
- c) *efcStatSweepFile.m*: does the same as the previous one but instead of a graph the output is a data file in two columns (temperature-time difference).

10.2. Thermodynamic EFC Model

Eutectic freezing crystallization operates at the eutectic temperature/point of a binary solution. In this method, salts separate as solids and fresh water separates as ice from brine simultaneously. Both salt and ice nucleates grow independently. This gives the advantage of easy separation since ice floats and the salt sinks by density difference. Though, very low operating temperature (-20 to -25 °C) and thus additional cost of eutectic freezing is required compared to other freezing methods. Separation and melting are the final steps. For separation, the formed ice blocks are collected in the ice crystal separator where they are washed with pure fresh water to purify blocks' surfaces and recover the solutes involved. The main disadvantage of the freeze crystallization process compared with evaporation and RO are the incurred operational costs during the ice separation process (Kucera 2014). Melting of pure ice blocks finally takes place either by direct or indirect contact. However, energy recovery is one of the important aspects of this process that must be highly considered.

Besides the statistical model, a first thermodynamic version of the model is an attempt to obtain a mathematical expression for the ice scaling thickness and its purity as a function of the variables of interest: time, temperature, concentration and rotational speed. The current version of the model does not take rotation into account, as the first experimental tests will be run in a static medium. The effect of the rotational speed can be implemented in the model in a revised version.

Once the ice scaling thickness is determined, the overall heat transfer can be evaluated. The model is formulated under the following hypotheses:

- Eutectic freeze crystallization: both ice and salt crystallize simultaneously and grow at the same rate.
- Perfect mixing: temperature and concentration are uniform everywhere within the vessel.
- There are no heat losses in the whole system.
- The thickness of the ice scaling is much smaller than the vessel radius.
- Crystals are considered to be spherical in shape.
- The temperature at the inner side of the ice scaling is equal to the slurry temperature.

The nucleation rate, in number of crystals formed by volume and time units, can be expressed as:

$$(10.1) \quad B = b_1 \exp\left(\frac{-b_2}{T}\right)$$

where b_1 and b_2 are constants to be determined and T is the temperature. The effective nucleation rate, in number of crystals by time unit, is:

$$(10.2) \quad B_{eff} = B(1 - \Phi)V$$

where Φ is the volume fraction of crystals, both ice and salt, inside the vessel, and V the total volume of the vessel without internal elements.

The growth rate of the crystals, even if there are different opinions among authors and there seems not to be a clear established criterion, can be approximated as:

$$(10.3) \quad G = g_1 \exp\left(\frac{-g_2}{T}\right)(C - C_{eq})$$

where g_1 and g_2 are constants to be determined, C is the concentration of the substance crystallizing in the solution and C_{eq} the equilibrium concentration. The total volume of crystals in each time step is:

$$(10.4) \quad v_{cT}^i = \sum N_c^i v_c^j$$

where N_c is the number of crystals formed at time step i and v_c the volume of crystal formed at time step j . Subscripts i and j vary to take into account that the first crystals formed will be the largest ones. The number of crystals formed at each time step is:

$$(10.5) \quad N_c^i = B_{eff}^i \Delta t$$

where Δt is the time step, which is considered uniform.

The crystal volume is determined by:

$$(10.6) \quad v_c = \frac{4}{3}\pi(r^{i-1} + G^i \Delta t)^3$$

Where r is the radius of the crystal. The volume fraction of crystals inside the vessel is, then:

$$(10.7) \quad \phi = \frac{v_{cT}}{V}$$

Since the interest lies in obtaining a correlation from experimental data via coefficient adjustment, we can assume, recalling Eq. 10.5, that the total number of crystals formed is

$$(10.8) \quad N_c \sim B_{eff}t = B(1 - \phi)Vt$$

Therefore, the following equation can be used to calculate the number of crystals:

$$(10.9) \quad N_c = b_1 \exp\left(\frac{-b_2}{T}\right) (1 - \phi)Vt$$

Combining the expressions for the crystal volume (10.6) and growth rate (10.3) presented earlier, the crystal volume can be obtained as:

$$(10.10) \quad v_c = \frac{4}{3}\pi \left(r_0 + g_1 \exp\left(\frac{-g_2}{T}\right) (C - C_{eq})t \right)^3$$

So, the total volume of crystals can be approximated as:

$$(10.11) \quad v_{cT} = b_1 \exp\left(\frac{-b_2}{T}\right) (1 - \phi)Vt \frac{4}{3}\pi \left(r_0 + g_1 \exp\left(\frac{-g_2}{T}\right) (C - C_{eq})t \right)^3$$

Since the total volume of crystals is related to the total volume of the vessel by the crystal volume fraction (Eq. 10.7), then

$$(10.12) \quad \phi V = b_1 \exp\left(\frac{-b_2}{T}\right) (1 - \phi)Vt \frac{4}{3}\pi \left(r_0 + g_1 \exp\left(\frac{-g_2}{T}\right) (C - C_{eq})t \right)^3$$

This model can be simplified by neglecting the initial radius of the crystal ($r_0=0$), which seems reasonable specially at long times. In order to facilitate reading, some constant parameters can be grouped:

$$(10.13) \quad \alpha_1 = b_1 \frac{4}{3}\pi g_1^3$$

So, the volume fraction of crystals can be calculated as:

$$(10.14) \quad \phi = \alpha_1(1 - \phi) \exp\left(\frac{-b_2}{T}\right) \left(\exp\left(\frac{-g_2}{T}\right)\right)^3 (C - C_{eq})^3 t^4$$

After some mathematical manipulation, the following expression for the crystal volume fraction can be obtained:

$$(10.15) \quad \phi = \alpha_1(1 - \phi)(-C_{eq})^3 t^4 \exp\left(\frac{-b_2 - 3g_2}{T}\right)$$

Regrouping some more parameters:

$$(10.16) \quad \alpha_2 = -b_2 - 3g_2$$

and then

$$(10.17) \quad \phi = \alpha_1(1 - \phi)(C - C_{eq})^3 t^4 \exp\left(\frac{\alpha_2}{T}\right)$$

After some more mathematical manipulation:

$$(10.18) \quad \phi = \frac{\alpha_1(C - C_{eq})^3 t^4 \exp\left(\frac{\alpha_2}{T}\right)}{1 + \alpha_1(C - C_{eq})^3 t^4 \exp\left(\frac{\alpha_2}{T}\right)}$$

$$(10.19) \quad \frac{1}{\phi} = \frac{1}{\alpha_1(C - C_{eq})^3 t^4 \exp\left(\frac{\alpha_2}{T}\right)} + 1$$

A volume fraction of scaling is defined as ϕ_s , with the volume of scaling being

$$(10.20) \quad V_s = \phi_s V$$

This volume of scaling can be also expressed in terms of the vessel geometry:

$$(10.21) \quad V_s = \pi R_i^2 L - \pi(R_i - \gamma)^2 L$$

where γ is the scaling thickness. Considering the scaling thickness much smaller than the vessel radius, then after some mathematical manipulation the volume of scaling can be defined as

$$(10.22) \quad V_s \approx 2\pi R_i \gamma L$$

Another parameter which will be useful is now defined:

$$(10.23) \quad \alpha_3 = \frac{V_s}{v_{cT}}$$

Substituting into the previously derived equation for the crystal volume fraction (10.19):

$$(10.24) \quad \frac{V}{v_{cT}} = \frac{1}{\alpha_1(C - C_{eq})^3 t^4 \exp\left(\frac{\alpha_2}{T}\right)} + 1$$

$$(10.25) \quad \frac{\alpha_3 V}{V_s} = \frac{1}{\alpha_1(C - C_{eq})^3 t^4 \exp\left(\frac{\alpha_2}{T}\right)} + 1$$

Introducing the expression for the volume of scaling (10.22):

$$(10.26) \quad \frac{\alpha_3 V}{2\pi R_i \gamma L} = \frac{1}{\alpha_1(C - C_{eq})^3 t^4 \exp\left(\frac{\alpha_2}{T}\right)} + 1$$

and after some more mathematical manipulation:

$$(10.27) \quad \gamma = \frac{\alpha_3 V \alpha_1 (C - C_{eq})^3 t^4 \exp\left(\frac{\alpha_2}{T}\right)}{2\pi R_i L \left(\alpha_1 (C - C_{eq})^3 t^4 \exp\left(\frac{\alpha_2}{T}\right) + 1 \right)}$$

Another parameter grouping variable is defined for the sake of clarity:

$$(10.28) \quad \alpha_4 = \frac{2\pi R_i L}{V}$$

Substituting, manipulating and rearranging an expression for the scaling thickness is obtained:

$$(10.29) \quad \gamma = \frac{\alpha_1 \alpha_3 (C - C_{eq})^3 t^4 \exp\left(\frac{\alpha_2}{T}\right)}{\alpha_4 \left(\alpha_1 (C - C_{eq})^3 t^4 \exp\left(\frac{\alpha_2}{T}\right) + 1 \right)}$$

Since α_4 is a geometrical parameter, the previous expression becomes

$$(10.30) \quad \gamma = \frac{V}{2\pi R_i L} \frac{\alpha_1 \alpha_3 (C - C_{eq})^3 t^4 \exp\left(\frac{\alpha_2}{T}\right)}{\left(\alpha_1 (C - C_{eq})^3 t^4 \exp\left(\frac{\alpha_2}{T}\right) + 1 \right)}$$

where α_1 , α_2 and α_3 are parameters to be determined experimentally.

As for the purity of the crystals, the impurity concentration within the crystal can be calculated through

$$(10.31) \quad C_{ic} = k_{diff} C_{il} \frac{\rho_c}{\rho_l}$$

where C_{il} is the impurity concentration within the solution and ρ_c and ρ_l are the densities for the crystal and the liquid, respectively. k_{diff} is computed in the following manner:

$$(10.32) \quad k_{diff} = f \left\{ \frac{C_{il}}{\rho_l - C_{il}} \left[\exp \left(\frac{G \rho_c}{k_d \rho_l} \right) - 1 \right] \right\}$$

where f expresses that k_{diff} is a function of what is inside (in a first approach it can be considered a linear function and thus f is another parameter to be determined) and k_d is the mass transfer coefficient.

In order to link the ice scaling with the total heat transfer, the model can be completed assuming that there are no heat losses. Therefore, the total heat transfer can be defined as:

$$(10.33) \quad Q = \dot{m}_c C p_c (T_{c,out} - T_{c,in})$$

where m_c is the mass flow rate of the coolant, $C p_c$ is its specific heat and $T_{c,out}$ and $T_{c,in}$ are the temperatures of the coolant at the exit and inlet, respectively. This heat transfer can be also related to the crystallization within the vessel as:

$$(10.34) \quad Q = \dot{m}_f \Delta H_f$$

where the subscript f corresponds to the crystallized liquid and ΔH is the heat of crystallization.

Since one of the hypotheses of the model is that there are no heat losses, then

$$(10.35) \quad Q = q_c = q_w = q_s = q_l$$

where the subscripts refer to the coolant (c), vessel wall (w), ice scaling (s) and slurry (l).

The heat transfer in each of those elements of the system is described by the following equations:

$$(10.36) \quad q_c = h_c 2\pi R_o L (T_o - T_c)$$

$$(10.37) \quad q_w = k_w 2\pi L \frac{(T_i - T_o)}{\ln \left(\frac{R_o}{R_i} \right)}$$

$$(10.38) \quad q_w = k_{ice} 2\pi L \frac{(T_{s,i} - T_i)}{\ln \left(\frac{R_i}{R_i - \gamma} \right)}$$

$$(10.39) \quad q_l = h_l 2\pi (R_i - \gamma) L (T_l - T_{s,i})$$

where h and k are the conductive and convective heat transfer coefficients, respectively, and the combined subscript s,i refers to the inner surface of the ice scaling. The overall heat transfer resistance, referred to the external area, can be computed as:

$$(10.40) \quad \frac{1}{U} = \frac{Q}{2\pi L R_o} \Delta T$$

$$(10.41) \quad \frac{1}{U} = \frac{1}{h_c} + \frac{R_o \ln\left(\frac{R_o}{R_i}\right)}{k_w} + \frac{R_o \ln\left(\frac{R_i}{R_i - \gamma}\right)}{k_{ice}} + \frac{R_o}{(R_i - \gamma)h_l}$$

Combining the previous set of equations for q , if the temperature of the inner surface of the scaling is equal to the temperature of the slurry, then after some mathematical manipulation the scaling thickness can be computed as:

$$(10.42) \quad \gamma = R_i - \frac{QR_i}{(T_l - T_i)2\pi Lk_{ice}}$$

and consequently, if the scaling thickness and slurry temperature are known, the total heat required can be estimated as:

$$(10.43) \quad Q = \left(1 - \frac{\gamma}{R_i}\right) (T_l - T_i) 2\pi Lk_{ice}$$

In the same manner, if the scaling thickness and total heat transfer are known, the slurry temperature can be estimated:

$$(10.44) \quad T_l = T_i + \frac{QR_i}{(R_i - \gamma)2\pi Lk_{ice}}$$

However, it must be checked if the hypothesis $T_{s,i}=T_l$ holds true in the experiments.

10.3. Experimental Validation

10.3.1. Objective

Validation experiments can serve to determine the following:

- Growth rate of the ice scaling
- Purity of the ice scaling
- Quantity and purity of both salt and ice crystals in the slurry
- Variation of the effective viscosity as a result of crystallization

The variables that affect the parameters to be studied are:

- Subcooling temperature
- Rotational speed
- Initial concentration
- Time

10.3.2. Experimental Campaign

The numerical model of the Eutectic Freeze Crystallization (EFC) allows determining the scaling induction time in the stirred crystallizer as a function of different variables, such as the temperature

difference between the stirred tank wall and the bulk solution, the rotational speed in the crystallizer and the salt concentration, and under certain restrictions (ice purity). That scaling induction time, along some other variables, can allow computing the different overall output parameters of interest. Nevertheless, numerical simulation must be validated. This task was planned to be carried out at CTM once a new 5 litres EFC reactor will be fully implemented in a test-rig.

A synthetic 4 wt% Na₂SO₄ (aq) solution needs to be prepared by dissolving analytical-grade Na₂SO₄ from Merck (>99%) in deionized water of resistivity 6.2 MΩcm. Dissolution has to be performed at room temperature under 300 rpm mixing condition for 30, 60, 90 and 120 min. Experiments has to be conducted at different temperature driving forces DTML (bulk, secondary flow) and the rotational speed of the impeller (e.g., 100 rpm, 200 rpm, 300 rpm), at a constant level of initial undercooling of about 0.25 C and residence time described previously in an experimental setup.

The experiments was planned to be conducted in a 5-L jacketed vessel type crystallizer (supplied by VidraFoc, Barcelona, Spain) with a concave bottom section to facilitate the settling of salt crystals. The ice slurry is expected to overflow through the top section. The crystallizer is insulated properly to prevent heat loss to the environment. A paddle with two blades is located in the middle section of the crystallizer and connected to a motor to agitate the solution in the crystallizer.

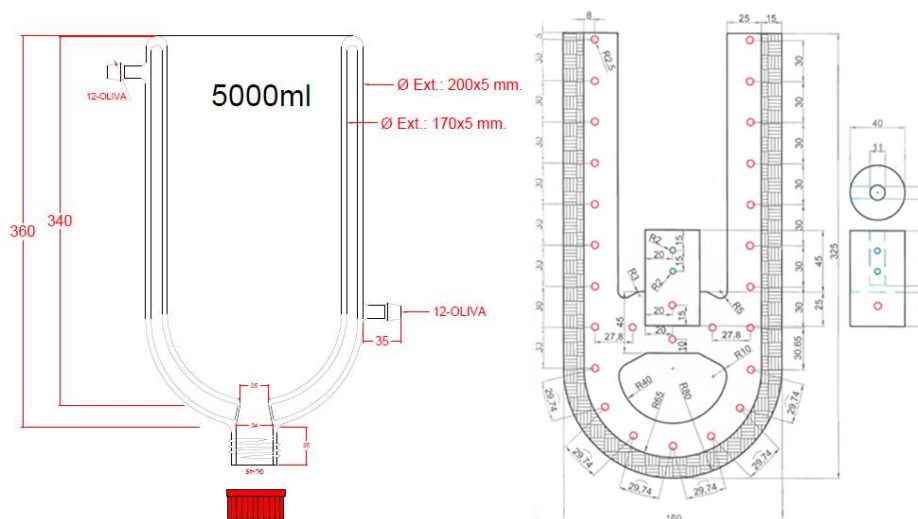


Figure 18: EFC Reactor layout.

The feed solution can be precooled by a heat exchanger in which the thermal fluid coolant is pumped by a cryo-compact Julabo Thermal Bath CF31 (supplied by Julabo, Seelbach, Germany). The temperature of the crystallizer content is controlled indirectly by means of a silicone oil coolant flowing through the crystallizer jacket. The coolant is circulated through the jacket of the crystallizer and exchanged heat with the solution inside the crystallizer. A DIN 1/10 PT100 temperature sensor with an accuracy of ± 0.01 °C can be used to measure the temperature of the solution. The onset of ice-scaling

in the middle part of the crystallizer wall can be detected by visual inspection focused on the crystallizer wall adjacent to the coolant inlet in the jacket, which is likely to form ice scale first in the crystallizer. A light source can be used to illuminate that part of the crystallizer. Compressed air is expected to be used to blow deposited condensate on the focused area in order to get a clear image.

Determining the induction time for ice-scaling (t_{ind}) is a method that can be used to control and extend the requirements of EFC processes. In this work, t_{ind} has been defined as the time elapsed after adding seed-ice to the solution to the onset of ice-scaling on the crystallizer wall.

The physical properties of the 4 wt% Na_2SO_4 (aq) solution can be obtained by using the correlation by (Hasan and Louhti-Kultanen 2015) (Hasan et al. 2017).

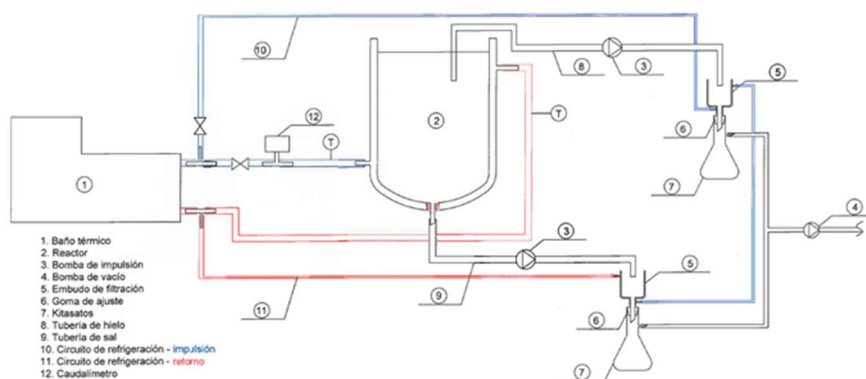


Figure 19: EFC Reactor experimental diagram.

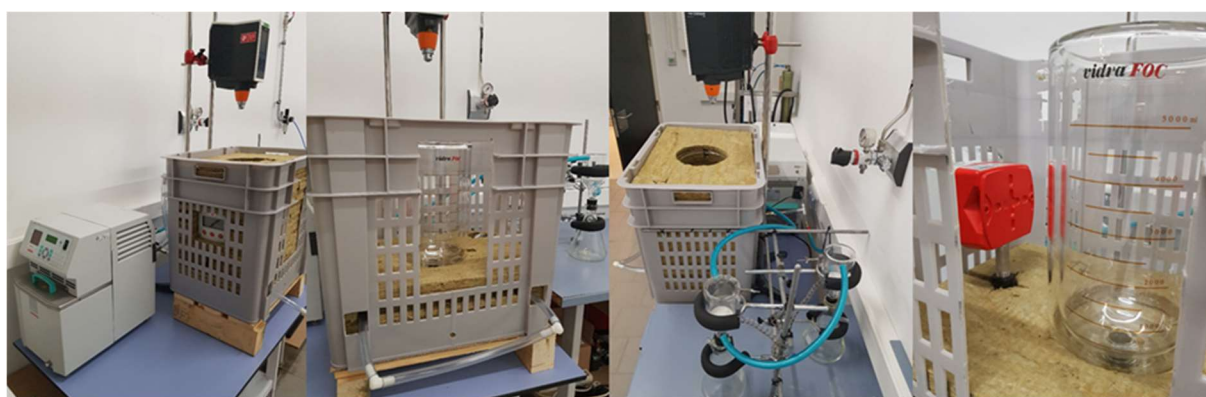


Figure 20: EFC Reactor layout.

In order to complete a successful experimental campaign, it is critical to obtain separately the four phases present in the vessel: ice scaling, liquid and both salt and ice crystals at the bulk. A sufficient number of experiments should be carried out to properly determine the influence of each of the variables. However, due to the large number of experiments required, there need to be two experimental campaigns. The first one serves to determine the influence of time, subcooling

temperature and rotational speed, while the second one yields the influence of the initial concentration and the effect of the variation of viscosity. Table 13 summarizes the experiments to be carried out during the first campaign with a fixed initial concentration.

Table 13: Experiments planned for the first experimental campaign.

Experiment	Subcooling (K)	Rotational speed (rpm)	Time (min)
1	0.25	0	30
2	0.25	0	60
3	0.25	0	90
4	0.25	0	120
5	1.00	0	30
6	1.00	0	60
7	1.00	0	90
8	1.00	0	120
9	4.00	0	30
10	4.00	0	60
11	4.00	0	90
12	4.00	0	120
13	0.25	300	30
14	0.25	300	60
15	0.25	300	90
16	0.25	300	120
17	1.00	300	30
18	1.00	300	60
19	1.00	300	90
20	1.00	300	120
21	4.00	300	30
22	4.00	300	60
23	4.00	300	90
24	4.00	300	120

The quantity of each of the phases has to be measured by voiding the vessel, filtering the bulk and separating the salt and ice crystals. Then, the ice scaling will melt. At the end, the four different phases can be obtained separately and weighted. To obtain the concentration of each phase an electrical conductivity sensor can be used. Finally, the ice scaling thickness has to be measured through a semi-numerical approach, considering the geometry of the ice, which depends on the temperature difference.

As commented previously, the goal of a combined EFC-Waste Heat Recovery System is the maximization of COP_{th}, COP_{el} of the system (waste heat is used to drive a chiller in order to deliver

cooling), control of ice growth velocity (function of the other conditions, such as temperature and concentration differences) and ice purity. Ice growth velocity is directly related to ice purity. These data will be used as the basis to define different control strategies of cooling delivery in order to evaluate waste heat recovery potential, being directly transformed to energy savings.

11. Electrodialysis Model

Electrodialysis (ED) is an electrochemical desalination process which uses a combination of semipermeable membranes and an electric field across the electrodes to remove the dissolved ions from the solution (Curto, Franzitta et al. 2021). Initially conceptualized for demineralizing sugar syrup, the technology has been developed for saline water desalination and it can be designed for several applications including city-scale brine water desalination, village-scale water treatment, seawater brine concentration, denitrification of water for municipal water supply, demineralization of wine, whey and sugar, in-house water treatment and wastewater treatment (Nayar, Fernandes et al. 2019).

11.1. Working Principle

As illustrated in Figure 21, an ED system primarily consists of several pairs of alternatively arranged anion exchange membranes (AEM) and cation exchange membranes (CEM) which are selectively permeable to anions and cations respectively (Nayar, Fernandes et al. 2019). The saline feedwater is fed through a feed channel between all the cell pairs. When an electric field using direct current is applied across the two electrodes, the cations (positive ions, such as Na^+ , Ca^{++}) are attracted by the anode, while the anions (negative ions, such as Cl^- , HCO_3^- , CO_3^{--}) are attracted by the cathode (Curto, Franzitta et al. 2021).

Since the AEM and CEM are only selectively permeable, the migration of ions towards the electrodes is selectively stopped by these membranes. For example, during its motion to the anode, a positive ion (cation) can cross the CEM but not the AEM and vice versa for the anions. As a result, the ions are confined inside the brine or 'concentrate' channels, removing ions from the freshwater or 'diluate' channels (see Figure 21) (Curto, Franzitta et al. 2021). The type of AEMs and CEMs is chosen based on the application. For example, for salt (NaCl) production from seawater, they are additionally selective to monovalent ions (Nayar, Fernandes et al. 2019).

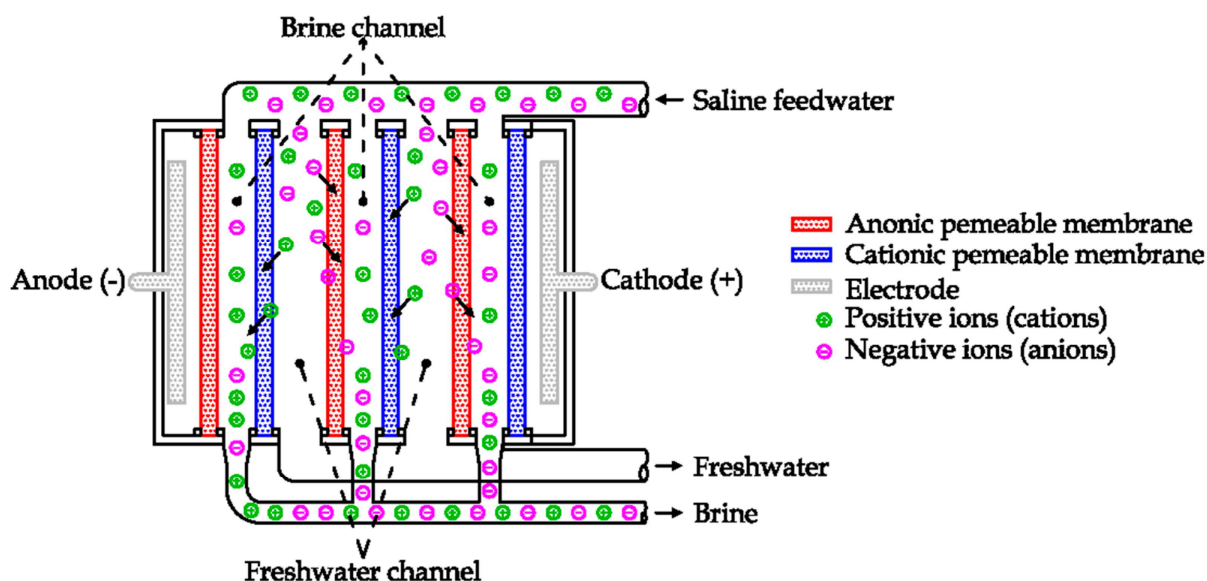


Figure 21: Simplified graphical illustration of the working principle of an electro dialysis unit (Curto, Franzitta et al. 2021).

11.2. Mathematical Modelling

In order to accurately describe the electro dialysis (ED) process and develop effective process simulation tools it is necessary to implement mathematical models able to consider a number of complex phenomena. These include, among others:

- Solution-membrane equilibria
- Concentration polarization
- Fluid flow behaviour along channels
- Mass transport phenomena
- Mass balance in the compartments
- Electrical phenomena

Several different modelling approaches have been presented so far in the literature, each one addressing in a different way and to a different extent all these aspects. These modelling tools are generally classified into **simplified** and **advanced** modelling approaches. The first class of process models is characterized by a highly simplified approach based on neglecting most non-ideal phenomena and on the use of lumped parameters equation. Simplified models are commonly adopted for a first rough design of ED equipment. The second and wider class of process models can be divided into two sub-categories: 1) rigorous Nernst-Planck (N-P) or Stefan-Maxwell (S-M) based *theoretical models* and 2) *semi-empirical models*. In both cases, non-ideal phenomena are accounted for and models typically include mass balance differential equations in order to describe the variation of process parameters along the flow direction. Semi-empirical models are based on a multi-scale approach, in which lower scale phenomena (such as mass transfer and fluid behaviour, leading also to

the characterization of diffusion boundary layer) are described by means of empirical information or small-scale theoretical analysis, e.g. by means of a Computational Fluid Dynamics tool.

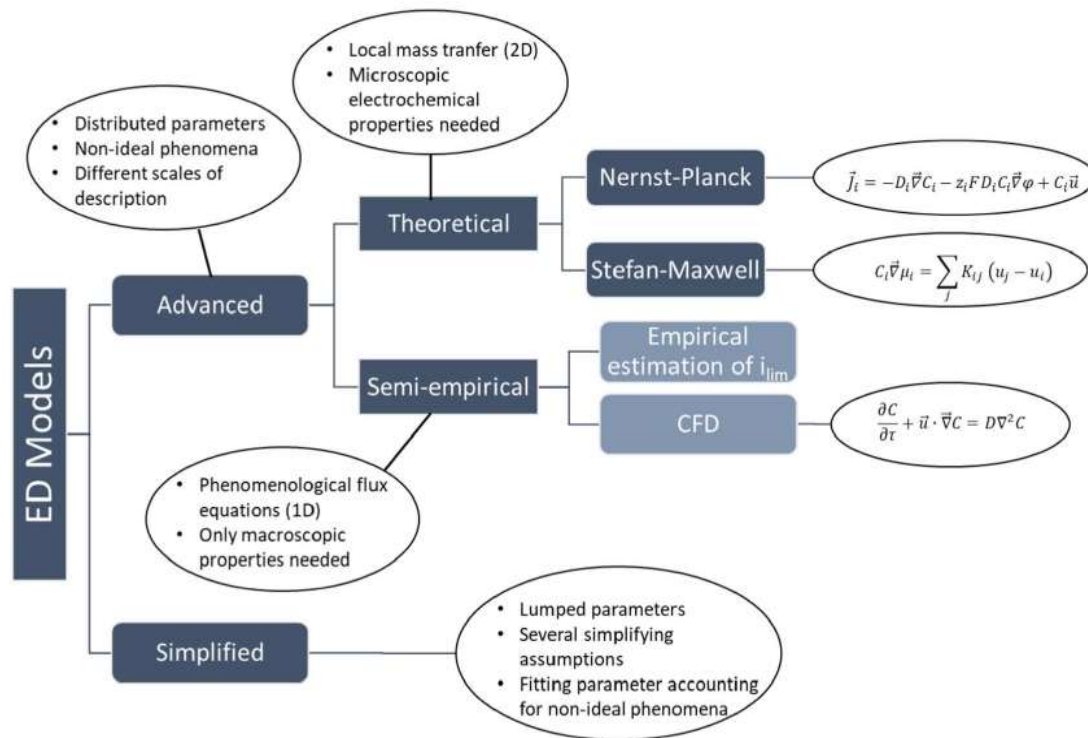


Figure 22: Block diagram showing the classification of ED modelling approaches along with the main features of each class of models (Campione et al. 2018).

In the current work, the techno-economic modelling of ED for salt (NaCl) concentration is based on the work of Nayar et al. (Nayar, Fernandes et al. 2019) which itself is adapted from a semi-empirical model developed by McGovern et al. (McGovern, Weiner et al. 2014). In the ZERO BRINE project, notably for the Bolesław Śmiały coalmine case study and Debiensko coalmine replication study, a cascade system of two ED units operating in a single-pass mode has been implemented. Due to the parameter requirement of the chosen modelling approach, independent modelling of each ED unit was not possible. As such, ED has been modelled as a single unit instead of a cascade system (Pawar, Mitko et al. 2021). An ED system consists of several pairs (N_{cp}) of anion-exchange membranes (AEM) and cation exchange membranes (CEM), where each pair of AEM and CEM constitutes one “cell-pair” (Nayar, Fernandes et al. 2019). These cell-pairs make up the “ED stack” together with the cathode, anode, concentrate and diluate channels. The ED unit used for concentrating the brine is modelled as a “single stage” design. This means that the change in the concentrate salinity from inlet ($S_{c,i}$) to outlet ($S_{c,o}$) occurs across a single ED cell-pair. To simulate the salt and water transport across the stack for the calculation of cell-pair area A_{cp} , the length of the stack is discretized into 50 computational cells ($N=50$) such that each cell sees the same change in salinity on the concentrate side:

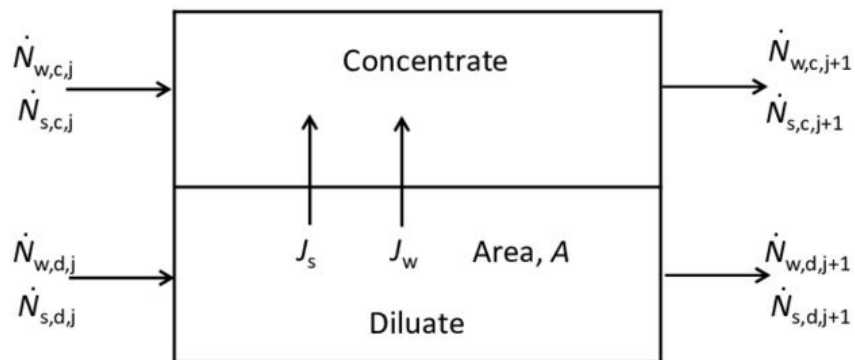
$$(10.1) \quad S_{c,k+1} = S_{c,k} + \frac{S_{c,o} - S_{c,i}}{N - 1}$$

where $S_{c,i}$ and $S_{c,o}$ are the salinities at the inlet and outlet of the concentrate stream and $k = 1$ to $N - 1$.

The salt and water transport in an ED computational cell are depicted in Figure 23. The molar flow rates of salt and water at $j=1$ or at the entrance to the concentrate and diluate channels are based on known mass flow rates. The below two equations illustrate the calculation for the concentrate channel:

$$(10.2) \quad \dot{N}_{s,c,j} = \frac{\dot{m}_{c,j} \cdot S_{c,i}}{1000 \cdot MW_s}$$

$$(10.3) \quad \dot{N}_{w,c,j} = \frac{\dot{m}_{c,j} \cdot (1000 - S_{c,i})}{1000 \cdot MW_w}$$



$$\text{where, } A = N_{cp} \times A_{cp}$$

Figure 23: Transport of salt and water in an ED computational cell (Nayar, Fernandes et al. 2019).

After passing through the first computational cell, the new molar flow rates of salt ($\dot{N}_{s,c,j+1}$) and water ($\dot{N}_{w,c,j+1}$) in the concentrate channels are based on the net salt flux ($J_{s,j}$) and net water flux ($J_{w,j}$) from the diluate channel into the concentrate channel (refer Figure 23):

$$(10.4) \quad \dot{N}_{s,c,j+1} - \dot{N}_{s,c,j} = A_{cp,tot,j} \cdot J_{s,j}$$

$$(10.5) \quad \dot{N}_{w,c,j+1} - \dot{N}_{w,c,j} = A_{cp,tot,j} \cdot J_{w,j}$$

where $A_{cp,tot,j}$ is the total cell-pair area across the stack discretized to each computational cell. Thus, the number of cell pairs can be determined by:

$$(10.6) \quad N_{cp} = \frac{\sum_{j=1}^N A_{cp,tot,j}}{A_{cp}}$$

The effective cell-pair area for each membrane pair (A_{cp}) is based on manufacturer's data and is chosen as 0.395 m² in this work (Chemicals 2013).

To obtain the net salt ($J_{s,j}$) and water flux ($J_{w,j}$) for each computational cell, the transport model of McGovern et al. is applied:

$$(10.7) \quad J_{s,j} = T_{s,j} \cdot \frac{i_j}{F} - L_{s,j} \cdot (C_{c,m,j} - C_{d,m,j})$$

$$(10.8) \quad J_{w,j} = T_{w,j} \cdot \frac{i_j}{F} - L_{w,j} \cdot (\pi_{c,m,j} - \pi_{d,m,j})$$

where, $T_{s,j}$ and $T_{w,j}$ are the salt and water transport numbers for the ED membrane and $L_{s,j}$ and $L_{w,j}$ are the salt and water permeabilities of the membrane. $C_{c,m,j}$ and $C_{d,m,j}$ are the molar concentrations of salt in the concentrate and diluate at the surface of the membrane. McGovern et al. have expressed the experimentally-determined transport and permeability numbers for a NEOSEPTA AMX and CMX membranes in the form of simple correlations:

$$(10.9) \quad T_s^{cp} = -4 \times 10^{-6} S_d^2 + 4 \times 10^{-5} S_d + 0.96 \pm 0.04$$

$$(10.10) \quad T_w^{cp} = -4 \times 10^{-5} S_c^2 - 10.9 \times 10^{-2} S_d + 11.2 \pm 0.06$$

$$(10.11) \quad L_s^{cp} = \min(2 \times 10^{-12} S_d^2 - 3 \times 10^{-10} S_d + 6 \times 10^{-8}, 2 \times 10^{-12} S_c^2 - 3 \times 10^{-10} S_c + 6 \times 10^{-8}) \pm 6 \times 10^{-9}$$

$$(10.12) \quad L_w^{cp} = 5 S_c^{-0.416} \pm 2 \times 10^{-5}$$

The molar flow rate of salt and water in the diluate in 'j+1'th computational cell is calculated using:

$$(10.13) \quad \dot{N}_{s,d,j+1} - \dot{N}_{s,d,j} = -A_{cp,tot,j} \cdot J_{s,j}$$

$$(10.14) \quad \dot{N}_{w,d,j+1} - \dot{N}_{w,d,j} = -A_{cp,tot,j} \cdot J_{w,j}$$

It should be noted that the authors used finite-difference method to perform species balance on each channel (Chehayeb, Farhat et al. 2017, Nayar, Fernandes et al. 2019). In our work, it was not possible to perform this analysis and we neglect the water flux for the calculation of A_{cp} . This results in a lower $A_{cp,tot}$ as compared to that computed by Nayar et al. for an industrial stack (self-calculation: 20.5 m², Nayar et al.: 22.7 m² and industrial stack: 24 m²). To improve the accuracy of the economic and energy consumption calculation, we have introduced a so-called "area correction factor" which increases the $A_{cp,tot}$ by 17% (in this example from 20.5 m² to ~24 m²). Based on the new cell-pair area $A_{cp,tot (corrected)}$, we recalculate N_{cp} which is then used for the calculation of cell-pair voltage V_{cp} using the following expression (McGovern, Weiner et al. 2014):

$$(10.15) \quad V_{cp} = \left(\bar{r}_{am,j} + \bar{r}_{cm,j} + \frac{h_d}{\sigma \Lambda_d C_{d,j}} + \frac{h_c}{\sigma \Lambda_c C_{c,j}} \right) i_j + \frac{\bar{r}_{cm,j}}{N_{cp}} i_j + \frac{2h_r}{\sigma k_r N_{cp}} i_j + E_{am,j} + E_{cm,j}$$

(Nayar, Fernandes et al. 2019) explains this equation using Figure 24 below. From left to right, the terms in equation (10.15) represent the resistances of the AEM and CEM, the diluate and concentrate channel resistances, the resistance of an extra CEM at the end of a stack, the resistance of the rinse stream which may be present in stacks, and the voltage drops across the AEM and CEM arising from concentration polarization. It should be noted that the resistance of the rinse stream is neglected in the current study.

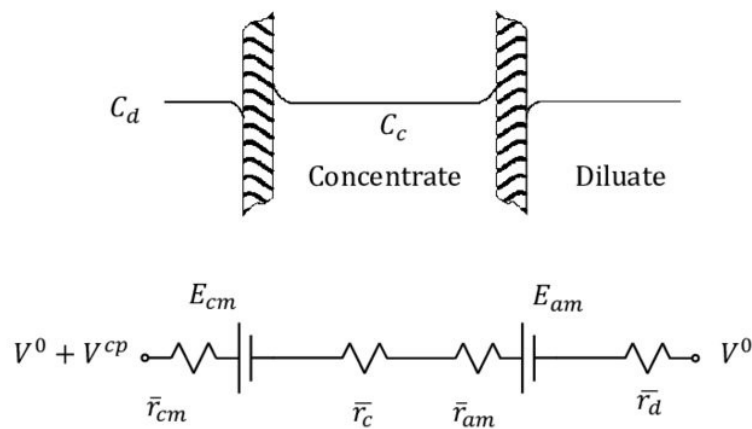


Figure 24: Circuit diagram of an ED cell-pair (Nayar, Fernandes et al. 2019).

Using the voltage across the electrodes, the total voltage across the ED stack is calculated as:

$$(10.16) \quad V_{ED,stack} = N_{cp} V_{cp} + V_{el}$$

The stack power is then calculated as:

$$(10.17) \quad \dot{W}_{ED,stack} = \sum_{j=1}^N i_j A_{cp,j} (N_{cp} V_{cp} + V_{el})$$

The power required for pumping the concentrate and diluate is calculated using (McGovern, Zubair et al. 2014):

$$(10.18) \quad \dot{W}_{ED,pump} = \frac{\Delta P_{dil} \dot{V}_{dil,in}}{\eta_{p,ED}} + \frac{\Delta P_{con} \dot{V}_{con,in}}{\eta_{p,ED}}$$

The total power required for the ED unit is calculated as:

$$(10.19) \quad \dot{W}_{ED} = \dot{W}_{ED,stack} + \dot{W}_{ED,pump}$$

Based on the electricity cost and a plant capacity factor, we can then calculate the annual energy costs of the ED system $OpEx_{ED,energy,yr}$. Other operating costs include costs for membrane replacement, maintenance and labour. Nayar et al. assumes a membrane cost ($SpCost_{ED,mem,m}$) of 222 USD/m² of membrane. The capital cost for one set of ED membranes is given by:

$$(10.20) \quad capEx_{Ed,mem} = SpCost_{ED,mem,m} \times A_{mem,total}$$

where the total membrane area is calculated by:

$$(10.21) \quad A_{cp,total} = N_{cp} \sum_{j=1}^N A_{cp,j}$$

$$(10.22) \quad A_{mem,total} = 2 \frac{A_{cp,total}}{Mem_{eff}}$$

where the factor 2 accounts for the fact that each cell pair has two membranes and Mem_{eff} accounts for the fact that only a portion of the membrane area is used for transport due to the presence of spacers and gaskets (Nayar, Fernandes et al. 2019).

Considering a membrane life of 7 years, Nayar et al. calculates the annual membrane cost as follows:

$$(10.23) \quad OpEx_{Ed,mem,yr} = \frac{CapEx_{ED,mem}}{Annuity_{factor}} \times [(1 + r_{return})^{-7} + (1 + r_{return})^{-14}]$$

The labour cost ($OpEx_{Ed,labor,yr}$) is calculated in relation to the mass flow rate through the ED system (Micari 2020). As per Nayar et al., the specific annual cost of maintenance ($SpCost_{ED,maint,m}$) and chemicals ($SpCost_{ED,chem,m}$) are taken as 8.5 and 2.1 USD/m²-year respectively. Thus, the annual maintenance and chemical costs are calculated as:

$$(10.24) \quad OpEx_{Ed,maint,chem,yr} = (SpCost_{ED,maint,m} + SpCost_{ED,chem,m}) \times A_{mem,total}$$

Finally, the total annual operating expenses are:

$$(10.25) \quad OpEx_{Ed,yr} = OpEx_{Ed,energy,yr} + OpEx_{Ed,mem,yr} + OpEx_{Ed,labor,yr} + OpEx_{Ed,maint,chem,yr}$$

The total capital cost of the ED system is calculated as:

$$(10.25) \quad capEx_{Ed,total} = SpCost_{ED,CapEx,m} \times A_{mem,total}$$

where Nayar et al. assumes the specific capital cost of a high salinity ED ($SpCost_{ED,CapEx,m}$) as 600 USD/m² of membrane. The total ED capital cost is then annualized using an annuity factor.

11.3. Model Validation

Since the type of ED system used in the ZERO BRINE project has a different configuration (two ED units in a cascade system operating in continuous mode) than the one modelled (a single ED unit operating in continuous mode), a one-to-one comparison with the ED used at the project site would not be possible. Moreover, the modelled ED would potentially have a smaller installed capacity than the implemented cascade system, as the model will provide an optimized size for the given flow and ion conditions. Thus, we have validated the model results, namely cell-pair area and electricity consumption, by comparing them with an industrial ED and literature respectively. As already discussed in the preceding section, our model estimates a cell-pair area ($A_{cp,tot}$) of 20.5 m² as against an industrial stack with 24 m². The estimated cell-pair area was then “corrected” to 24 m² using an “area correction factor”, which has then been used for as a correction parameter in the simulation. The model results for electricity consumption are validated by comparing it with those from Nayar et al. for a “standalone ED system” which has the following parameters: a concentrate inlet flow rate of 50 m³/h, a diluate-to-concentrate inlet ratio of 80, ED current density of 300 A/m², concentrate and diluate inlet salinity of 35 g_{salt}/kg_{sol}, concentrate outlet salinity of 200 g_{salt}/kg_{sol} and a corresponding annual salt production of 96,836 ton_{NaCl}/year (based on Nayar et al.’s method). For the same conditions, our model estimates a specific energy consumption of 210 kWh_{el}/ton_{NaCl} as against 219 kWh_{el}/ton_{NaCl} estimated by Nayar et al., which is within 4.1%. Thus, using these two methods, we have validated the calculation of cell-pair area and electrical consumption of our ED model.

11.4. Nomenclature

Acronyms

AEM	Anion exchange membrane
CEM	Cation exchange membrane
CapEx	Capital expenditure [USD]
ED	Electrodialysis
OpEx	Operational expenditure [USD]

Roman symbols

A	area [m ²]
i	current density [A/m ²]
J	molar flux [mol/m ² .s]
L _s	salt permeability [m ² /s]
L _w	water permeability [mol/m ² .s.bar]
Mem _{eff}	membrane effectiveness [-]
ṁ	mass flow rate [kg/s]
Ṅ	molar mass flow rate [mol/s]
P	pressure [bar]
r	rate of return on capital [-]
r̄	area resistance [Ωm ²]
S	salinity [kg _{salt} /kg _{sol}]
T	temperature [°C]

T_s	membrane salt transport number [-]
T_w	membrane water transport number [-]
V	voltage [V]
\dot{V}	volume flow rate [m ³ /s]
\dot{W}	power [W]

Subscripts

c	concentrate
cp	cell-pair
d	distillate
el	electrode or electrical
i	inlet
o	outlet
tot	total

12. RCE Integration

12.1. RCE Integration Environment

In ZERO BRINE, several different groups of scientists provide inputs for technology tools for specific tasks. These tools have to be integrated into one single software to be used together in the envisioned scientific projects. Furthermore, the tools need to be accessible to everyone inside the project without additional overhead or maintenance effort. To address this requirement, RCE was adapted to suit the needs of the ZERO BRINE project and to make the developed tools easily available.

RCE was developed at DLR as an open source, freely available, platform independent and distributed integration environment for scientists and engineers to analyse, optimize, and design complex systems. RCE provides a platform for sharing different tools from different teams within the project, grouping them into functional workflows that can be executed automatically. As each tool has to be integrated only once to be accessible to everyone in the project, both the maintenance and the integration effort are low and manageable. Therefore, RCE is fulfilling the requirements detailed above.

RCE provides a reliable method to couple tools of different kinds into one functional super-model or simulation. Each tool is represented as a block that can be connected to other blocks. Each block represents a tool, each connection an exchange of data. This creates a workflow which can be executed at the push of one button. Due to its distributed nature, tools can be used both locally and remotely by the internet at the same time in the same workflow.

RCE is extensible and supports different scientific applications with a wide range of requirements. Coupling of external tools into workflows is a central feature of RCE and as each tool or model has to be integrated only once to be accessed using standardized inputs and outputs throughout a network of RCE servers by RCE clients, it adds only a low overhead to the development of tools. Each tool output

can be configured to be passed along the workflow as input to another tool or as results for storage to disk.

A tool is executed by RCE once all required input data is available, either from other tools or provided by the user. Tool and workflow execution are therefore automated, so no user interaction is required during execution. Result data are generated by the tools of a workflow during its execution and collected by RCE, which provides them in a graphical viewer to the scientist or as data files.

In complex analyses, designs, or simulation tasks like it is the case in ZERO BRINE, multiple experts and tools are involved, which are located at different sites. To support collaboration, RCE is designed in two components, a server and a client. The servers host integrated tools and make them available to clients of scientists and engineers in a peer-to-peer network.

12.2. RCE Server

The RCE server is the heart of the integration environment, as it provides access to all tools integrated into it. The RCE server is only responsible for executing (partial) workflows, collecting results and handing them off to the client and therefore does not feature the graphical user interface provided by the RCE client. The RCE server is run on dedicated hardware, as it does all calculations of the tools it provides access to. Within the RCE server, tools can be integrated, as long as they do not require user input through a graphical user interface at runtime. All tools with command line interfaces, no matter the programming language, can be integrated via a flexible scripting interface based on Python within RCE.

The tools can then be accessed by RCE clients remotely and via their respective graphical user interfaces. The tools on the RCE server can be chained into workflows by the users through the client and executed as if they were one large program. The RCE server provides its integrated tools as building blocks. It manages data transfer between the users and in between tools. As a data driven environment, the server automatically executes tools, when the prerequisite data is available and collects the output. Output can be represented to the user via the graphical user interface of the client or as data files.

If multiple RCE servers are available, they can be connected into one network, providing their respective tools like one seamless single program to all connected clients. All data handling during execution of workflows is done by RCE without the need of interference by the user. RCE servers are responsible only for executing their tools and for transferring the created data. Workflows can be defined including tools hosted on multiple servers, in the same way, as if all tools were available on one single server or locally on the client.

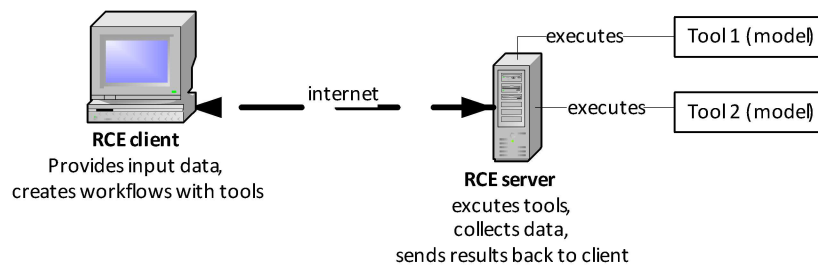


Figure 25: Schematic representation of the integration approach of RCE.

12.3. The RCE Client

The RCE client software features a graphical user interface for designing workflows and for tool integration. Users can either use it locally, with local tools integrated to RCE executing local workflows. Or they can connect to one or a network of remote RCE server by the internet. Then the client has access to all tools locally in the client and remotely on each RCE server. The user can then create workflows from all available tools. All data transfer is handled by RCE and protected by encryption and automated without the need of user interaction. The scientist can therefore focus solely on creating workflows out of the available tools and executing them.

12.4. Tool Integration

Tools are easily integrated into RCE with a graphical tool provided by the client. The integrated tool can then be transferred to an RCE server to be made available to all clients, or used locally only in this RCE client. Within RCE the first step to integrate a tool, is the creation of a new block. The block later represents the tool in workflows and can be used in the graphical user interface. The block can be configured with all inputs and outputs needed by the tool. This allows RCE to check for inputs and outputs automatically during execution and enables RCE to start the tool when all required data is available. Integration is a simple task of writing minimal Python wrappers feeding the inputs from RCE toward the tool and the output of the tool backward to RCE. Data can be cleaned, reshaped and adapted to the tool from within Python at this step if necessary. Afterwards the tool represented by its block is available for execution in workflows.



Figure 26: General approach to integrate tools in RCE.

12.5. Technical Aspects of RCE

RCE is written in Java and therefore platform independent. It can be installed and executed on linux, mac and windows operating systems and is capable of serving tools between these platforms. Thus, RCE is capable of integrating platform depending tools into one seamless tool that can be easily accessed by scientists through their RCE clients.

RCE is shipped only as one single java software package. It can be configured to either run as a server or as a client. This supports tool integration as the tool can first be integrated in client mode and then RCE can be started in server mode with the integrated tool, rendering a transfer of the integration data to the server superfluous.

12.6. RCE Integration of Tools

As part of WP5, DLR has completed the techno-economic modelling of several technology models (listed shortly hereafter) on Python which are made available to project partners on RCE as *Integrated Tools* via a server on the DLR side. Due to IT security regulations and firewall limitations, all project partners need fixed ip addresses to obtain a project-specific connection (in this case, for ZERO BRINE) to the RCE server, which have to be applied for in advance at DLR. Once the project partner is connected to the server via a so-called *Uplink Connection*, the partner can access the various technology tools on his RCE client under the tab *User Integrated Tools*. Following technology tools have been successfully published as *Integrated Tools* and can be used by project partners to simulate desired treatment chains. The **bold** names below are the same as the name of the *Integrated Tools* on RCE:

- **NF**: tool for the simulation of the nanofiltration (NF) technology
- **rej_membrane_NF**: converts the ionic plant rejection of NF, obtained from experimental data, into ionic ‘membrane rejection’, which is the required format of the rejection file for the NF tool
- Crystallizer: under this category, several technology tools have been developed to suit specific use cases
 - o **Crystallizer**: using a solution of NaOH, this tool simulates a crystallizer that precipitates Mg and Ca ions as Mg(OH)₂ and Ca(OH)₂ respectively
 - o **Crystallizer_CaSulphate_MgHydro**: simulates a crystallizer that is used for the precipitation of Ca and Mg ions from the brine in the form of CaSO₄ and Mg(OH)₂. Hydrated dolime solution (Ca(OH)₂.Mg(OH)₂) is used to provide OH ions
 - o **Crystallizer_NaCarbo_CaCarbo**: simulates a crystallizer that is used for the precipitation of Ca ions from the brine in the form of CaCO₃. An alkaline solution of Na₂CO₃ is used to provide CO₃ ions in addition to those present in the brine solution

- **Crystallizer_NaOH_MgHydro**: simulates a crystallizer that is used for the precipitation of Mg ions from the brine in the form of $Mg(OH)_2$. An alkaline solution of NaOH is used to provide OH ions
- **NaCl_Crystallizer**: used for the precipitation of NaCl crystals from a saturated solution
- **ED**: simulates the electrodialysis (ED) technology that is used to concentrate a solution with Na and Cl ions (other ions, if present, are neglected)
- **RO**: simulates the reverse osmosis (RO) technology
- **MED**: simulates the multi-effect distillation (MED) technology

12.7. Prerequisites

In order to access these tools and create own workflows on RCE, the following prerequisites should be met along with obtaining the project-specific server access discussed previously:

- Installing RCE: install the latest version of RCE with the help of RCE documentation (DLR 2021)
- Python environment and packages: create a virtual Python environment and ensure the installation of following packages on it:
 - Numpy
 - Pandas
 - Matplotlib
 - Scipy
 - Pyyaml
 - lapws
 - Xlwt
 - Xlrd
- Establishing Uplink Connection: once the server access has been granted, establish the Uplink Connection on RCE

12.8. Illustration of an RCE Tool and Modelling of a Treatment Chain

Chain

In this sub-section, the use and working of a technology tool (nanofiltration) will be illustrated. This will be followed by the explanation of an exemplary workflow which uses a combination of tools to simulate a treatment chain (Spanish replicability study).

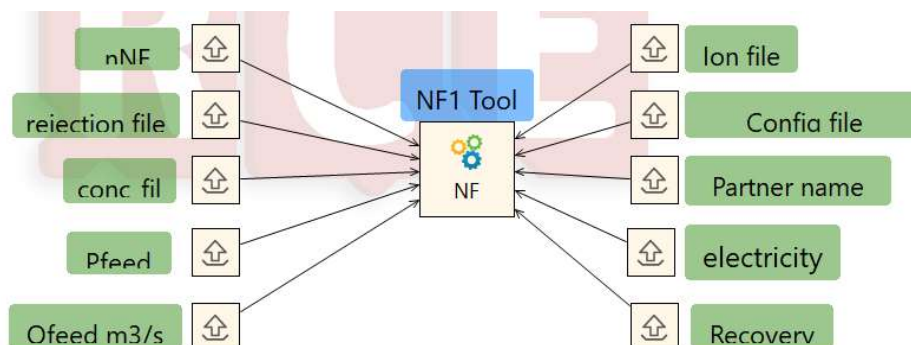


Figure 27: NF tool along with its input providers.

Figure 27 above is an excerpt of the RCE GUI that shows the NF tool at the centre connected to various *Input Providers* to its left and right. These *Input Providers* are different inputs, which are necessary to successfully simulate a tool. The NF tool, for example, requires the following inputs: volumetric flow rate [m^3/s], feed pressure [bar], ionic concentration [mol/m^3], ionic rejection [-], recovery rate [-], electricity cost [USD/kWh] and configuration file. The data type of the inputs should be taken care of (this can be checked in the *Component Properties* tab of a particular tool). For example, ionic concentration and ionic rejection files should be in yaml file format, whereas the flow rate is a float number. Once all the inputs are provided in correct format, the tool can be executed to obtain technical results (flow rate and ion concentrations in the permeate and retentate, electricity consumption, etc.) and economic results (capital and operating costs) in the form of an Excel file.

To illustrate the combined use of different technology tools to simulate a complete treatment chain on RCE, we take the example of the Spanish replicability study. In this study, a bench-scale experiment was performed to assess a treatment chain to process inorganic brine produced in an urban environment and to obtain valuable minerals and solutions from it. The inorganic brine mainly consists of Na, Cl, Mg, Ca, SO_4 , and HCO_3 ions. The proposed treatment chain aims at recovering valuable minerals like calcium, magnesium and sulphates in the form of calcium carbonate (CaCO_3), magnesium hydroxide ($\text{Mg}(\text{OH})_2$) and sodium sulphate (Na_2SO_4) respectively. As shown in Figure 28, it consists of a calcium and magnesium precipitator, ultrafiltration (UF), nanofiltration (NF) and an evaporator. The permeate from the NF is intended to be used as a purified brine in ion exchange resin processes. Assuming this permeate as the main product of the treatment chain, all the expenses and revenues

from CaCO_3 , Mg(OH)_2 , and Na_2SO_4 are represented in terms of levelized cost of purified brine (LBC) in USD/m^3 .

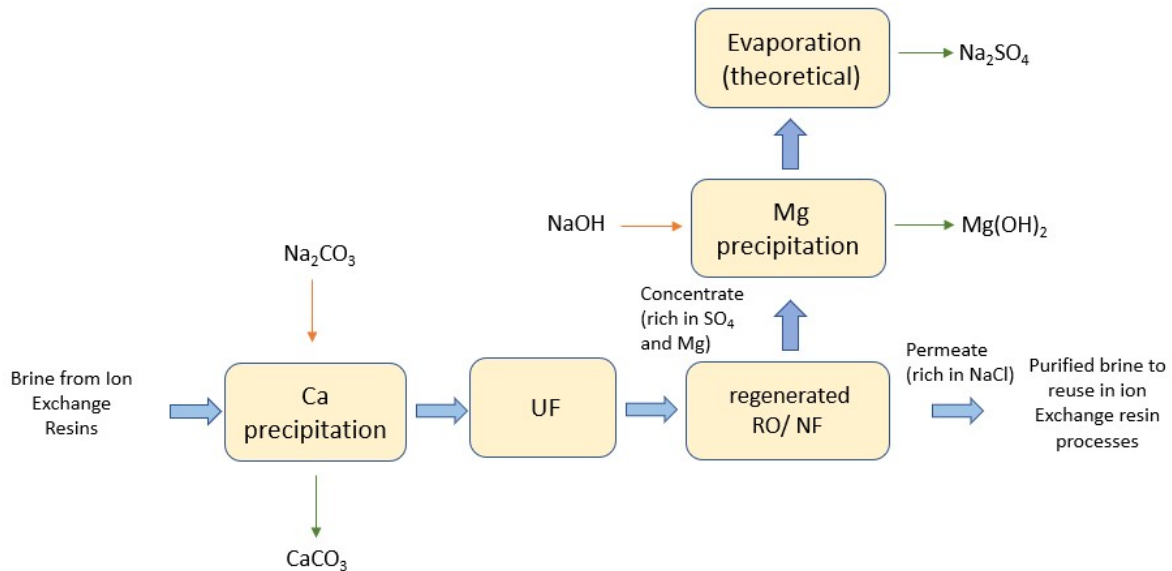


Figure 28: Schematic representation of the treatment chain in the Spanish replicability study.

The treatment chain's validation and assessment of economic feasibility are performed on the RCE platform. As shown in Figure 29, the modelled treatment chain consists of tools representing calcium and magnesium precipitators, and NF (pH adjustment, ultrafiltration (UF) and evaporator for Na_2SO_4 precipitation have not been modelled in RCE. Thus, the global economic calculations to determine the LBC do not reflect the costs for these components as well as the revenue from the recovery of Na_2SO_4).

Once all the necessary inputs are provided and the scripts for global economic calculations and the Excel joiner (the bottom two blocks in Figure 29) are modified to suit this particular chain, the techno-economic results are obtained in the form of two Excel sheets: i) Excel joiner output: this is simply the merging of outputs of different technology tools into one excel, ii) global economic output: this provides an outlook of the expenses and revenues of the entire treatment chain and expresses them in terms of levelized cost of the main product (in this case, pure brine or LBC) which is estimated using the following formula:

$$LBC \left[\frac{\text{USD}}{\text{m}^3_{\text{brine}}} \right] = \frac{\text{CAPEX} + \text{OPEX} - \text{Revenue}_{\text{CaCO}_3 + \text{Mg(OH)}_2} \left[\frac{\text{USD}}{\text{year}} \right]}{\text{NF permeate or brine} \left[\frac{\text{m}^3_{\text{brine}}}{\text{year}} \right]}$$

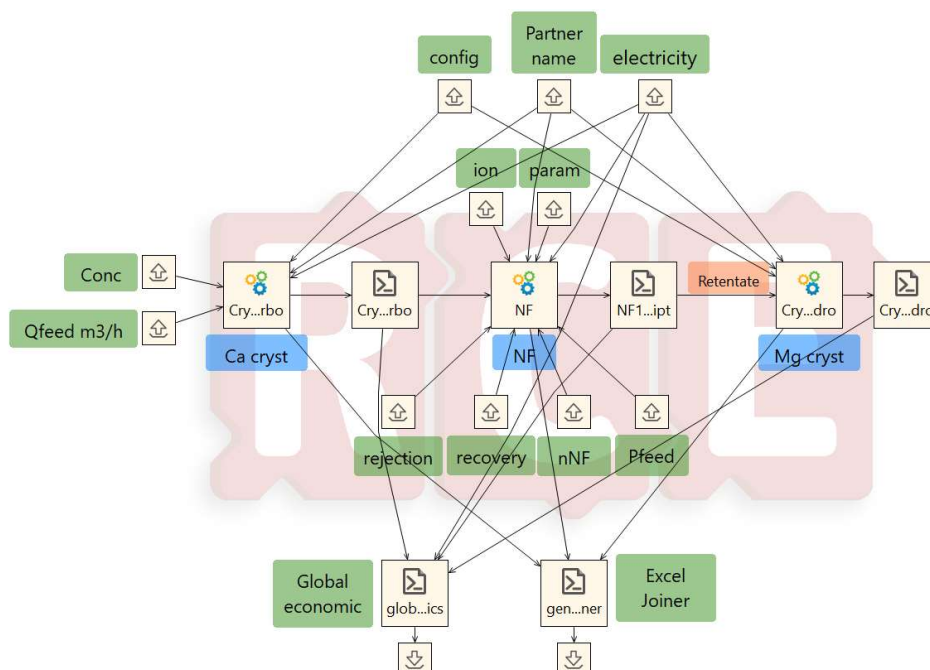


Figure 29: Graphical illustration of the implemented treatment chain on RCE for the Spanish replication study.

As can be seen from this example, the tools are versatile and can be used in a number of desired combinations to simulate any treatment chain. Additional technology tools like eutectic freeze crystallizer (EFC) and ion exchange resins (IEX) can be modelled (preferably in Python) and integrated with RCE to use them as *Integrated Tools* to simulate further treatment chains. For more information about the server access and to obtain template workflows, you can contact Nikhil.Pawar@dlr.de or Benjamin.Fuchs@dlr.de.

13. Bibliography

- Alamdari, A., M. R. Rahimpour, N. Esfandiari, and E. Nourafkan. 2008. Kinetics of magnesium hydroxide precipitation from sea bittern. *Chemical Engineering and Processing* 47:215–221.
- Alexandratos, S. D. 2009. Ion-Exchange Resins: A Retrospective from Industrial and Engineering Chemistry Research. *Ind. Eng. Chem. Res.* 48:388–398.
- Ali, N., A. W. Mohammad, and A. L. Ahmad. 2005. Use of nanofiltration predictive model for membrane selection and system cost assessment. *Separation and Purification Technology* 41:29–37.
- Alkaisi, A., R. Mossad, and A. Sharifian-Barforoush. 2017. A review of the water desalination systems integrated with renewable energy. *Energy Procedia* 110, 268–274.
- Alkhudhiri, A., N. Darwish, and N. Hilal. 2012. Membrane distillation: A comprehensive review. *Desalination* 287:2–18.
- AlMadani, H. M. N. 2003. Water desalination by solar powered electrodialysis process. *Renewable Energy*, 28:1915–1924.

- Andrjesdottir, O., C. L. Ong, M. Nabavi, S. Paredes, A. S. G. Khalil, B. Michel, and D. Poulikakos. 2013. An experimentally optimized model for heat and mass transfer in direct contact membrane distillation. *International Journal of Heat and Mass Transfer* 66:855–867.
- Bowen, W. R., B. Cassey, P. Jones, and D. L. Oatley. 2004. Modelling the performance of membrane nanofiltration—application to an industrially relevant separation. *Journal of Membrane Science* 242:211–220.
- Bowen, W. R., A. W. Mohammad, and N. Hilal. 1997. Characterisation of nanofiltration membranes for predictive purposes — use of salts, uncharged solutes and atomic force microscopy. *Journal of Membrane Science* 126:91–105.
- Campione, A., L. Gurreri, M. Ciofalo, G. Micale, A. Tamburini, and A. Cipollina. 2018. Electrodialysis for water desalination: A critical assessment of recent developments on process fundamentals, models and applications. *Desalination*, 434: 121–160.
- Carta, J., J. González, and V. Subiela. 2004. The SDAWES project: an ambitious R&D prototype for wind-powered desalination. *Desalination*, 161(1): 33–48.
- Chehayeb, K. M., D. M. Farhat, K. G. Nayar and J. H. Lienhard. 2017. Optimal design and operation of electrodialysis for brackish-water desalination and for high-salinity brine concentration. *Desalination* 420: 167-182.
- Chemicals, A. 2013. Selemion Ion Exchange Membranes, Model: DW Type 3E. A. Chemicals. Japan.
- Cipollina, A., M. Bevacqua, P. Dolcimascolo, A. Tamburini, A. Brucato, H. Glade, L. Buether, and G. Micale. 2014. Reactive crystallisation process for magnesium recovery from concentrated brines. *Desalination and Water Treatment*:1–12.
- Curto, D., V. Franzitta and A. Guercio (2021). "A Review of the Water Desalination Technologies." *Applied Sciences* 11(2).
- DLR 2021. Deutsches Zentrum für Luft- und Raumfahrt e. V. RCE. from <https://rcenvironment.de/>.
- DOWEX Ion Exchange Resins Water Conditioning Manual. (n.d.).
- DOWEX Marathon C Resin - Product Data Sheet. (n.d.).
- El-Dessouki, H. T., and H. M. Ettouney. 2002. *Fundamentals of Salt Water Desalination*. Elsevier.
- El-Dessouky, H., I. Alatiqi, S. Bingulac, and H. Ettouney. 1998. Steady-State Analysis of the Multiple Effect Evaporation Desalination Process. *Chem. Eng. Technol.* 21:437–451.
- Enciso, R., J.A. Delgadillo, O. Domínguez, and I. Rodríguez-Torres. 2017. Analysis and validation of the hydrodynamics of an electrodialysis cell using computational fluid dynamics. *Desalination*, 408: 127–132.
- ESDU. 1993. Condensation inside tubes: pressure drop in straight horizontal tubes. ESDU Series on Heat Transfer.
- Eykens, L., I. Hitsov, K. De Sitter, C. Dotremont, L. Pinoy, I. Nopens, and B. Van der Bruggen. 2016. Influence of membrane thickness and process conditions on direct contact membrane distillation at different salinities. *Journal of Membrane Science* 498:353–364.
- Fernandez-Gonzalez, C., A. Dominguez-Ramos, R. Ibañez, and Irabien, A. 2015. Sustainability assessment of electrodialysis powered by photovoltaic solar energy for freshwater production. *Renewable and Sustainable Energy Reviews* 47, 604–615.
- Filmtec Reverse Osmosis Membranes Technical Manual. (n.d.).
- Geraldes, V., and M. D. Afonso. 2006. Generalized Mass-Transfer Correction Factor for Nanofiltration and Reverse Osmosis. *AIChE Journal* 52:3353–3362.
- Geraldes, V., and A. M. B. Alves. 2008. Computer program for simulation of mass transport in nanofiltration membranes. *Journal of Membrane Science* 321:172–182.
- Gu, B., C.S. Adjiman, X.Y. Xu. 2017. The effect of feed spacer geometry on membrane performance and concentration polarisation based on 3D CFD simulations. *J. Membr. Sci.*, 527: 78–91.

- Gude, V.G., N. Nirmalakhandan, S. Deng. 2010. Renewable and sustainable approaches for desalination. *Renewable and Sustainable Energy Reviews* 14, 2641–2654.
- Gurreri, L., G. Battaglia, A. Tamburini, A. Cipollina, G. Micale, M. Ciofalo. 2017. Multiphysical modelling of reverse electrodialysis. *Desalination*, 423: 52–64.
- Hasan, M. and M. Louhi-Kultanen, Ice growth kinetics modeling of air-cooled layer crystallization from sodium sulfate solutions, *Chem. Eng. Sci.* 133 (2015) 44-53.
- Hasan, M., R. Filimonov, J. Chivavava, J. Sorvari, M. Louhi-Kultanen, and A. Emslie Lewis. Ice growth on the cooling surface in a jacketed and stirred eutectic freeze crystallizer of aqueous Na₂SO₄ solutions. *Separation and Purification Technology* 175 (2017) 512–526.
- Hassan, A. S., and M. A. Darwish. 2014. Performarce of thermal vapor compression. *Desalinationn* 335:41–46.
- Hitsov, I., L. Eykens, W. De Schepper, K. De Sitter, C. Dotremont, and I. Nopens. 2017. Full-scale direct contact membrane distillation (DCMD) model including membrane compaction effect. *Journal of Membrane Science* 524:245–256.
- Hitsov, I., T. Maere, K. De Sitter, C. Dotremont, and I. Nopens. 2015. Modelling approaches in membrane distillation: A critical review. *Separation and Purification Technology* 142:48–64.
- Hitsov, I., K. De Sitter, C. Dotremont, and I. Nopens. 2018. Economic modelling and model-based process optimization of membrane distillation. *Desalination* 436:125–143.
- Ishimaru, N. 1994. Solar photovoltaic desalination of brackish-water in remote areas by electrodialysis. *Desalination*, 98 (1–3): 485–493.
- Jamal, K., M. A. Khan, and M. Kamil. 2004. Mathematical modeling of reverse osmosis systems. *Desalination* 160:29–42.
- Khalifa, A., H. Ahmad, M. Antar, T. Laoui, and M. Khayet. 2017. Experimental and theoretical investigations on water desalination using direct contact membrane distillation. *Desalination* 404:22–34.
- Khayet, M., A. Velasquez, and J. I. Mengual. 2004. Modelling mass transport through a porous partition: Effect of pore size distribution. *Journal of Non-Equilibrium Thermodynamics* 29:279–299.
- Kimura, S., and S. Sourirajan. 1967. Analysis of data in reverse osmosis with porous cellulose acetate membrane used. *AIChE Journal* 13:497–503.
- Kucera J. 2014. *Desalination: Water from water*. Scrivener Publishing.
- Lee, H., F. Sarfert, H. Strathmann, S.H. Moon. 2002. Designing of an electrodialysis desalination plant. *Desalination*, 142: 267–286.
- Liu, Z., L. Li, Y. Chen, X. Li, Y. Zhang, and G. Shen. 2011. Optimal parameters of response surface methodology for precipitation of magnesium hydroxide flame retardant. *Chin. J. Process Eng.* 11:1017–1023.
- Lundstrom, J.E. 1979. Water desalting by solar powered electrodialysis. *Desalination*, 31 (1–3): 469–488.
- Lonsdale, H. K., U. Merten, and R. L. Riley. 1965. Transport properties of cellulose acetate osmotic membranes. *Journal of Applied Polymer Science* 9:1341–1362.
- M. Bialik, P. Sedin, and H. Theliander. 2008. Boiling Point Rise Calculations in Sodium Salt Solutions. *Ind. Eng. Chem. Res.* 47:1283–1287.
- Malek, A., M. N. . Hawlader, and J. C. Ho. 1996. Design and Economics of RO seawater desalination. *Desalination* 105:245–261.
- Malek, P., J.M. Ortiz, and H.M.A. Schulte-Herbrüggen. 2016. Decentralized desalination of brackish water using an electrodialysis system directly powered by wind energy. *Desalination*, 377, 54–64.
- Marchisio, D. L., J. T. Pikturna, m R. O. Fox, R. D. Vigil, and A. A. Barresi. 2003a. Quadrature Method of Moments for Population-Balance Equations. *AIChE Journal* 49:1266–1276.

- Marchisio, D. L., R. D. Vigil, and R. O. Fox. 2003b. Quadrature method of moments for aggregation-breakage processes. *Journal of Colloid and Interface Science* 258:322–334.
- McGovern, R. K., A. M. Weiner, L. Sun, C. G. Chambers, S. M. Zubair and J. H. Lienhard. 2014. On the cost of electrodialysis for the desalination of high salinity feeds. *Applied Energy* 136: 649-661.
- McGovern, R. K., S. M. Zubair and J. H. Lienhard 2014. The benefits of hybridising electrodialysis with reverse osmosis. *Journal of Membrane Science* 469: 326-335.
- Micari, M. 2020. Integration of Desalination and Purification processes for the Treatment and Valorization of Industrial Brines. Ph.D., University of Stuttgart.
- Moser, M. 2015. Combined Electricity and Water Production Based on Solar Energy. Institut für Energiespeicherung der Universität Stuttgart.
- Nayar, K. G., J. Fernandes, R. K. McGovern, K. P. Dominguez, A. McCance, B. S. Al-Anzi and J. H. Lienhard. 2019. Cost and energy requirements of hybrid RO and ED brine concentration systems for salt production. *Desalination* 456: 97-120.
- Oatley, D. L., L. Llenas, R. Pérez, P. M. Williams, X. Martínez-Lladó, and M. Rovira. 2012. Review of the dielectric properties of nanofiltration membranes and verification of the single oriented layer approximation. *Advances in Colloid and Interface Science* 173:1–11.
- Al-Obaidani, S., E. Curcio, F. Macedonio, G. Di Profio, H. Al-Hinai, and E. Drioli. 2008. Potential of membrane distillation in seawater desalination: Thermal efficiency, sensitivity study and cost estimation. *Journal of Membrane Science* 323:85–98.
- Omar, H. M., and S. Rohani. 2017. Crystal Population Balance Formulation and Solution Methods: A review. *Crystal Growth and Design* 17:4028–4041.
- Ortega-Delgado, B., L. García-Rodríguez, and D. C. Alarcon-Padilla. 2017. Opportunities of improvement of the MED seawater desalination process by pretreatments allowing high-temperature operation. *Desalination and Water Treatment*, 97:94–108.
- Ortiz, J. M., E. Expósito, F. Gallud, V. García García, V. Montiel, A. Aldaz. 2006. Photovoltaic electrodialysis system for brackish water desalination: Modeling of global process, *J. Membr. Sci.*, 274: 138–149.
- Pawar, N. D., K. Mitko, S. Harris and G. Korevaar. 2021. (submitted) Valorization of Coal Mine Effluents – Challenges and Economic Opportunities. *Water Resources and Industry*.
- Pitzer, K. S., and G. Mayorga. 1973. Thermodynamics of Electrolytes. I. Activity and Osmotic Coefficients for Strong Electrolytes with One or Both Ions Univalent. *The Journal of Physical Chemistry* 77:2300–2308.
- Al-Qaraghuli, A. and L.L. Kazmerski. 2012. Comparison of technical and economic performance of the main desalination processes with and without renewable energy coupling. *Proceedings of the American Solar Energy Society World Renewable Energy Forum*, 1–8.
- Qasem, N.A.A., B. Ahmed Qureshi, and S.M. Zubair. 2018. Improvement in design of electrodialysis plants by considering the Donnan potential. *Desalination*, 441: 62–76.
- Qtaishat, M., T. Matsuura, B. Kruczek, and M. Khayet. 2008. Heat and mass transfer analysis in direct contact membrane distillation. *Desalination* 219:272–292.
- Qureshi, B.A. and Zubair, S.M. 2018. Design of electrodialysis desalination plants by considering dimensionless groups and variable equivalent conductivity. *Desalination*, 430: 197–207.
- Roy, Y., M. H. Sharqawy, and J. H. Lienhard. 2015. Modeling of flat-sheet and spiral-wound nanofiltration configurations and its application in seawater nanofiltration. *Journal of Membrane Science* 493:360–372.
- Sadrzadeh, M., A. Kaviani, and T. Mohammadi. 2007. Mathematical modeling of desalination by electrodialysis. *Desalination*, 206: 538–546.
- Senthilmurugan, S., A. Ahluwalia, and S. K. Gupta. 2005. Modeling of a spiral-wound module and estimation of model parameters using numerical techniques. *Desalination* 173:269–286.

- Sharqawy, M. H., J. H. Lienhard V, and S. M. Zubair. 2010. The thermophysical properties of seawater: A review of existing correlations and data. *Desalination and Water Treatment* 16:354–380.
- Shen, S. 2015. Thermodynamic Losses in Multi-effect Distillation Process. *Materials Science and Engineering* 88:1–12.
- Sommariva, C. 2010. *Desalination and Advanced Water Treatment-Economics and Financing*. . Balaban Desalination Publications.
- Tado, K., F. Sakai, Y. Sano, and A. Nakayama. 2016. An analysis on ion transport process in electrodialysis desalination, *Desalination* 378: 60–66.
- Tedesco, M., A. Cipollina, A. Tamburini, W. van Baak, and G. Micale. 2012. Modelling the reverse electrodialysis process with seawater and concentrated brines. *Desalination Water Treat.* 49: 404–424.
- Tedesco, M., A. Cipollina, A. Tamburini, I.D.L. Bogle, and G. Micale. 2015. A simulation tool for analysis and design of reverse electrodialysis using concentrated brines. *Chemical Engineering Research and Design* 93: 441-456.
- Tsiakis, P. and L.G. Papageorgiou. 2005. Optimal design of an electrodialysis brackish water desalination plant. *Desalination*, 173: 173–186.
- Turek, M., and W. Gnot. 1995. Precipitation of magnesium hydroxide from brine. *Ind. Eng. Chem. Res* 34:244–250.
- Veerman, J., M. Saakes, S.J. Metz, and G.J. Harmsen. 2011. Reverse electrodialysis: a validated process model for design and optimization. *Chem. Eng. J.* 166: 256–268.
- Veza, J., B. Peñate, and F. Castellano. 2004. Electrodialysis desalination designed for off-grid wind energy. *Desalination*, 160 (3): 211–221.
- Vezzani, D., and S. Bandini. 2002. Donnan equilibrium and dielectric exclusion for characterization of nanofiltration membranes. *Desalination* 149:477–483.
- Vince, F., F. Marechal, E. Aoustin, and P. Breant. 2008. Multi-objective optimization of RO desalination plants. *Desalination* 222:96–118.
- Wheaton, R., and L. Lefevre. 2016. *DOWEX Ion Exchange Resins - Fundamental of Ion Exchange*. . Dow Chemical Company.
- Wilf, M. 2007. *The Guidebook to Membrane Desalination Technology*. Balaban Desalination Publications.